MISSING
PAGE

To my parents

ACKNOWLEDGEMENTS

I would like to thank my advisor for her guidance and encouragement through this difficult journey. It was comforting to find that her door was always open to discuss my problems and concerns. I would also like to express my gratitude to the members of my committee for their time and consideration.

I have many friends and colleagues without whom this dissertation could not have been successfully completed. I would like to thank Mr. Marcel Tutt, Prof. Larry Dunleavy, Mr. Walid Ali-Ahmad, and Prof. Gabriel Rebeiz for their help in the development of experimental procedures. The many enlightening discussions with Mr. Norm VandenBerg, Mr. Andy Engel, Mr. Nihad Dib, and Ms. Emilie Van Deventer helped to solidify abstract ideas, and for this I thank them.

The encouragement I recieved from my family eased the many anxieties encountered in the Ph.D. process, and made it considerably more enjoyable than it could have been. Finally, I thank Ms. Mary Magyar for helping me to prepare this manuscript and for never failing to believe in me.

TABLE OF CONTENTS

LIST OF TABLES

LIST OF FIGURES

Figure

LIST OF APPENDICES

Appendix

CHAPTER I

INTRODUCTION

1.1 Motivation and Objectives

Planar transmission line structures are essential components in microwave monolithic integrated circuits (MMICS) and monolithic antenna arrays. Current trends from hybrid technology to higher density planar integration are strongly dependent on the availability of well characterized passive planar structures for interconnect and distributed circuit functions. Microstrip is the most commonly used transmission line structure because of its compatibility with discrete MMIC components, and the ease with which it can be incorporated into a larger design. Nonetheless, it suffers from a variety of problems at millimeter-wave frequencies including high radiation and conductor losses, and dispersion. In addition, parasitic electromagnetic coupling between circuits in close proximity will complicate higher density MMIC designs. All of these problems are compounded further by the inability to tune microstrip circuits after fabrication. Consequently, millimeter and submillimeter-wave MMIC design cycles are destined to remain lengthy unless accurate and reliable theoretical models are successfully integrated into the process. The approach and models presented can eliminate this waste of resources and reduce development cost and time.

Existing microstrip computer aided design (CAD) software is based upon quasi-

static and semi-empirical data, and has demonstrated good performance at frequencies up to X-band. At higher frequencies, non-ideal electromagnetic effects are not modeled correctly (or at all), and the results can be inaccurate or even misleading. The fullwave technique applied here makes no simplifying assumptions which limit its accuracy at higher frequencies. All electromagnetic effects are inherently included in the analysis. Consequently, this technique can accurately determine the useful frequency range of microstrip, provide improved CAD models, and be used to evaluate existing models.

1.2 Types of Planar Transmission Lines

Planar transmission line structures are well suited for use in hybrid circuits or (M)MICS because of their conformal, two-dimensional nature and their compatability with active devices and lumped elements. In addition, they are ideal for monolithic array structures where they can be used both as feeding structures and antenna elements. Furthermore, they are easily fabricated with photolithographic and etching techniques. Numerous configurations have been proposed for these structures. They include, but are not limited to i) stripline, ii) microstrip, iii) slotline, iv) coplanar strips, and v) coplanar waveguide, all of which are shown in Figure 1.1. Stripline is included in this class although it is not easily accessible for interconnection to discrete components. These structures, with the exception of stripline, propagate hybrid modes having both longitudinal electric and magnetic fields. Nonetheless, they are called "quasi-TEM" structures because they propagate fundamental modes which are close to TEM , especially at low frequencies. These lines can be of either closed or open type as shown in Figure 1.2 for microstrip. (M)MICS are often packaged in some type of cavity or waveguide enclosure with a notable exception being

when they are part of an antenna array.

As previously mentioned, microstrip is the most widely used planar line. However, more recently coplanar waveguide has found wide usage, because it has easier access to the ground plane which is located on the top face, and its guide wavelength and characteristic impedance are less dependent than microstrip on the height of the substrate.

1.3 Techniques for analysis of planar transmission lines

The methods of analysis of microstrip structures are traditionally divided into three groups entitled i) quasi-static,[1]-[6] ii) dispersive[7]-[10], and iii) fullwave [11]-[28]. Quasi-static techniques assume that the microstrip supports a TEM mode of propagation and circuit parameters are determined by calculations of the static capacitance and inductance. Dispersion models are derived semi-empirically, and provide information concerning the frequency behavior of microstrip. Fullwave techniques provide rigorous solutions for the time-varying electromagnetic fields, and account accurately for high frequency dispersion, electromagnetic coupling, and radiation. The three categories differ greatly in complexity and accuracy. Quasi-static and dispersion models breakdown with increasing frequency, and are generally considered low frequency techniques. Fullwave models are complicated and computer intensive, and are the most appropriate for high frequencies. A brief review of some of these techniques is given below.

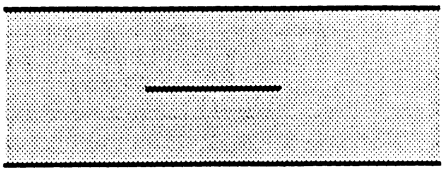

a. Stripline

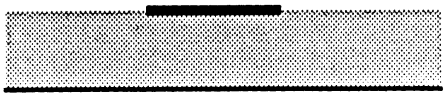

b. Microstrip

C. Slotline

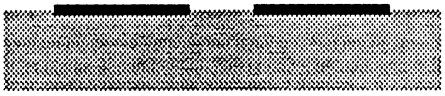

D. Coplanar Strips

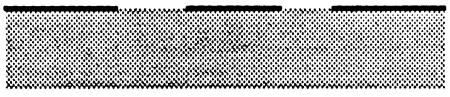

E. Coplanar Waveguide

Figure 1.1: Types of Planar transmission Lines

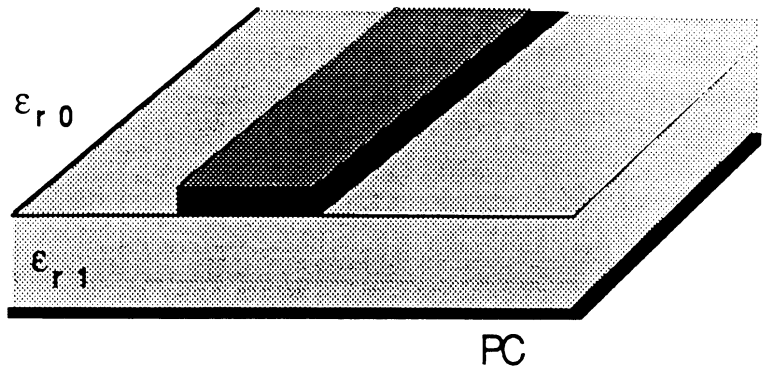

a. Open Microstrip

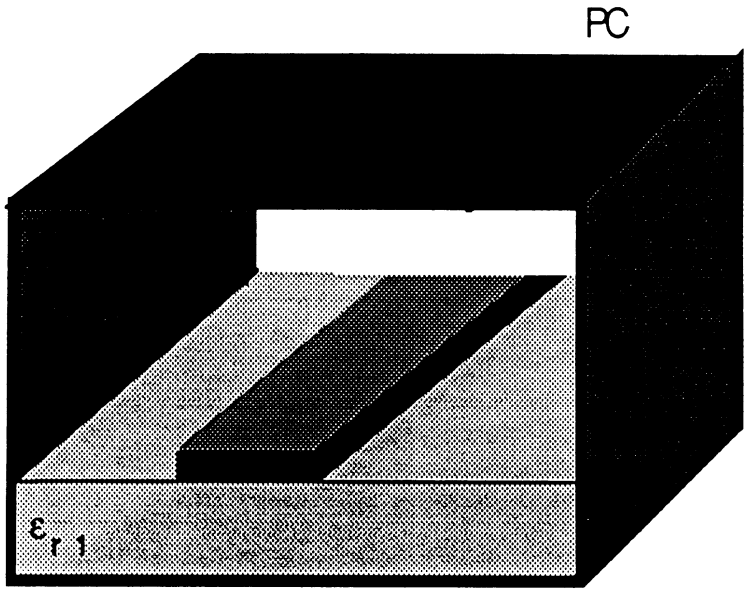

b. Enclosed Microstrip

Figure 1.2: Open and Enclosed Microstrip Lines

1.3.1 Quasi-Static Models

Circuit models obtained with quasi-static techniques are extensively used in commercial CAD packages because they are well understood and numerically efficient. Included in this class are modified conformal mapping[29], finite difference [30], and integral equation techniques [31]. With modified conformal mapping, the open microstrip geometry is transformed to a parallel plate structure by a complex mapping. Closed form expressions can then be obtained for the static capacitance of the new geometry. The quasi-static integral equation approach involves an application of the method of moments to Laplace's equation in its integral form, while the finite difference technique solves Laplace's equation in its differential form. Integral equation approaches are applicable to open or closed problems, while finite difference techniques are difficult to implement without an enclosing boundary. The TEM assumption limits these techniques to frequencies where the substrate and conductor widths are a small fraction of a wavelength.

1.3.2 Dispersion Models

With increasing frequency, the microstrip structure deviates from having a TEM behavior. Techniques which attempt to semi-empirically account for the hybrid nature of the fields are called dispersion models. Two such techniques are the planar waveguide [32] and ridged waveguide [33] models. Both of these techniques are based on the study of structures which resemble microstrip, but can be handled in closed form. The planar waveguide is a parallel plate capacitor, having a frequency dependent width and dielectric constant to account for dispersion. The ridged waveguide is an inhomogeneous parallel plate waveguide having three regions. A dielectric section is sandwiched between two larger free space sections. The entire structure is bounded

with vertical magnetic walls. Both the planar and ridged waveguides have a zero frequency behavior which is determined experimentally or by quasi-static techniques, and is identical to the corresponding microstrip geometry.

1.3.3 High Frequency Fullwave Models

Techniques which account for the hybrid nature of the microstrip mode by solving for time-varying electromagnetic fields are fullwave methods. Fullwave models provide the most accurate characterization of microstrip, especially at high frequencies. They include the finite difference method[34], and the space domain[19] and spectral domain integral equation techniques [36]. The finite difference technique requires the solution of the wave equation subject to the appropriate boundary conditions in differential form. The technique is more easily implemented with an enclosing boundary, however, it is possible to treat the open problem with the use of an absorbing boundary [35]. Integral equation techniques involve solutions to the electric or magnetic field integral equations by the method of moments. The application of the technique differs for open and enclosed microstrip by the form of the Green's function, which may be represented as a Fourier integral in the open problem and a Fourier series in the enclosed problem. Spectral and space domain techniques differ by the application of the method of moments. In the spectral domain technique, the representation of the unknown microstrip current is Fourier transformed, and the method of moments is applied in the spectral domain. In the space domain technique, the method of moments is applied in the space domain.

1.4 Experimental Techniques for Measurement of Circuit Parameters

Experimental verification is critical for any fullwave numerical study, because the theoretical approaches are extremely complex. Therefore, measurments were performed to validate the numerical models at every stage. This section provides a brief overview to microwave planar circuit measurments. The 8510B automatic network analyzer can provide error correction for 7 mm coaxial measurements with the aid of a 7 mm calibration kit containing a coaxial short, open, and precision 50 ohm load. Unfortunately, in the measurement of microstrip and other planar transmission line structures, difficulties arise due to the need for a fixture with coaxial-to-microstrip transitions, and the unavailability of precision microstrip standards (open, short, load). For example, microstrip open-ends radiate, shorts require a via hole transition, and precision thin film 50 ohm loads are not available. Consequently, techniques have been developed to extract network parameter information without the reliance on known standards. These methods may be divided into resonator [37], time domain [38], fixture equivalent circuit modeling [39], and fixture de-embedding techniques[40]-[42]. A comparison of these methods is presented in [43]. Based on that study and the availability of microwave equipment and computer software, the Thru-Reflect-Line (TRL) de-embedding technique was judged the best approach here.

Fixture De-embedding

The TRL de-embedding scheme is a variation on the Thru-Short-Delay (TSD) approach. Another variation is the Line-Reflect-Line (LRL) approach. All three are based on the use of simple planar transmission line sections and loads. In particular,

TSD relies on two different length sections of transmission line, and a shorted line. LRL and TRL are variations which recognize that the short may be replaced with any load having a high reflection coefficient. For microstrip measurements, an open is preferred because it is more easily realized than a short. LRL differs from TRL by the position where the reference plane is established. In TRL the thru line is considered to be zero length (which implies that the reference will be located at the center of the line), while in LRL the thru line may be of non-zero length. In either case, the microstrip line's phase constant need not be accurately known, and is determined through the de-embedding procedure. This is also the case for the parasitics of the open-end standard. All three approaches require that the microstrip-to-coaxial transitions be repeatable.

1.5 Overview

A comprehensive collection of theoretical data concerning the high frequency behavior of open microstrip discontinuities is presented. In the past, fullwave analysis has been proven a valuable tool for microstrip analysis, but there has been a failure in effectively using these techniques to improve our understanding of high frequency behavior. One area where this is particularly true is with radiation losses. This study not only investigates the impact of radiation losses on microwave circuit performance, but also presents low-loss designs, and explains the improvements from an electromagnetic point of view.

In Chapter 2, the SDIE approach to microstrip structures is presented, including the implementation of the method of moments to the electric field integral equation. A method where scattering parameters are extracted from multiport microstrip networks is also described. Furthermore, it is shown how radiation losses are separated

into space and surface wave contributions, and how radiation patterns within the substrate, representing surface wave fields, are obtained.

The numerical techniques applied to the solution of this problem are reviewed in Chapter 3. Analytical methods have been used to reduce this difficult numerical problem to manageable computer requirements. In fact, results of this study have all been obtained on a desktop Apollo workstation. The numerical convergence and accuracy is also investigated in Chapter 3, with specific recommendations and conclusions given.

Numerical results obtained by the SDIE approach are presented in Chapters 4 and 5. In Chapter 4, microstrip structures are treated from a circuit perspective, with results presented in terms of scattering parameters. Examples of microstrip step, bend, cross-, and T-junction discontinuities are offered. Matching networks with one and two stub tuners are presented, and meander line sections useful for phase shifting and filtering are explored. Finally, discontinuities printed on multilayered substrates are analyzed.

Chapter 5 investigates the radiation properties of microstrip discontinuities. Patterns depicting surface wave propagation within the dielectric substrate are shown for a radial stub and a microstrip bend. In addition, the relative levels of space and surface wave radiation occurring are quantified. The effect of substrate composition (multi-layers) and the presence of superstrates on radiation properties is also presented.

The results throughout this dissertation have been fully supported by comparison with published data and other CAD techniques. For the cases where no verification was available, experimental studies were performed. In section 4.2, an implementation of the TRL fixture de-embedding approach used to measure open microstrip

network parameters is presented. In particular, experimental results were obtained for microstrip rectangular and radial stubs. The experimental results were found to be very repeatable as will be shown. In section 5.2, a new method for obtaining far-field power patterns at the substrate level is presented. This technique was used to verify the direction of surface wave propagation in the dielectric substrate.

CHAPTER II

THE SPACE DOMAIN INTEGRAL EQUATION TECHNIQUE

2.1 Introduction

This chapter presents the Space Domain Integral Equation Technique (SDIE), which has been used to study the high frequency behavior of open microstrip discontinuities. The approach is a full electromagnetic or fullwave analysis, and employs the dyadic Green's function for a grounded multi-layer dielectric configuration, shown in section 2.3. This results in a technique that is able to analyze microstrip structures printed on a single or multi-layer dielectric, with or without a superstrate. Furthermore, the method of moments is applied (section 2.4) with two components of electric current in the plane of the discontinuity, allowing for the treatment of an extensive class of microstrip elements such as steps in width, corners, T-junctions, and cross junctions. This microstrip current is represented by summations of sub-domain rooftop basis functions which are substituted into the electric field integral equation, and a system of linear equations is created by the application of Galerkin's method. The solution of this system is the current on the conducting strips. An approach, based on transmission line theory, is then employed to determine the network parameters for the multiport microstrip network as detailed in section 2.5. Total radiation

loss may be obtained directly from the scattering parameters, however in section 2.6, an analysis is presented which is used to separate total radiation loss into space wave and surface wave contributions.

2.2 Problem Geometry

In the past, much of the published work on the full wave analysis of open microstrip discontinuities has been limited to structures with strip widths much smaller than the microstrip wavelength ($w << \lambda_g$). Under this approximation, the transverse current component was considered a second order effect and neglected [19]. Therefore, the analysis was restricted to thin-strip discontinuities such as open ends, gaps, and coupled line filters. Obviously, the transverse current component is critical in more complicated structures such as steps in width, corners, and T-junctions, and is therefore included here.

The general multilayer open microstrip geometry is shown in Figure 2.1. The dielectric layers are considered lossless, but the development is not limited by this assumption. The conductors have infinite conductivity with the strip conductor being of finite thickness ($t << \lambda_g$). An extension of the problem to include conductor loss is detailed in section 2.4.2. No assumptions have been made which limit the validity of this study with respect to frequency or the complexity of the microstrip shape.

2.3 Integral Equation and Green's Function

Assuming the time dependence $e^{j\omega t}$, Maxwells equations are of the form

$$\bar{\nabla} \times \bar{H} = \bar{J} + j\omega\epsilon_i \bar{E} \tag{2.1}$$

$$\bar{\nabla} \times \bar{E} = -j\omega\mu_0 \bar{H} \tag{2.2}$$

$$\bar{\nabla} \cdot \bar{B} = 0 \tag{2.3}$$

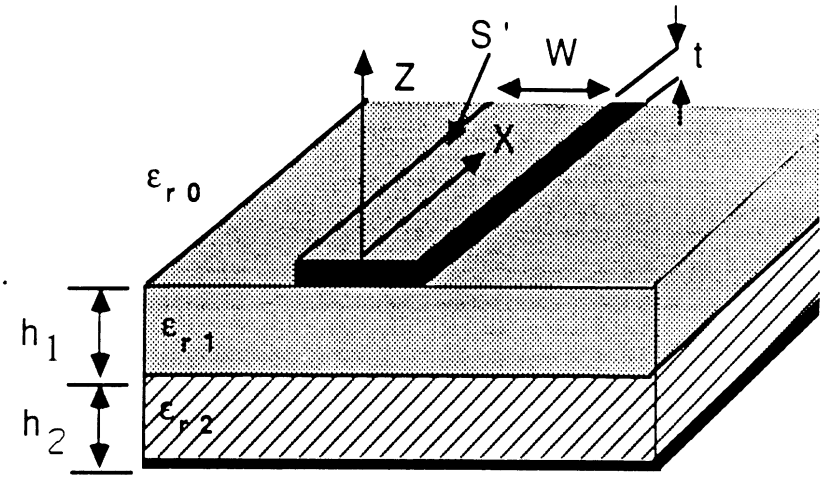

a. Microstrip discontinuity with multi-layer substrate

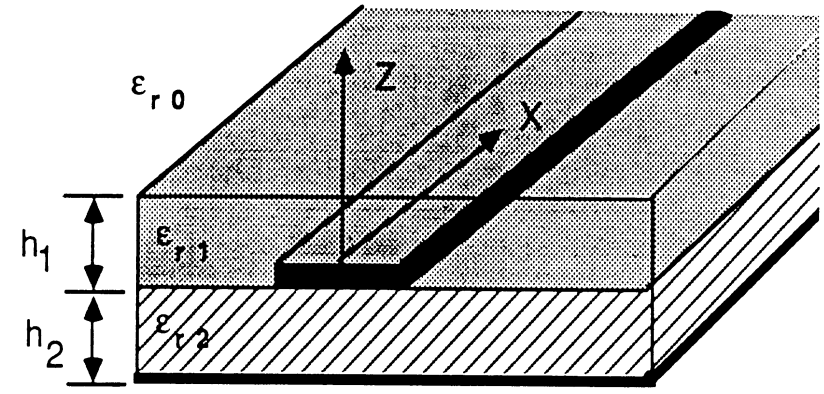

b. Microstrip discontinuity with superstrate

Figure 2.1: Multilayer open microstrip geometry with and without a superstrate

$$\bar{\nabla} \cdot \bar{D} = 0 \tag{2.4}$$

with ϵ_i the dielectric permittivity in the region (i). All the results presented have non-magnetic substrates ($\mu = \mu_0$). In view of (2.3), the magnetic flux density $\bar{B}$ may be written as the curl of the magnetic vector potential($\bar{A}$)

$$\bar{B} = \mu_0 \bar{H} = \bar{\nabla} \times \bar{A} \quad . \tag{2.5}$$

Substitution of equation (2.5) into equation (2.2) results in

$$\bar{\nabla} \times (\bar{E} + j\omega \bar{A}) = 0 \quad . \tag{2.6}$$

Introducing the scalar potential Φ, the solution to equation (2.6) for the electric field may be expressed

$$\bar{E} = -j\omega \bar{A} + \bar{\nabla}\Phi \quad . \tag{2.7}$$

Substitution of (2.5) and (2.7) into equation (2.1) yields

$$\nabla \times \nabla \times \bar{A} = -\nabla^2 \bar{A} + \nabla(\nabla \cdot \bar{A}) = \mu_0 \bar{J} + k_i^2 \bar{A} + j\omega \epsilon_i \mu_0 \nabla \Phi \tag{2.8}$$

In equation 2.5, only the curl of the vector potential was specified, and the divergence may now be conveniently defined by the Lorentz condition as

$$\Phi = \frac{1}{j\omega \epsilon_i \mu_0} \nabla \cdot \bar{A} \quad . \tag{2.9}$$

Consequently, substitution of (2.9) into (2.8) results in the inhomogeneous wave equation

$$\nabla^2 \bar{A} + k_i^2 \bar{A} = -\mu_0 \bar{J} \quad . \tag{2.10}$$

In order to solve for the fields radiated by the current on the microstrip discontinuity, it is required that we first have the solution for an infinitesimal delta source. This solution is called the Green's function ($\bar{G}$), and is governed by the wave equation

$$\nabla^2 \bar{G} + k^2 \bar{G} = -\mu_0 \delta(r - r') \tag{2.11}$$

with the infinitesimal source located at r'. When the source is of arbitrary orientation the Green's function becomes dyadic

$$(\nabla^2 + k^2)\bar{\bar{G}} = -\mu_0 \bar{\bar{I}} \delta(r - r') \quad . \tag{2.12}$$

The unit dyad present in equation (2.12) has the form

$$\bar{\bar{I}} = \hat{x}\hat{x} + \hat{y}\hat{y} + \hat{z}\hat{z} \quad . \tag{2.13}$$

Utilizing Green's second identity with equations (2.10) and (2.12) [45] results in

$$\bar{A}(\bar{r}) \;=\; \mu_0 \oint_V \bar{\bar{G}} \cdot \bar{J} dv' \quad . \tag{2.14}$$

In view of equations (2.7), (2.9), and (2.14), the electric field may be expressed in terms of the dyadic Green's function as

$$\bar{E}(\bar{r}) = \oint_V \left(k_i^2 \bar{\bar{I}} + \bar{\nabla}\bar{\nabla} \right) \cdot \bar{\bar{G}} \cdot \bar{J} dv' \tag{2.15}$$

Referring to Figure 2.1, where the current is confined to the microstrip conducting strips, the integral equation may be written in the form of a surface integral

$$\bar{E}(x,y,z) = \int\int_{S'} [k_i^2 \bar{\bar{I}} + \bar{\nabla}\bar{\nabla}] \cdot \bar{\bar{G}}_i(x,y,z/x',y',z') \cdot \bar{J}(x',y')|_{z'=0} \; ds' \quad (i = 0,1,2) \tag{2.16}$$

where S' is the surface of the microstrip conducting strips, k_i is the wavenumber, and $\bar{\bar{G}}_i(x,y,z/x',y',z')$ is the dyadic Green's function in region (i). The current ($\bar{J}(x',y')$) present in equation (2.16) is two-dimensional in the plane of the discontinuity and can be represented as

$$\bar{J}(x',y') = J_x(x',y')\hat{x} + J_y(x',y')\hat{y} \quad . \tag{2.17}$$

The Green's function appropriate for the open microstrip problem with an arbitrary number of layers in the substrate and/or a superstrate [27],[46],[47] is expressed

in the form of Sommerfeld integrals given by:

$$G_{\xi\xi}(x,y,z/x',y',0) = \frac{\omega\mu_0}{2\pi k_0^2}\int_0^\infty J_0(\lambda\rho)\mathcal{Z}_{\xi\xi}(z)\frac{\mathcal{N}_{\xi\xi}(\lambda)}{f_1(\lambda)}d\lambda \tag{2.18}$$

$$G_{z\xi}(x,y,z/x',y',0) = \frac{\omega\mu_0}{2\pi k_0^2}\Phi(\phi)\int_0^\infty J_1(\lambda\rho)\mathcal{Z}_{z\xi}(z)\frac{\mathcal{N}_{z\xi}(\lambda)}{f_1(\lambda)f_2(\lambda)}d\lambda \tag{2.19}$$

$$\xi = x, y$$

where

$$\rho = \sqrt{(x-x')^2+(y-y')^2} \tag{2.20}$$

$$\Phi(\phi) = \begin{cases} \cos(\phi) & \xi = x \\ \sin(\phi) & \xi = y \end{cases} \tag{2.21}$$

and with $\mathcal{N}_{\xi\xi}(\lambda)$, $\mathcal{N}_{z\xi}(\lambda)$, $f_1(\lambda)$, and $f_2(\lambda)$ given in appendix A. In equations (2.18) and (2.19), $f_1(\lambda)$, and $f_2(\lambda)$ are analytic functions with discrete zeroes. The contributions from these zeroes give the power propagating in the substrate in the form of transverse electric (TE) and transverse magnetic (TM) surface waves, respectively.

2.4 The Method of Moments

In the previous section, the electric field integral equation for the open microstrip geometry was derived. This equation cannot be solved analytically for the complicated microstrip geometry. Consequently, the method of moments, a well known numerical technique for solving electromagnetic antenna, scattering, and monolithic circuit problems [48], is used.

A rectangular region containing the microstrip discontinuity is subdivided into smaller rectangles (see Figure 2.2) and the current is expressed as a superposition of known basis functions multiplied by unknown coefficients.

$$J_x(x',y') = \sum_{n_x=1}^{N_x+1}\sum_{m_x=1}^{M_x+1} I_{nm}^x[f_{n_x}(x')g_{m_x}(y')] \tag{2.22}$$

$$J_y(x',y') = \sum_{n_y=1}^{N_y+1}\sum_{m_y=1}^{M_y+1} I^y_{nm}[f_{n_y}(y')g_{m_y}(x')] \tag{2.23}$$

where the pairs (n_x, m_x) and (n_y, m_y) indicate the nodes in the mesh for the X-current and Y-current, respectively. In addition, the function $f_{n_\xi}(\xi')$ gives the longitudinal dependence of each component

$$f_{n_\xi}(\xi') = \begin{cases} \frac{\sin k_s(\xi_{n_\xi+1}-\xi')}{\sin k_s l_\xi} & \xi_{n_\xi} \le \xi' \le \xi_{n_\xi+1} \\ \frac{\sin k_s(\xi'-\xi_{n_\xi-1})}{\sin k_s l_\xi} & \xi_{n_\xi-1} \le \xi' \le \xi_{n_\xi} \\ 0 & Elsewhere \\ & (\xi,\zeta) = (x,y),(y,x) \end{cases} \tag{2.24}$$

while $g_{m_\xi}(\zeta')$ gives the transverse dependence

$$g_{m_\xi}(\zeta') = \begin{cases} 1 & \zeta_{m_\xi} \le \zeta' \le \zeta_{m_\xi+1} \\ 0 & Elsewhere \\ & (\xi,\zeta) = (x,y),(y,x) \end{cases} . \tag{2.25}$$

In the above, $l_\xi = \xi_{n_\xi+1} - \xi_{n_\xi}$, and k_s is a scaling parameter chosen to vary between k_0 (free space wavenumber) and k_i (wavenumber in the highest permittivity dielectric region). These are "sub"-domain basis functions because they are non-zero over only a small fraction of the structure.

With the substitution of equations (2.22) and (2.23) into equation (2.16), the original integral equation can be written in the form

$$\begin{aligned} E_x + \Delta E_x &= \sum_{n_x=1}^{N_x+1}\sum_{m_x=1}^{M_x+1} I^x_{nm} \int\int_{S'} \mathcal{K}_{xx}(x,y/x',y') f_{n_x}(x') g_{m_x}(y')\, dx'dy' \qquad (2.26) \\ &+ \sum_{n_y=1}^{N_y+1}\sum_{m_y=1}^{M_y+1} I^y_{nm} \int\int_{S'} \mathcal{K}_{xy}(x,y/x',y') f_{n_y}(y') g_{m_y}(x')\, dx'dy' \\ E_y + \Delta E_y &= \sum_{n_x=1}^{N_x+1}\sum_{m_x=1}^{M_x+1} I^x_{nm} \int\int_{S'} \mathcal{K}_{yx}(x,y/x',y') f_{n_x}(x') g_{m_x}(y')\, dx'dy' \qquad (2.27) \\ &+ \sum_{n_y=1}^{N_y+1}\sum_{m_y=1}^{M_y+1} I^y_{nm} \int\int_{S'} \mathcal{K}_{yy}(x,y/x',y') f_{n_y}(y') g_{m_y}(x')\, dx'dy' \end{aligned}$$

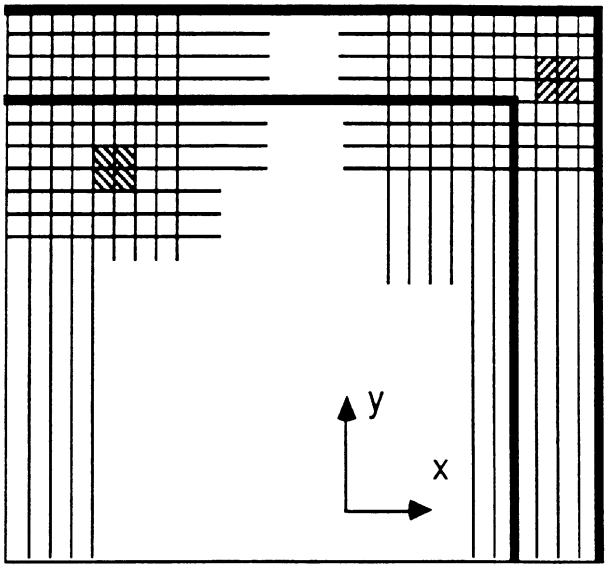

a. Typical Discretization

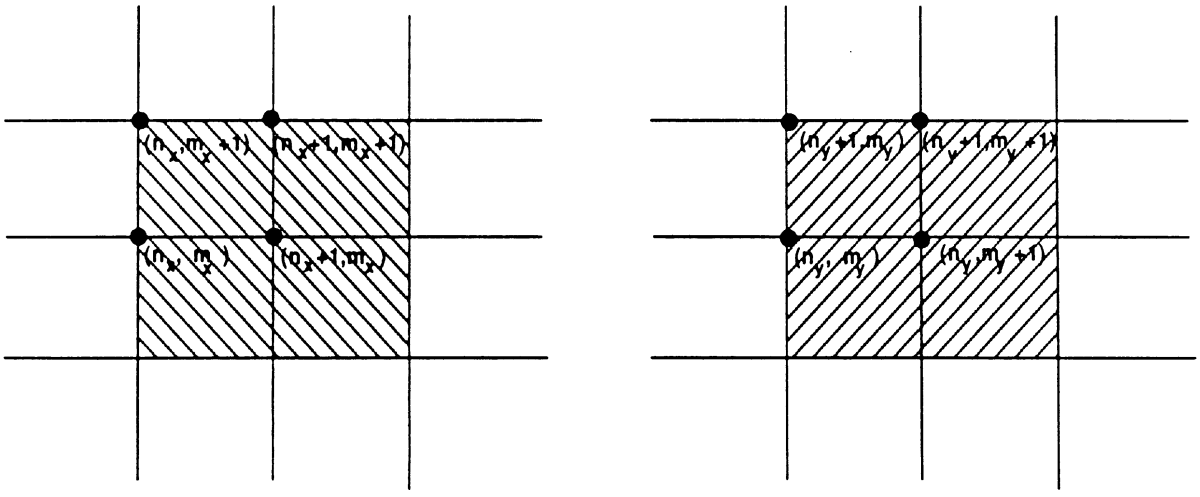

b. X-directed Mesh Y-directed Mesh

Figure 2.2: Sub-division of (M)MIC area around Corner Discontinuity

where $\mathcal{K}_{\xi\zeta}(x,y/x',y')(\xi,\zeta = x,y)$ are integro-differential operators given by

$$\mathcal{K}_{\xi\zeta}(x,y/x',y') = \int_0^\infty \left[(k_i^2\delta_{\xi\zeta} + \frac{\partial^2}{\partial\xi\partial\zeta})F_{\zeta\zeta} + \frac{\partial^2}{\partial z\partial\xi}F_{z\zeta}\right] d\lambda \qquad (2.28)$$

and $F_{\zeta\zeta}$ and $F_{z\zeta}$ are functions of λ of the following form

$$F_{\zeta\zeta} = \frac{\omega\mu_0}{2\pi k_0^2} J_0(\lambda\rho)\mathcal{Z}_{\zeta\zeta}(z)\frac{\mathcal{N}_{\zeta\zeta}(\lambda)}{f_1(\lambda)} \qquad (2.29)$$

$$F_{z\zeta} = \frac{\omega\mu_0}{2\pi k_0^2} \Phi(\phi)J_1(\lambda\rho)\mathcal{Z}_{z\zeta}(z)\frac{\mathcal{N}_{z\zeta}(\lambda)}{f_1(\lambda)f_2(\lambda)} \quad . \qquad (2.30)$$

In equations (2.26) and (2.27), the errors ΔE_x and ΔE_y are introduced under the approximations made for the unknown current distributions in equations (2.22)-(2.23). The z derivative in equation (2.28) may be replaced by an ζ derivative resulting in the modified form for the operator $\mathcal{K}_{\xi\zeta}$:

$$\mathcal{K}_{\xi\zeta}(x,y/x',y') = \int_0^\infty \left[\left(k_i^2\delta_{\xi\zeta} + \frac{\partial^2}{\partial\xi\partial\zeta}\right) f_{\zeta\zeta} + \frac{\partial^2}{\partial\xi\partial\zeta}f_{z\zeta}\right] J_0(\lambda\rho)d\lambda \qquad (2.31)$$

$$f_{\zeta\zeta} = F_{\zeta\zeta} \qquad (2.32)$$

$$f_{z\zeta} = -\frac{\omega\mu_0}{2\pi k_0^2} \mathcal{Z}'_{z\zeta}(z)\frac{\mathcal{N}_{z\zeta}(\lambda)}{\lambda f_1(\lambda)f_2(\lambda)} \qquad (2.33)$$

where $\delta_{\xi\zeta}$ is the kronecker delta and $\mathcal{Z}'_{z\zeta}(z)$ is the first derivative of $\mathcal{Z}_{z\zeta}(z)$ with respect to z. In this manner, the first order Bessel function in equation (2.28) is eliminated and the ρ dependence of all Sommerfeld integrals is in the argument of a zero'th order Bessel function of the first kind.

2.4.1 The Impedance Matrix

The application of Galerkin's method for error minimization reduces equations (2.26) and (2.27) to a matrix equation

$$\left[\ Z\ \right]\left[\ I\ \right] = \left[\ V\ \right] \quad . \qquad (2.34)$$

where $[Z]$ is a square matrix called the impedance matrix and contains the four sub-matrices shown below

$$\left[Z \right] = \begin{bmatrix} \left[Z_{xx} \right] & \left[Z_{xy} \right] \\ \left[Z_{yx} \right] & \left[Z_{yy} \right] \end{bmatrix} \tag{2.35}$$

In equation (2.34) the vector $[I]$ is the vector of unknown x and y current amplitudes, and $[V]$ is the excitation vector.

The elements of each submatrix of the impedance matrix are given by the following double inner products

$$Z_{xx}(n,m,\nu,\mu) = \langle f_{n_x}(x')g_{m_x}(y'),\ \mathcal{K}_{xx},\ f_{\nu_x}(x)g_{\mu_x}(y) \rangle \tag{2.36}$$

$$Z_{xy}(n,m,\nu,\mu) = \langle f_{n_x}(x')g_{m_x}(y'),\ \mathcal{K}_{xy},\ f_{\nu_y}(y)g_{\mu_y}(x) \rangle \tag{2.37}$$

$$Z_{yx}(n,m,\nu,\mu) = \langle f_{n_y}(y')g_{m_y}(x'),\ \mathcal{K}_{yx},\ f_{\nu_x}(x)g_{\mu_x}(y) \rangle \tag{2.38}$$

$$Z_{yy}(n,m,\nu,\mu) = \langle f_{n_y}(y')g_{m_y}(x'),\ \mathcal{K}_{yy},\ f_{\nu_y}(y)g_{\mu_y}(x) \rangle \tag{2.39}$$

where the pair $(\nu_\xi, \mu_\xi)(\xi = x, y)$ indicates the testing points. The terms Z_{xx} and Z_{yy} are called the direct-coupled terms because the direction of the testing field and the current component are the same, while the terms Z_{xy} and Z_{yx} are the cross-coupled terms.

The double inner products in equations (2.36)-(2.39) are expressed in the following manner

$$\langle f_{n_\xi} g_{m_\xi},\ \mathcal{K}_{\xi\zeta},\ f_{\nu_\zeta} g_{\mu_\zeta} \rangle = \int\int_{S'} dx'dy' \int\int_{S} dxdy \left(f_{n_\xi} g_{m_\xi}\ \mathcal{K}_{\xi\zeta}\ f_{\nu_\zeta} g_{\mu_\zeta} \right) \tag{2.40}$$

where S, and S' represent the surface of the microstrip conducting strips for the testing and basis cells, respectively.

2.4.2 Excitation Vector

The elements of the excitation vector are of the form

$$\left[V \right] = \left[\begin{bmatrix} V_x^{\nu,\mu} \end{bmatrix} \right] \\ \begin{bmatrix} V_y^{\nu,\mu} \end{bmatrix} \tag{2.41}$$

with

$$V_x(\nu,\mu) = \int\int_S dxdy \ (E_x(x,y)\, f_{\nu_x} g_{\mu_x}) \tag{2.42}$$

$$V_y(\nu,\mu) = \int\int_S dxdy \ \left(E_y(x,y)\, f_{\nu_y} g_{\mu_y}\right) \tag{2.43}$$

Lossy Conductors

Resistive losses in the microstrip conducting strips may also be included by the replacement of the conductive strips with infinitesimally thin surface impedance boundaries. The boundary conditions on the strip conductors are imposed through the following relation

$$\bar{z} \times \left[\bar{z} \times \bar{E}(x,y,z)\right] = \bar{\bar{Z}} \cdot (\bar{H} \times \hat{z}) \qquad x,y \in S \tag{2.44}$$

where $\bar{E}_t$ is the tangential electric field over the surface (S) of the conducting strips and

$$\bar{\bar{Z}}(f) = z_x \hat{x}\hat{x} + z_y \hat{y}\hat{y} \tag{2.45}$$

is a dyad whose components represent the appropriate surface impedance boundaries along the x and y directions. These frequency dependent impedance boundaries are evaluated by a quasi-TEM analysis in such a way that they provide the overall effect of the penetration of the fields and the resulting current distributions within the strips [51]. This technique has provided very accurate results for conductor loss at millimeter-wave frequencies [52].

The magnetic fields are related to current on the strip conductor by the expression

$$\hat{z} \times \bar{H} = \bar{J}(x', y') \quad . \tag{2.46}$$

In view of equation (2.46), equations (2.42) and (2.43) take the form

$$V_x(\nu, \mu) = -\int\int_S dxdy \; (Z_x \cdot J_x(x', y') \, f_{\nu_x} g_{\mu_x}) \tag{2.47}$$

$$V_y(\nu, \mu) = \int\int_S dxdy \; \left(Z_y \cdot J_y(x', y') \, f_{\nu_y} g_{\mu_y}\right). \tag{2.48}$$

In the above equations, the current is the only unknown, and may be represented by the summations of equations (2.22) and (2.23). The resulting expressions may be moved to the left side of the matrix equation and combined with the impedance matrix. The excitation vector may then determined in the same manner as the for the case of perfect conductors.

Perfect Conductors

The electric field on the microstrip conductors is the sum of the field excited by the electric current on the microstrip and the incident field on the strips. When the strips have infinite conductivity, the total tangential electric field must be zero.

In order to excite the discontinuity, voltage gap generators are utilized. The presence of the infinitesimally small gap is reflected in the excitation vector where

$$V_x^{\nu\mu} = \begin{cases} 1 \quad if \quad x_\nu = x_g \\ 0 \qquad Elsewhere \end{cases} \tag{2.49}$$

and

$$V_y^{\nu\mu} = \begin{cases} 1 \quad if \quad y_\mu = y_g \\ 0 \qquad Elsewhere \end{cases} \tag{2.50}$$

As will be discussed in section 2.5, the number and strength of the gap generators depends on the number of ports for the microstrip discontinuity.

At microwave frequencies, radiation from discontinuities introduces losses which dominate the conductor losses unless long line lengths are present [65],[66]. In this dissertation, conductor loss will be included and compared to radiation losses in an example of a meander delay line. In all other examples, perfect conductors will be considered ($\bar{E}_t(x, y, z = t) = 0$).

2.5 Determining N-port Network Parameters

The linear matrix equation may be solved for the electric current according to

$$\left[I \right] = \left[Z \right]^{-1} \left[V \right] \quad . \tag{2.51}$$

The solution for the current on the conducting strips of a T-junction discontinuity is shown in Figure 2.3. This current clearly shows the formation of standing waves and the edge effect. From the current distribution, the network parameters may be computed by transmission line theory assuming that a single microstrip mode is excited along the feeding line, which is a good approximation for practical (M)MIC substrates. The microstrip element may be represented as an N-port network (Figure 2.4) with the port voltages and currents related according to the expression

$$V_n = \sum_{m=1}^{N} Z_{nm} I_m \qquad \forall n \in (1, N) \tag{2.52}$$

where the elements Z_{nm} are commonly referred to as circuit impedance or [Z]-parameters. Dividing each voltage V_n by the corresponding current I_n results in the following expression for the input impedance Zin_n at port n.

$$Zin_n = \sum_{m=1}^{N} Z_{nm} (\frac{I_m}{I_n}) \quad . \tag{2.53}$$

The input impedances Zin_n (n=1,N) are determined at a given reference plane from the method of moments current solution. An N-port discontinuity has N^2 unknown

network parameters, and therefore, N^2 independent equations are required for the problem. These may be obtained from (2.53) after exciting the N-port microstrip element by N independent excitations. In addition, scattering parameters can be obtained from the [Z]-parameters by the well-known matrix equation

$$[S] = ([Z] - [I])([Z] + [I])^{-1} \tag{2.54}$$

The total radiation loss can be obtained from the scattering parameters according to

$$\frac{P_{rad}}{P_{in}} = 1 - \sum_{m=1}^{N} |S_{m1}|^2 \quad . \tag{2.55}$$

The radiation loss is frequently represented by the quantity G which is defined as

$$G = 1 - \frac{P_{rad}}{P_{in}} = \sum_{m=1}^{N} |S_{m1}|^2 \quad . \tag{2.56}$$

Many microstrip discontinuities (eg. bends, stubs), can be represented by two-port, symmetric networks. In this case, the number of excitations can be reduced to two with reciprocity and symmetry. For such examples, the [Z]-parameters may be written in the compact form according to

$$Z_{11} = \frac{Z_{in}^{1e} + Z_{in}^{1o}}{2} \tag{2.57}$$

$$Z_{22} = Z_{11} \tag{2.58}$$

$$Z_{12} = \frac{Z_{in}^{1o} - Z_{in}^{1e}}{2} \tag{2.59}$$

$$Z_{12} = Z_{21} \quad . \tag{2.60}$$

In the above, the quantity $Z_{in}^{1e(o)}$ is the input impedance at port 1 under an even(odd) excitation. An even excitation refers to equal sources at both ports, while an odd

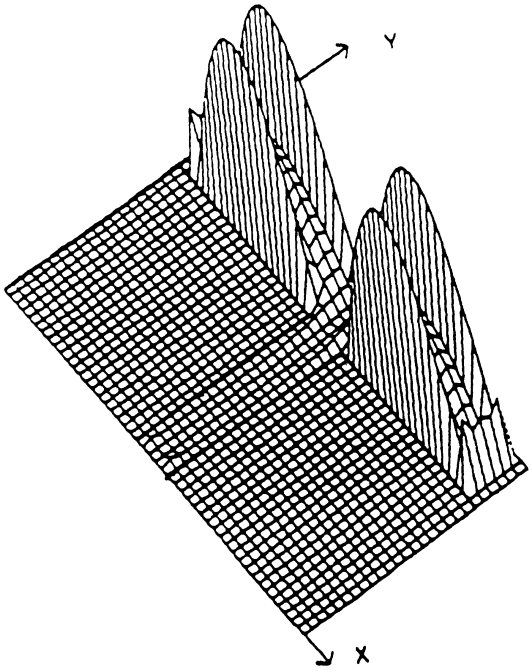

a. X-directed Current on Tee

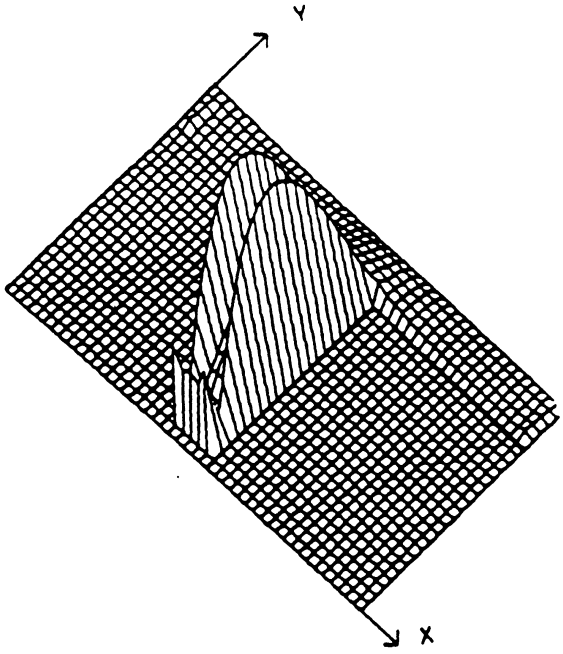

b. Y-directed Current on Tee

Figure 2.3: Current On T-Junction Excited by Gap Generators ($\epsilon_{r1} = 4, h_1 = .4mm, w = .2mm$)

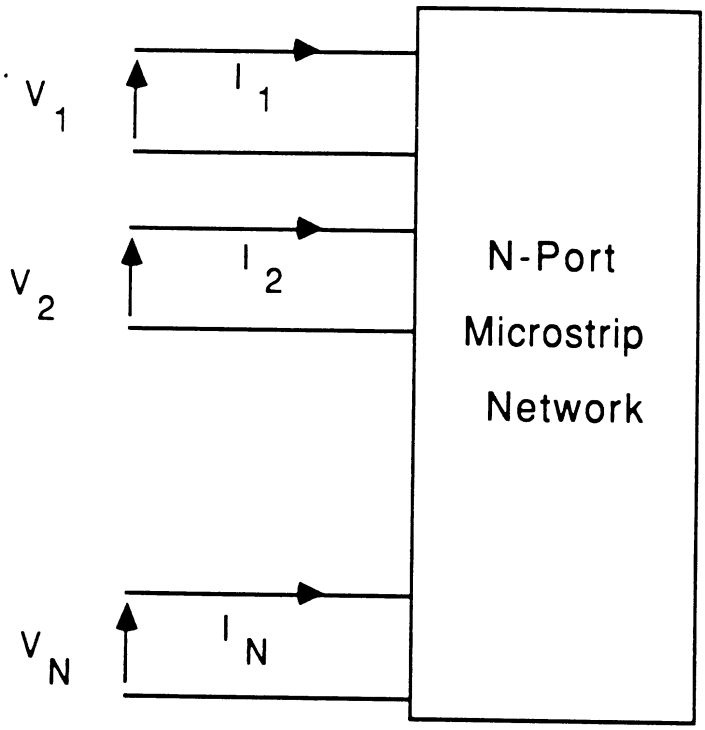

Figure 2.4: N-port Microstrip Network

excitation refers to sources of equal strength which are 180 degrees out of phase. The scattering parameters are then obtained from the [Z]-parameters according to

$$S_{11} = S_{22} = \frac{Z_{11}^2 - 1 - Z_{12}^2}{D} \tag{2.61}$$

$$S_{12} = S_{21} = \frac{2Z_{12}}{D} \tag{2.62}$$

with

$$D = Z_{11}^2 + 2Z_{11} - Z_{12}^2 \tag{2.63}$$

and the total radiation loss is given by

$$\frac{P_{rad}}{P_{in}} = 1 - |S_{11}|^2 - |S_{12}|^2 \tag{2.64}$$

2.6 Radiated Power and Surface Wave Patterns

The electromagnetic fields generated by the current on the microstrip element may be computed directly from the electric field integral equation after the microstrip current is known. This is done by a numerical integration of equation (2.16) after the current summations have been inserted. Performing this integration for the radiated fields at all spatial angles would be extremely time consuming, and is fortunately not necessary. To quantify the space and surface wave power losses, it is only necessary to obtain the far-field patterns. These may be obtained by an approximate saddle point integration, which is much less time-consuming than a full numerical integration of equation (2.16). Of course, to compute the near field power, as is required for characteristic impedance evaluation, a numerical integration of equation (2.16) is needed. In this section, the saddle point evaluation for the far-fields is presented. The analysis is done for a single substrate layer for clarification purposes without a loss of generality.

2.6.1 Space Waves

As shown in Figure 2.5(a), the original path of integration is along the positive real axis. The path contains a finite number of singularities, which correspond to excited surface waves, between the free space (k_0) and the highest dielectric (k) wavenumber. To obtain the radiated far-fields, the integral is transformed to the steepest descent plane by the complex mapping

$$\lambda = k_0 \sin \alpha \quad . \tag{2.65}$$

Figure 2.5(b) shows the new path of integration in the α-plane. The quantities shown in the parenthesis correspond to the points mapped from the λ-plane to the α-plane. The poles now lie along the line defined by $\mathrm{Re}(\alpha) = \pi/2$, between the points $\mathrm{Im}(\alpha) = 0$ and $\mathrm{Im}(\alpha) = \nu_k$. ν_k is mapped from the point k in the λ-plane according to

$$k = k_0 \sin(\pi/2 + j\nu_k) \tag{2.66}$$

$$\nu_k = \cosh^{-1}(\epsilon_r) \quad . \tag{2.67}$$

The Green's function may be represented as an integral over the entire real axis as shown in appendix B for a single dielectric layer. To find the far-field patterns, these components of the of the Green's function are transformed to spherical coordinates according to

$$\rho = r \sin \theta \tag{2.68}$$

$$z = r \cos \theta \tag{2.69}$$

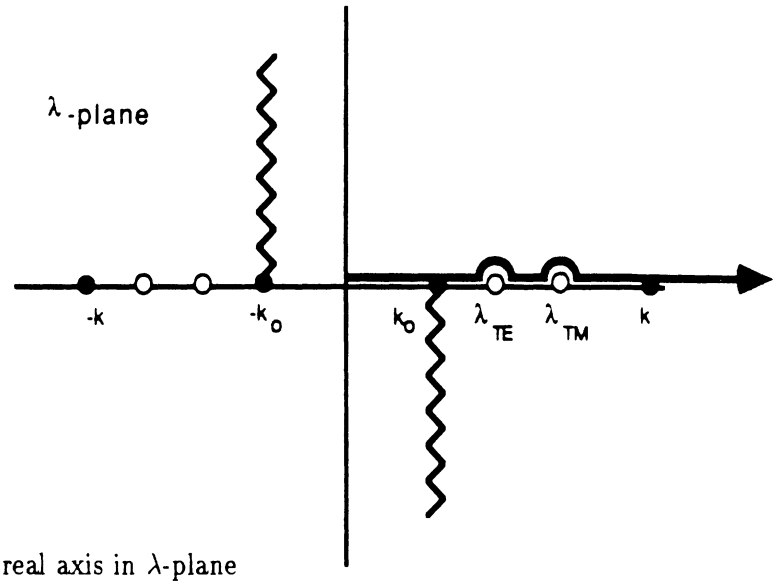

a. Integration along real axis in λ-plane

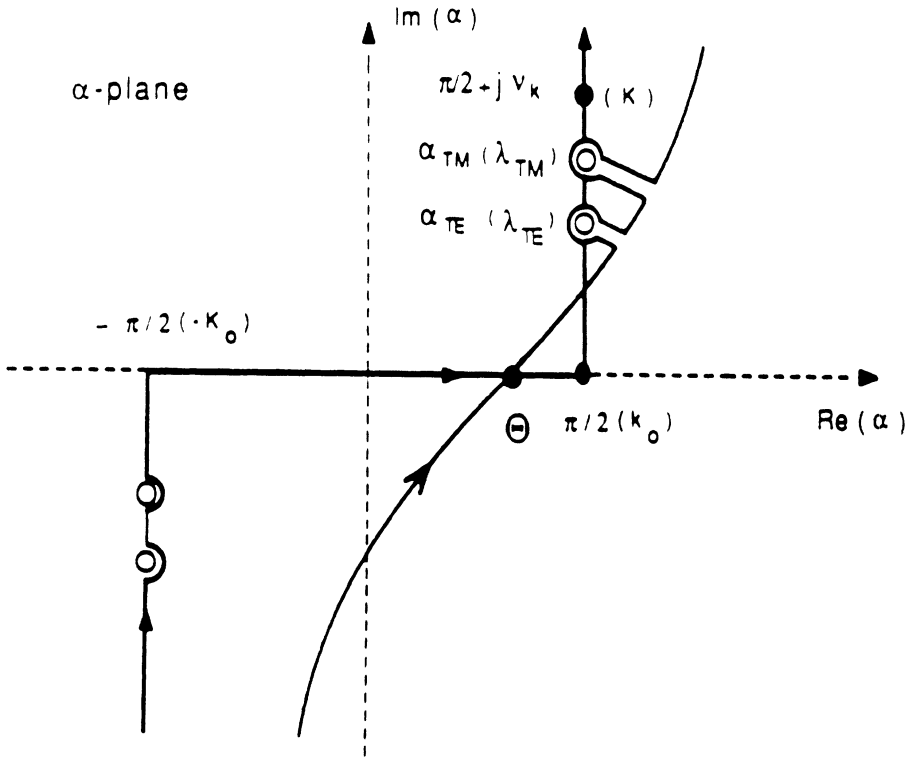

b. Contour of integration in α-plane

Figure 2.5: Integration Paths

After substitution of equations (2.68) and (2.69) into (B.1), the form of the Green's function becomes

$$G_{xx} = G_{yy} = -\frac{j\omega\mu_o}{4\pi k_0^2}\int_{-\infty}^{\infty} H_0^{(1)}(rk_0\sin(\theta)\sin(\alpha))e^{-jk_0r\cos(\theta)\cos(\alpha)} \frac{j\sin(k_0h\sqrt{\epsilon_r-\sin(\alpha)^2})}{f_1(\alpha)}k_0^2\cos(\alpha)\sin(\alpha)d\alpha$$

$$G_{zx} = \tan\phi G_{zy} = -\frac{j\omega\mu_o}{4\pi k_0^2}(1-\epsilon_r)\cos(\phi)\int_{-\infty}^{\infty} H_1^{(1)}(rk_0\sin(\theta)\sin(\alpha))e^{-jk_0r\cos(\theta)\cos(\alpha)} \frac{j\sin(k_0h\sqrt{\epsilon_r-\sin(\alpha)^2})\cos(k_0h\sqrt{\epsilon_r-\sin(\alpha)^2})}{f_1(\alpha)f_2(\alpha)}k_0^3\cos(\alpha)\sin(\alpha)^2$$

with the surface wave characteristic equations taking the form

$$f_1(\alpha) = -k_0\cos(\alpha)\sin(k_0h\sqrt{\epsilon_r-\sin(\alpha)^2})+jk_0\sqrt{\epsilon_r-\sin(\alpha)^2}\cos(k_0h\sqrt{\epsilon_r-\sin(\alpha)^2}) \tag{2.71}$$

for TE surface waves, and

$$f_2(\alpha) = -k_0\sqrt{\epsilon_r-\sin(\alpha)^2}\sin(k_0h\sqrt{\epsilon_r-\sin(\alpha)^2})+jk_0\epsilon_r\cos(\alpha)\cos(k_0h\sqrt{\epsilon_r-\sin(\alpha)^2}) \tag{2.72}$$

for TM surface waves. Since far-field patterns($rk_0 >> 1$) are desired, the Hankel functions may be replaced by their respective large argument approximations

$$H_0^{(1)}(rk_0\sin(\theta)\sin(\alpha)) = \sqrt{\frac{2j}{\pi rk_0}}\frac{e^{-jrk_0\sin(\theta)\sin(\alpha)}}{\sqrt{\sin(\theta)\sin(\alpha)}} \tag{2.73}$$

$$H_1^{(1)}(rk_0\sin(\theta)\sin(\alpha)) = \sqrt{\frac{2j}{\pi rk_0}}\frac{je^{-jrk_0\sin(\theta)\sin(\alpha)}}{\sqrt{\sin(\theta)\sin(\alpha)}} \quad . \tag{2.74}$$

The contour of integration (Figure 2.5(b)) is then deformed into the steepest descent path[53]. During this contour deformation, a finite number of surface wave simple pole singularities are captured as shown in the figure. The green's function is now of the form

$$G_{xx} = G_{yy} = -\frac{j\omega\mu_o}{4\pi}\sqrt{\frac{2j}{\pi rk_0}}\left\{\int_{-\infty}^{\infty}\frac{jF(\alpha)}{f_1(\alpha)}e^{-jk_0r\cos(\theta-\alpha)}d\alpha \right. \tag{2.75}$$

$$+ \sum_{1}^{NTE} 2\pi j \left[\frac{\alpha-\alpha_{te}}{f_1(\alpha)}\right]_{\alpha=\alpha_{te}} F(\alpha_{te}) e^{-jk_0 r\sin(\theta-\alpha_{te})}\Bigg\}$$

$$G_{zx} = \tan\phi G_{zy} = -\frac{j\omega\mu_o}{4\pi}\sqrt{\frac{2j}{\pi r k_0}}\Bigg\{(1-\epsilon_r)\cos(\phi)\int_{-\infty}^{\infty}\frac{G(\alpha)e^{-jk_0 r\cos(\theta-\alpha)}}{f_1(\alpha)f_2(\alpha)}d\alpha$$
$$+ \sum_{1}^{NTM} 2\pi j\left[\frac{\alpha-\alpha_{tm}}{f_2(\alpha)}\right]_{\alpha=\alpha_{tm}}\frac{G(\alpha_{tm})}{f_1(\alpha_{tm})}e^{-jk_0 r\sin(\theta-\alpha_{tm})} \qquad (2.76)$$
$$+ \sum_{1}^{NTE} 2\pi j\left[\frac{\alpha-\alpha_{te}}{f_1(\alpha)}\right]_{\alpha=\alpha_{te}}\frac{G(\alpha_{te})}{f_1(\alpha_{te})}\}e^{-jk_0 r\sin(\theta-\alpha_{te})}\Bigg\}$$

with .

$$F(\alpha) = \frac{\sin(\alpha)\cos(\alpha)}{\sqrt{\sin(\theta)\sin(\alpha)}} j\sin(k_0 h\sqrt{\epsilon_r - \sin(\alpha)^2}) \qquad (2.77)$$

$$G(\alpha) = -\frac{\sin(\alpha)^2\cos(\alpha)}{\sqrt{\sin(\theta)\sin(\alpha)}}\sin(k_0 h\sqrt{\epsilon_r-\sin(\alpha)^2})\cos(k_0 h\sqrt{\epsilon_r-\sin(\alpha)^2}) \quad . \quad (2.78)$$

The summations correspond to the excited surface wave modes (NTM,NTE) and will be discussed further in the following section.

A saddle point integration is now performed on the above integrals, with the saddle point equal to the spherical observation angle ($\alpha = \theta$). The contribution of the saddle point is given by

$$G_{xx} = \frac{j\omega\mu_o}{2\pi}\frac{e^{(-jk_0 R)}}{k_0 R}\frac{F(\theta)}{f_1(\theta,h)}e^{(jk_0[x'\sin(\theta)\cos(\phi)+y'\sin(\theta)\sin(\phi)])} \qquad (2.79)$$

$$G_{zx} = \frac{j\omega\mu_o}{2\pi}(1-\epsilon_r)\cos(\phi)\frac{e^{(-jk_0 R)}}{k_0 R}\frac{jG(\theta)}{f_1(\theta,h)f_2(\theta,h)} \qquad (2.80)$$
$$e^{(jk_0[x'\sin(\theta)\cos(\phi)+y'\sin(\theta)\sin(\phi)])} \quad .$$

These expressions give the far-field space wave patterns above the substrate . These space waves are spherical waves in nature as seen by their spatial dependence $\frac{e^{(-jk_0 R)}}{k_0 R}$. In the phase terms of the above expressions

$$R = r + (x'\sin(\theta)\cos(\phi) + y'\sin(\theta)\sin(\phi)) \qquad (2.81)$$

and in the amplitude terms r has been replaced by R.

To obtain the fields for a microstrip discontinuity, one returns to the electric field integral equation. In the far-field, the electric field density can be written in spherical coordinates as

$$E_\theta = k_0^2[\pi_\theta^x + \pi_\theta^y] \tag{2.82}$$

$$E_\phi = k_0^2[\pi_\phi^x + \pi_\phi^y] \tag{2.83}$$

with

$$\begin{aligned}
\pi_\theta^x &= \int\int_{S'}[G_{xx}\cos(\theta)\cos(\phi) - G_{zx}\sin(\theta)]J_x(x',y')dx'dy' \\
\pi_\theta^y &= \int\int_{S'}[G_{yy}\cos(\theta)\sin(\phi) - G_{zy}\sin(\theta)]J_y(x',y')dx'dy' \\
\pi_\phi^x &= \int\int_{S'}[-G_{xx}\sin(\phi)]J_x(x',y')dx'dy' \\
\pi_\phi^y &= \int\int_{S'}[G_{yy}\cos(\phi)]J_y(x',y')dx'dy'
\end{aligned} \tag{2.84}$$

Inserting the results of the saddle point analysis from equations (2.79) and (2.80), and the summations for the microstrip current (equations (2.22) and (2.23)), the electric field can be written in the form

$$\begin{aligned}
E_\theta &= \frac{j\omega\mu_o}{2\pi}k_0^2\frac{e^{(-jk_0R)}}{k_0R}[\frac{F(\theta)}{f_1(\theta,h)}\cos(\theta) - \frac{jG(\theta)(1-\epsilon_r)}{f_1(\theta,h)f_2(\theta,h)}\sin(\theta)] \\
&\quad [A_{rx}(\theta,\phi)\cos(\phi) + A_{ry}(\theta,\phi)\sin(\phi)] \\
E_\phi &= -\frac{j\omega\mu_o}{2\pi}k_0^2\frac{e^{(-jk_0R)}}{k_0R}\frac{F(\theta)}{f_1(\theta,h)}[A_{rx}(\theta,\phi)\sin(\phi) - A_{ry}(\theta,\phi)\cos(\phi)]
\end{aligned}$$

where the terms $A_{rx}(\theta,\phi)$ and $A_{ry}(\theta,\phi)$ contain the spatial integrations of the product between basis functions and the phase of the appropriate Green's function components. These integrations are performed analytically and result in the expressions given below

$$A_{rx}(\theta,\phi) = 4e^{(jK_0\frac{1}{2}\sin(\theta)\sin(\phi))}[\sum_{n=1}^{N+1}\sum_{m=1}^{M+1}I_{nm}^x e^{(jy_mK_0\sin(\theta)\sin(\phi))}e^{(jx_nK_0\sin(\theta)\cos(\phi))}]$$

$$\frac{\sin\left(K_0\frac{l}{2}\sin(\theta)\sin(\phi)\right)}{K_0\sin(\theta)\sin(\phi)}\frac{\cos(lK_0\sin(\theta)\cos(\phi))-\cos(k_s l)}{K_s\sin(K_s l)[1-(\frac{K_0}{k_s})^2(\sin(\theta)\cos(\phi))^2]} \quad (2.85)$$

$$A_{ry}(\theta,\phi) = 4e^{(jK_0\frac{l}{2}\sin(\theta)\cos(\phi))}\left[\sum_{n=1}^{N+1}\sum_{m=1}^{M+1} I^y_{nm} e^{(jy_m K_0\sin(\theta)\sin(\phi))} e^{(jx_n K_0\sin(\theta)\sin(\phi))}\right]$$

$$\frac{\sin\left(K_0\frac{l}{2}\sin(\theta)\cos(\phi)\right)}{K_0\sin(\theta)\cos(\phi)}\frac{\cos(lK_0\sin(\theta)\sin(\phi))-\cos(k_s l)}{K_s\sin(K_s l)[1-(\frac{K_0}{k_s})^2(\sin(\theta)\sin(\phi))^2]} \quad (2.86)$$

where the quantities l and k_s represent the subsection length and scaling constant for the basis functions, respectively.

There are two contributions to the radiated fields: A substrate factor, resulting from the Green's function and containing all the information about the substrate; and a shaping factor, resulting from the spatial dependence of the source and containing all the information about the shape and current distribution over the conducting strips. Consequently, these two factors may be handled independently to reduce losses.

The total far-field space wave power is obtained by integrating the Poynting vector over a hemisphere centered around the discontinuity as shown in figure 2.6 (a).

$$P_r^{sp} = \frac{1}{2}\int_0^{2\pi}\int_0^{\frac{\pi}{2}}\left[\frac{E_\theta^2}{\eta_0}+\frac{E_\phi^2}{\eta_0}\right] r\sin(\theta)d\theta d\phi \quad . \quad (2.87)$$

2.6.2 Surface Waves

During the contour deformation of the previous section, a finite number of singularities were captured as shown in Figure 2.5. These singularities correspond to excited surface wave modes that fall into two types: a) Transverse Electric (TE_z), or b) Tranverse Magnetic (TM_z) to the dielectric-air interface. The poles are determined by the zeroes of two analytic functions in the denominator of the Green's

function given by

$$f_1(\alpha) = -\cos(\alpha)\sin(k_0 h\sqrt{\epsilon_r - \sin(\alpha)^2}) + j\sqrt{\epsilon_r - \sin(\alpha)^2}\cos(k_0 h\sqrt{\epsilon_r - \sin(\alpha)^2}) \tag{2.88}$$

for (TE_z) waves, and

$$f_2(\alpha) = -\sqrt{\epsilon_r - \sin(\alpha)^2}\sin(k_0 h\sqrt{\epsilon_r - \sin(\alpha)^2}) + j\epsilon_r\cos(\alpha)\cos(k_0 h\sqrt{\epsilon_r - \sin(\alpha)^2}) \tag{2.89}$$

for (TM_z) waves. It is now a simple matter to obtain field patterns in the dielectric $(\theta = \pi/2)$ by the application of Cauchy's residue theorem. The total number of poles is determined by the operating frequency and the substrate parameters, and can be determined by a search for zeroes in equations (2.88) and (2.89). The pole locations are given by

$$\alpha_{TM} = \frac{\pi}{2} + j\nu_n \quad n = 1, N_{TM} \tag{2.90}$$

$$\alpha_{TE} = \frac{\pi}{2} + j\nu_m \quad m = 1, N_{TE} \tag{2.91}$$

where N_{TM} and N_{TE} are the number of excited TM and TE modes, respectively. The far-fields are determined by computing the residues of the singularities and are given in Appendix C.

The power in a particular mode is found from the Poynting vector. The surface wave power at the dielectric interface is given by

$$P_r^{TM}(\phi) = \sum_{n=0}^{NTM} \frac{k_0^2\omega\mu_0}{4\pi}\frac{[\epsilon_r - cosh^2(\nu_n)]cosh^2(\nu_n)sinh^2(\nu_n)}{|f_2'(\alpha)|^2|_{\pi/2+j\nu_n}}(\sin(k_0 h\sqrt{\epsilon_r - \sin(\alpha)^2}))^2$$
$$|\cos(\phi)A_{rx}(\phi) + \sin(\phi)A_{ry}(\phi)|^2 \tag{2.92}$$

for TM waves, and

$$P_r^{TE}(\phi) = \sum_{m=0}^{NTE} \frac{k_0^2\omega\mu_0}{4\pi}\frac{cosh^2(\nu_m)sinh^2(\nu_m)}{|f_1'(\alpha)|^2|_{\pi/2+j\nu_m}}(\sin(k_0 h\sqrt{\epsilon_r - \sin(\alpha)^2}))^2$$
$$|\sin(\phi)A_{rx}(\phi) + \cos(\phi)A_{ry}(\phi)|^2 \tag{2.93}$$

for TE waves. In equations (2.92) and (2.93) the terms $A_{rx}(o)$ and $A_{ry}(o)$ are given by equations (2.85) and (2.86), with the quantity $k_0 \cosh(\nu_n)$ replacing $k_0 \sin(\theta)$.

The total power in TM and TE modes may be found by integrating the Poynting vector over a cylindrical surface centered at the discontinuity as shown in figure 2.6 (b).

$$P_r^{TM} = -\int_{-h}^{\infty}\int_{0}^{2\pi} \frac{E_z \cdot H_\phi^*}{2} \rho d\phi dz \tag{2.94}$$

$$P_r^{TE} = \int_{-h}^{\infty}\int_{0}^{2\pi} \frac{E_\phi \cdot H_z^*}{2} \rho d\phi dz. \tag{2.95}$$

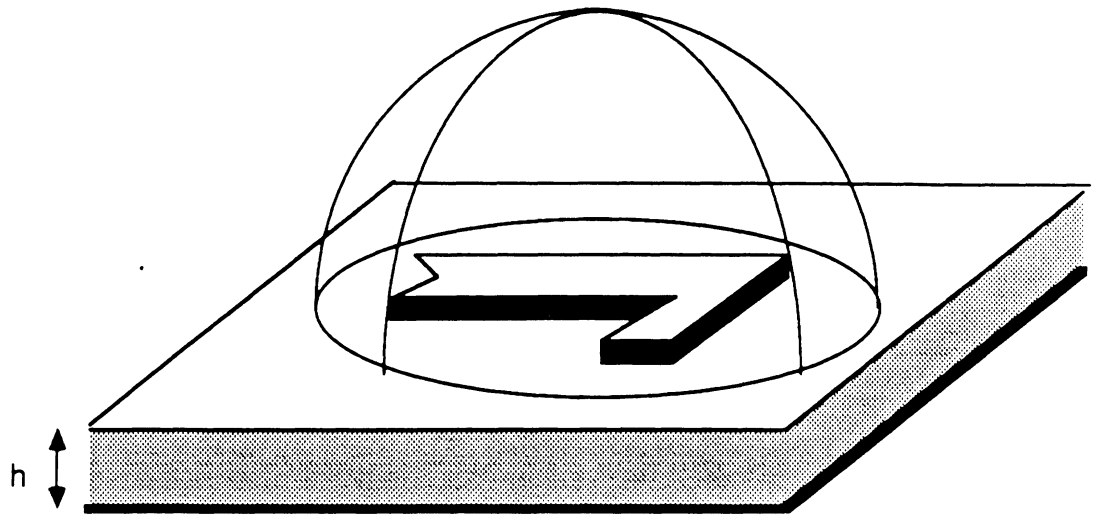

a. Integration plane for space wave radiation

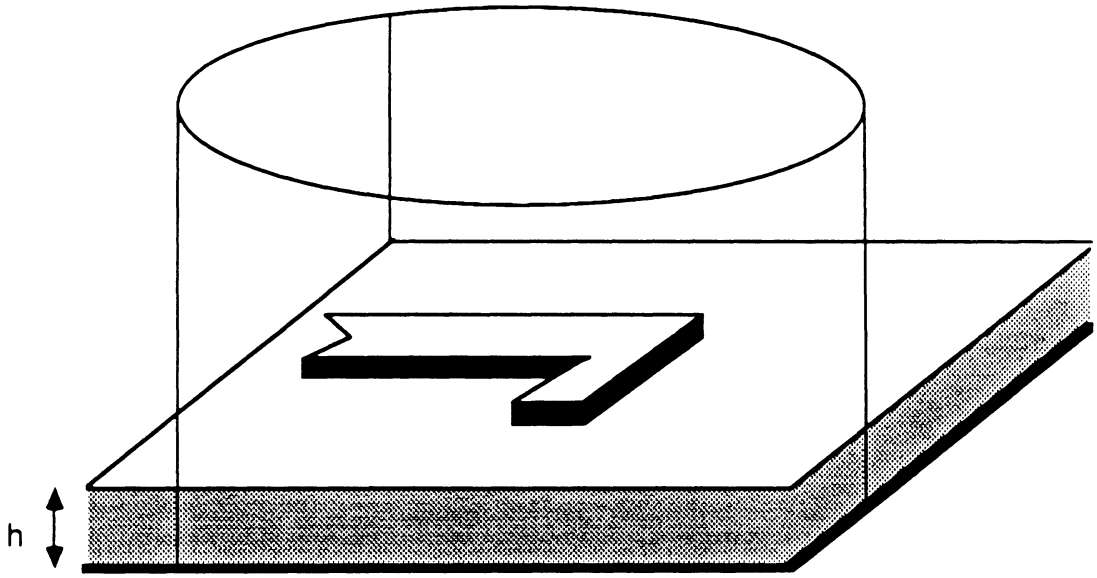

b. Integration plane for surface wave radiation

Figure 2.6: Integration Planes

CHAPTER III

NUMERICAL CONSIDERATIONS

3.1 Evaluation of the Impedance Matrix

The evaluation of the impedance matrix requires the majority of analytical and numerical effort for this problem. The elements contain quadruple spatial integrals shown in equation (2.40), as well as the semi-infinite Sommerfeld integrals in the Green's function. A real axis integration of the Sommerfeld integrals is performed as discussed in section 3.1.1. The evaluation of the quadruple space integrals is discussed in sections 3.1.2 and 3.1.3. Techniques for filling the matrix with the minimum computational effort are discussed in section 3.2.

An important aspect of all numerical problems is the accuracy and stability of the numerical solution. In section 3.4, two types of numerical convergence are investigated. Results will be presented which show the optimal choices of numerical parameters for a desired level of accuracy.

3.1.1 Sommerfeld Integrals

The Sommerfeld integrals are computed by a real-axis integration in the complex λ-plane[54] using an extraction of the singularities technique which effectively takes into account the contribution from the simple poles in the integrand (see Figure

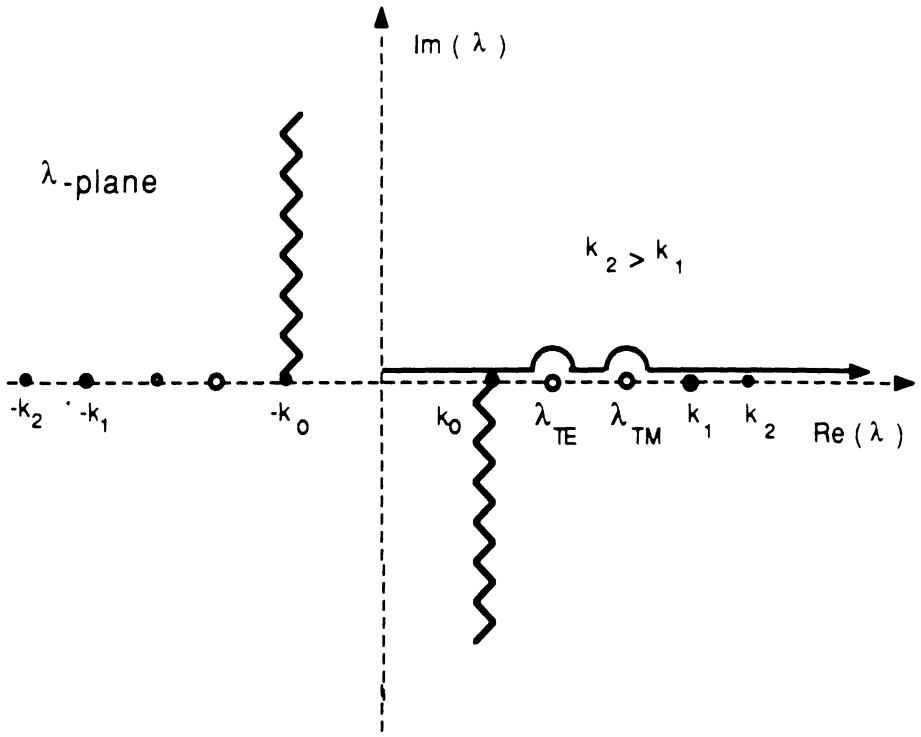

Figure 3.1: Real Axis Integration of Sommerfeld Integral

3.1). As has been mentioned in the previous chapter, for a lossless substrate these poles lie on the real axis between the free space wavenumber (k_0) and the highest wavenumber of the other layers ($MAX(k_1, k_2)$). The residues of the poles correspond to radiated power in the form of TM and TE modes propagating within the substrate layer. For the grounded substrate configuration, the TM_0 surface wave mode has no cutoff frequency. For monolithic arrays and (M)MICS, it is desirable to operate at frequencies where higher order surface waves are not excited to avoid excessive radiation losses. Nevertheless, high radiation losses may also be encountered at frequencies where only the dominant surface wave mode is excited.

The semi-infinite Sommerfeld integrals are divided into two regions with respect

to λ, and a combination of numerical and analytical techniques are employed to evaluate the integrals in each region separately. The first region extends from 0 to the parameter A, and the second from [A-∞). The parameter A is chosen to satisfy the condition

$$A_t = \tanh\left(\sqrt{A^2 - k_i^2}\, h_i\right) \doteq 1 \tag{3.1}$$

where the index (i) refers to the electrically thinnest dielectric layer adjacent to the microstrip structure. When λ is greater than A, simplifications are made in the integrand which result in improved accuracy and reduced computational effort.

In view of the above, the elements of the impedance matrix may be written as

$$Z_{\xi\zeta} = Z_{\xi\zeta}^{A} + Z_{\xi\zeta}^{\infty} \qquad \xi, \zeta = x, y. \tag{3.2}$$

3.1.2 Evaluation of the quadruple spatial integrals from [0-A]

Considering equations (2.31),(2.40), and (3.1), $Z_{\xi\zeta}^{A}(n, m, \nu, \mu)$ is given by the following expression:

$$\begin{aligned} Z_{\xi\zeta}^{A}(n, m, \nu, \mu) &= \delta_{\xi\zeta}\, \mathcal{L}_{\xi\xi}(A)\, \langle f_{n_\xi} g_{m_\xi},\, J_0(\lambda\rho),\, f_{\nu_\zeta} g_{\mu_\zeta} \rangle \\ &+ \mathcal{R}_{\xi\zeta}(A)\, \langle f_{n_\xi} g_{m_\xi},\, \frac{\partial^2}{\partial\xi\partial\zeta} J_0(\lambda\rho),\, f_{\nu_\zeta} g_{\mu_\zeta} \rangle \end{aligned} \tag{3.3}$$

where $\mathcal{L}_{\xi\xi}(A)$ and $\mathcal{R}_{\xi\zeta}(A)$ are integral operators given by

$$\mathcal{L}_{\xi\xi}(A) = k_i^2 \int_0^A d\lambda f_{\xi\xi} \tag{3.4}$$

$$\mathcal{R}_{\xi\zeta}(A) = \int_0^A d\lambda (f_{\zeta\zeta} + f_{z\zeta}). \tag{3.5}$$

The real-axis evaluation of the Sommerfeld integrals with simple pole singularities is given in [54]. As mentioned, the numerical evaluation of the double inner products containing quadruple integrals would result in unacceptable numerical error and excessive CPU time. This difficulty has been overcome by transforming the integrals

to convergent series. This is accomplished by representing the Bessel function in equation (3.3) in its integral form, and combining it with the trigonometric functions in the basis functions. The Bessel function and its derivatives may be written as

$$J_0(\lambda\rho) = \frac{1}{2\pi}\int_{-\pi}^{\pi} e^{j\lambda(x-x')\cos\phi} e^{j\lambda(y-y')\sin\phi} d\phi \tag{3.6}$$

$$\frac{\partial^{\sigma+\tau}}{\partial x^{\sigma}\partial y^{\tau}} J_0(\lambda\rho) = \frac{1}{2\pi}\int_{-\pi}^{\pi} (j\lambda\cos\phi)^{\sigma}(j\lambda\sin\phi)^{\tau} e^{j\lambda(x-x')\cos\phi} e^{j\lambda(y-y')\sin\phi} d\phi \tag{3.7}$$

Employing these relations the quadruple integrals can be reduced to convergent series as shown in Appendix D. These series are of the form

$$\langle f_{n_\xi} g_{m_\xi},\ J_0(\lambda\rho),\ f_{\nu_\xi} g_{\mu_\xi}\rangle \tag{3.8}$$
$$= \sum_{k=0}^{\infty}\sum_{k'=0}^{\infty}\sum_{l=0}^{\infty}\sum_{l'=0}^{\infty} A_{2k}A_{2k'}B_lB_{l'}(-1)^{k+k'}(-j)^{l+l'} \frac{\partial^{2(k+k')+(l+l')} J_0(\lambda\rho)}{(\partial|\xi-\xi'|)^{2(k+k')}(\partial|\zeta-\zeta'|)^{(l+l')}}$$

$$\langle f_{n_\xi} g_{m_\xi},\ \frac{\partial^2}{\partial\xi^2} J_0(\lambda\rho),\ f_{\nu_\xi} g_{\mu_\xi}\rangle \tag{3.9}$$
$$= \sum_{k=0}^{\infty}\sum_{k'=0}^{\infty}\sum_{l=0}^{\infty}\sum_{l'=0}^{\infty} A_{2k}A_{2k'}B_lB_{l'}(-1)^{k+k'}(-j)^{l+l'} \frac{\partial^{2(k+k'+1)+(l+l')} J_0(\lambda\rho)}{(\partial|\xi-\xi'|)^{2(k+k'+1)}(\partial|\zeta-\zeta'|)^{(l+l')}}$$

$$\langle f_{n_\xi} g_{m_\xi},\ \frac{\partial^2}{\partial\xi\partial\zeta} J_0(\lambda\rho),\ f_{\nu_\zeta} g_{\mu_\zeta}\rangle \tag{3.10}$$
$$= \sum_{k=0}^{\infty}\sum_{k'=0}^{\infty}\sum_{l=0}^{\infty}\sum_{l'=0}^{\infty} A_{2k}A_{2k'}B_lB_{l'}(-1)^{k+k'}(-j)^{l+l'} \frac{\partial^{2(k+k'+1)+(l+l')} J_0(\lambda\rho)}{(\partial|\xi-\xi'|)^{(2k+l'+1)}(\partial|\zeta-\zeta'|)^{(2k'+l+1)}}.$$

where $\xi,\zeta = x,y(\xi \neq \zeta)$, and $\rho = \sqrt{(\xi_{\nu_\xi} - \xi_{n_\xi})^2 + (\zeta_{\mu_\zeta} - \zeta_{m_\zeta})^2}$. Although these summations result in a considerable reduction of computations, they still require the vast majority of CPU time.

3.1.3 Evaluation of the quadruple spatial integrals from [A-∞]

The contribution for the interval of the semi-infinite Sommerfeld integral from [A ,∞) can be written as

$$Z_{xx}^{(\infty)} = \langle f_{n_x} g_{m_x},\ \mathcal{K}_{xx}^{(\infty)},\ f_{\nu_x} g_{\mu_x}\rangle \tag{3.11}$$

$$Z_{xy}^{(\infty)} = \langle f_{n_x} g_{m_x}, \mathcal{K}_{xy}^{(\infty)}, f_{\nu_y} g_{\mu_y} \rangle \tag{3.12}$$

$$Z_{yx}^{(\infty)} = \langle f_{n_y} g_{m_y}, \mathcal{K}_{yx}^{(\infty)}, f_{\nu_x} g_{\mu_x} \rangle \tag{3.13}$$

$$Z_{yy}^{(\infty)} = \langle f_{n_y} g_{m_y}, \mathcal{K}_{yy}^{(\infty)}, f_{\nu_y} g_{\mu_y} \rangle \tag{3.14}$$

where

$$\mathcal{K}_{\xi\zeta}^{(\infty)} = \int_A^\infty \left[(k_i^2 \delta_{\xi\zeta} + \frac{\partial^2}{\partial\xi\partial\zeta}) f_{\zeta\zeta} + \frac{\partial^2}{\partial\xi\partial\zeta} f_{z\zeta} \right] J_0(\lambda\rho) d\lambda \quad . \tag{3.15}$$

When A is chosen according to equation (3.1), simplifications may be made in the integrand of the Green's function resulting in the expressions

$$\mathcal{K}_{\xi\zeta}^{(\infty)} = \mathcal{H}_{\xi\zeta}^{(\infty)} - \mathcal{H}_{\xi\zeta}^{(A)} \tag{3.16}$$

where

$$\mathcal{H}_{\xi\zeta}^{(\infty)} = \left\{ h_{\zeta\zeta} \left[\delta_{\xi\zeta} + \frac{\partial^2}{\partial\xi\partial\zeta} \right] + h_{z\zeta} \frac{\partial^2}{\partial\xi\partial\zeta} \right\} \frac{1}{\sqrt{\rho^2 + \left(\frac{t}{f(A)}\right)^2}} \tag{3.17}$$

and

$$\mathcal{H}_{\xi\zeta}^{(A)} = \int_0^A d\lambda \left[h_{\zeta\zeta} (\delta_{\xi\zeta} + \frac{\partial^2}{\partial\xi\partial\zeta}) + h_{z\zeta} \frac{\partial^2}{\partial\xi\partial\zeta} \right] J_0(\lambda\rho) \frac{e^{-\lambda t f(A)}}{f(A)}. \tag{3.18}$$

In equations (3.17) and (3.18), $f(A)$, $h_{\zeta\zeta}$, and $h_{z\zeta}$ are constants given by

$$h_{\zeta\zeta} = \frac{\omega\mu_0}{2\pi k_0^2} \frac{1}{2\left[1 - \epsilon_2(A)\right] f(A)} \tag{3.19}$$

$$h_{z\zeta} = \frac{\omega\mu_0}{2\pi k_0^2} \frac{1}{2f(A)} \left(\frac{1}{\left[1 - \epsilon_2(A)\right]} - \frac{2}{\left[(\epsilon_{rA} + \epsilon_{r1})(1 - \epsilon_3(A))\right]} \right) \tag{3.20}$$

with

$$f(A) = \sqrt{1 + \frac{k_1^2}{A^2 - k_1^2}} \tag{3.21}$$

$$\epsilon_2(A) = \frac{k_2^2 - k_1^2}{4(A^2 - k_1^2)} \tag{3.22}$$

$$\epsilon_3(A) = \frac{\epsilon_{r1}}{2(\epsilon_{r1} + \epsilon_{r2})} \frac{k_2^2 - k_1^2}{4(A^2 - k_1^2)} \tag{3.23}$$

for the case of a superstrate/substrate configuration. When the superstrate is not present, the quantities ϵ_{r1}, and ϵ_{r2} are replaced by ϵ_{r0}, and ϵ_{r1}, respectively.

Substitution of (3.16) into (3.11)-(3.14) gives

$$Z_{\xi\zeta}^{(\infty)} = \langle f_{n_\xi} g_{m_\xi},\ \mathcal{H}_{\xi\zeta}^{(\infty)},\ f_{\nu_\zeta} g_{\mu_\zeta} \rangle - \langle f_{n_\xi} g_{m_\xi},\ \mathcal{H}_{\xi\zeta}^{(A)},\ f_{\nu_\zeta} g_{\mu_\zeta} \rangle \tag{3.24}$$

where the quantity containing $\mathcal{H}_{\xi\zeta}^{(A)}$ can be handled in exactly the same manner as $Z_{\xi\zeta}^{A}$. Substitution of equation(3.17) into (3.24) for the quantity $\mathcal{H}_{\xi\zeta}^{(\infty)}$ gives

$$\langle f_{n_\xi} g_{m_\xi},\ \dot{\mathcal{H}}_{\xi\zeta}^{(\infty)},\ f_{\nu_\zeta} g_{\mu_\zeta} \rangle = \delta_{\xi\zeta} h_{\zeta\zeta} \langle f_{n_\xi} g_{m_\xi},\ \frac{1}{\sqrt{\rho^2 + \frac{t}{f(A)}^2}},\ f_{\nu_\xi} g_{\mu_\xi} \rangle \tag{3.25}$$

$$+\ h_{\zeta\zeta} \langle f_{n_\xi} g_{m_\xi},\ \frac{\partial^2}{\partial \xi^2} \frac{1}{\sqrt{\rho^2 + \frac{t}{f(A)}^2}},\ f_{\nu_\xi} g_{\mu_\xi} \rangle + h_{z\zeta} \langle f_{n_\xi} g_{m_\xi},\ \frac{\partial^2}{\partial \xi \partial \zeta} \frac{1}{\sqrt{\rho^2 + \left(\frac{t}{f(A)}\right)^2}},\ f_{\nu_\zeta} g_{\mu_\zeta} \rangle$$

The derivatives present in the double inner products can be eliminated through integration by parts, resulting in the expressions

$$\begin{aligned} &\langle f_{n_\xi} g_{m_\xi},\ \frac{\partial^2}{\partial \xi^2} \frac{1}{\sqrt{\rho^2 + \frac{t}{f(A)}^2}},\ f_{\nu_\xi} g_{\mu_\xi} \rangle \\ &= \int_{\zeta_{m_\xi}}^{\zeta_{m_\xi+1}} d\zeta' \int_{\zeta_{\mu_\xi}}^{\zeta_{\mu_\xi+1}} d\zeta \int_{-l_\xi}^{l_\xi} d\xi \sin\left(k_s(l_\xi - |\xi|)\right) \\ &\cdot \left(\frac{1}{\sqrt{\rho_A^2 + \left(\frac{t}{f(A)}\right)^2}} + \frac{1}{\sqrt{\rho_B^2 + \left(\frac{t}{f(A)}\right)^2}} - \frac{2\cos(k_s l_\xi)}{\sqrt{\rho_C^2 + \left(\frac{t}{f(A)}\right)^2}} \right) \end{aligned} \tag{3.26}$$

and

$$\begin{aligned} &\langle f_{n_\xi} g_{m_\xi},\ \frac{\partial^2}{\partial \xi \partial \zeta} \frac{1}{\sqrt{\rho^2 + \left(\frac{t}{f(A)}\right)^2}},\ f_{\nu_\zeta} g_{\mu_\zeta} \rangle \\ &= \int_{-l_\xi}^{l_\xi} d\xi \int_{-l_\zeta}^{l_\zeta} d\zeta' \sin\left(k_s(l_\xi - |\xi|)\right) \sin\left(k_s(l_\zeta - |\zeta'|)\right) \\ &\left(\frac{1}{\sqrt{\rho_D^2 + \left(\frac{t}{f(A)}\right)^2}} + \frac{1}{\sqrt{\rho_E^2 + \left(\frac{t}{f(A)}\right)^2}} - \frac{1}{\sqrt{\rho_F^2 + \left(\frac{t}{f(A)}\right)^2}} - \frac{1}{\sqrt{\rho_G^2 + \left(\frac{t}{f(A)}\right)^2}} \right) \end{aligned} \tag{3.27}$$

In equations (3.26) and (3.27), ρ_{A-G} are functions of ξ and ζ given by

$$\begin{aligned}
\rho_A^2 &= (\zeta - \zeta')^2 + (\xi + \xi_{\nu_\xi} - \xi_{n_\xi} + l_\xi)^2 \\
\rho_B^2 &= (\zeta - \zeta')^2 + (\xi + \xi_{\nu_\xi} - \xi_{n_\xi} - l_\xi)^2 \\
\rho_C^2 &= (\zeta - \zeta')^2 + (\xi + \xi_{\nu_\xi} - \xi_{n_\xi})^2 \\
\rho_D^2 &= (l_\zeta - \zeta' + \zeta_{\mu_\xi} - \zeta_{m_\zeta})^2 + (\xi + \xi_{\nu_\xi} - \xi_{n_\zeta})^2 \\
\rho_E^2 &= (-\zeta' + \zeta_{\mu_\xi} - \zeta_{m_\zeta})^2 + (\xi + \xi_{\nu_\xi} - \xi_{n_\zeta} + l_\xi)^2 \\
\rho_F^2 &= (-\zeta' + \zeta_{\mu_\xi} - \zeta_{m_\zeta})^2 + (\xi + \xi_{\nu_\xi} - \xi_{n_\zeta})^2 \\
\rho_G^2 &= (l_\zeta - \zeta' + \zeta_{\mu_\xi} - \zeta_{m_\zeta})^2 + (\xi + \xi_{\nu_\xi} - \xi_{n_\zeta} + l_\xi)^2
\end{aligned} \tag{3.28}$$

3.2 Formation of the Impedance Matrix

As mentioned in the previous section, to solve for a specific microstrip discontinuity, a discretization of the entire (M)MIC surface enclosing the structure (Figure 2.2) is performed. The reason for this approach is two-fold. On one hand, it allows the maximum utilization of symmetry inherently present in the open microstrip problem, as will be discussed shortly. Secondly, when the discretization is performed in this manner, other circuit elements printed on the same substrate may be analyzed without the re-evaluation of the impedance matrix elements. For the desired microstrip element, a simple routine correctly fills the impedance matrix from these pre-existing elements according to the discontinuity shape and the known boundary conditions. Therefore, if a design is to be made on a specific substrate (such as GaAs or Alumina), impedance matrix elements can be pre-computed and stored in libraries, and re-used indefinitely for the synthesis of the desired performance. However, it must be noted that for very large problems, solving the matrix can be more time-consuming than generating the matrix elements, and the savings from this approach may not

be as significant.

The mesh of Figure 2.2 shows a total of $(N_i M_i), (i = x, y)$ node points resulting in $(N_x M_x)^2 + (N_y M_y)^2$ interactions for the direct terms (Z_{xx}, Z_{yy}) and $(N_x M_x N_y M_y)$ interactions for the cross-coupled terms (Z_{yx}, Z_{xy}) . Fortunately, this number can be reduced significantly by symmetry and reciprocity. From equations (2.36)-(2.40) it can be shown that the spatial dependence in the direct terms is an even function of the quantities $(x - x')$ and $(y - y')$. Furthermore, the cross-coupled interactions are odd functions of these quantities. Therefore, elements may be catalogued according to these properties, resulting in large reductions in computational effort. The number of elements computed for the particular submatrix Z_{ij} is reduced to $N_i M_j, (i, j = x, y)$, which is the square root of the previously given numbers. This is not true for shielded microstrip where the position of the cavity or waveguide wall is reflected in the spatial dependence of the Green's function. Consequently, the interactions between subsections are not solely dependent on their relative position to each other, but also on their exact position in the cavity.

A three-dimensional view of the impedance matrix is shown in Figure 3.2. The matrix is toeplitz and diagonally dominant with the value of the diagonal elements the largest contribution by an order of magnitude. The large values of elements off the diagonal results from interactions of adjacent cells, and their location in the impedance matrix depends on the ordering of the nodes.

3.3 Effective Dielectric Constant

Before computing the network parameters for a microstrip discontinuity, it is necessary to determine the value of the guide wavelength on its feeding lines. Fortunately, this parameter is easily obtained without significant additional effort. The

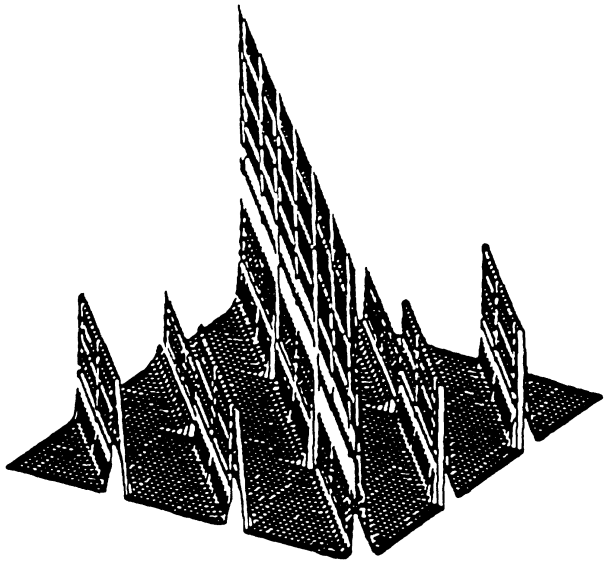

Figure 3.2: Impedance Matrix

guide wavelength (λ_g) and effective dielectric constant (ϵ_{eff}) are related by the expression

$$\lambda_g = \frac{\lambda_0}{\sqrt{\epsilon_{eff}}} \tag{3.29}$$

with λ_0 the free space wavelength. For a particular discontinuity under consideration, the guide wavelength for its feeding lines is determined by simulating a long open-ended line of the same dimensions. The magnitude of the resulting current is of the form shown in figure 3.3. It is then an easy matter to determine the guide wavelength by either of the expressions

$$\lambda_g = 2\frac{(d^{Imax}_{max} - d^{1}_{max})}{(I_{max} - 1)} \tag{3.30}$$

or

$$\lambda_g = 2\frac{(d^{Imin}_{min} - d^{1}_{min})}{(I_{min} - 1)} \tag{3.31}$$

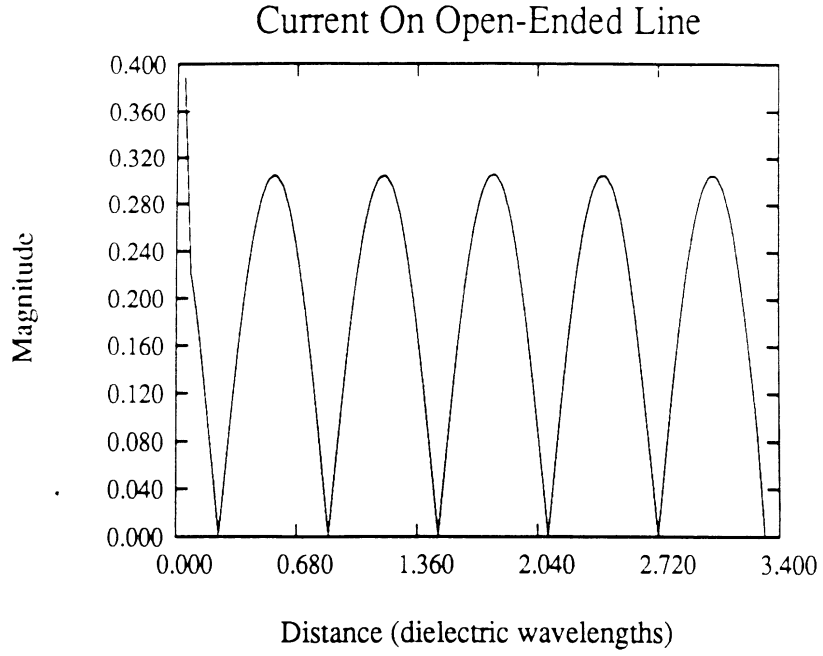

Figure 3.3: Longitudinal current distribution for a long open-ended line ($h = 25mil, W = 25mil, \epsilon_{r1} = 10.65$)

where $d_{max}(d_{min})$ are the positions of maxima (minima) on the line and $I_{max}(I_{min})$ is the number of maxima (minima). The accuracy of λ_g is improved by increasing the line length and therefore the number of maxima and minima. The effective dielectric constant is then given by

$$\epsilon_{eff} = (\frac{\lambda_0}{\lambda_g})^2 = (\frac{c}{2f})^2(\frac{I^{max} - 1}{d^{Imax}_{max} - d^{1}_{max}})^2 \quad . \tag{3.32}$$

Figure 3.4 shows the effective dielectric constant for a 50 ohm line with increasing line length. As illustrated, an accurate value is obtained for short lengths of line with only two maxima or minima present. Also note that the subsection size influences the stability of the effective dielectric constant. For the same physical discretization, the data at 12 GHz stabilizes at shorter line lengths than the results for 18 GHz. The electrical size of the subsection is larger at the higher frequency, with the values given

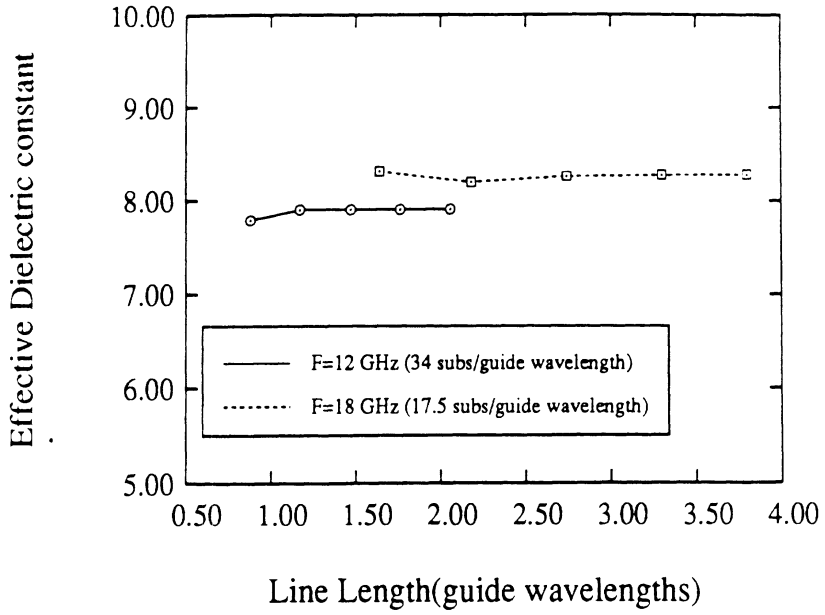

Figure 3.4: Effective Dielectric Constant For single layer substrate ($h = 25mil, W = 25mil, \epsilon_{r1} = 10.65$) with increasing length of line

in the graph. Furthermore, the greater radiation losses at higher frequencies distorts the shape of the current, and it has been found that the average of several maxima or minima is required for accurate results. Convergence tests for the subsection size will be discussed more extensively in section 3.4.2, and radiation loss in Chapter 5.

It is critical to obtain accurate values of the effective dielectric, because poor accuracy for the effective dielectric constant will result in less accurate and unstable network parameter results. In Figure 3.5, the effective dielectric constant of a fifty ohm line is compared to CAD results [56] for a shielded structure. The agreement is excellent, as expected, because the fundamental open microstrip mode does not radiate.

For multi-layer microstrip, there is far less available data than for single layer.

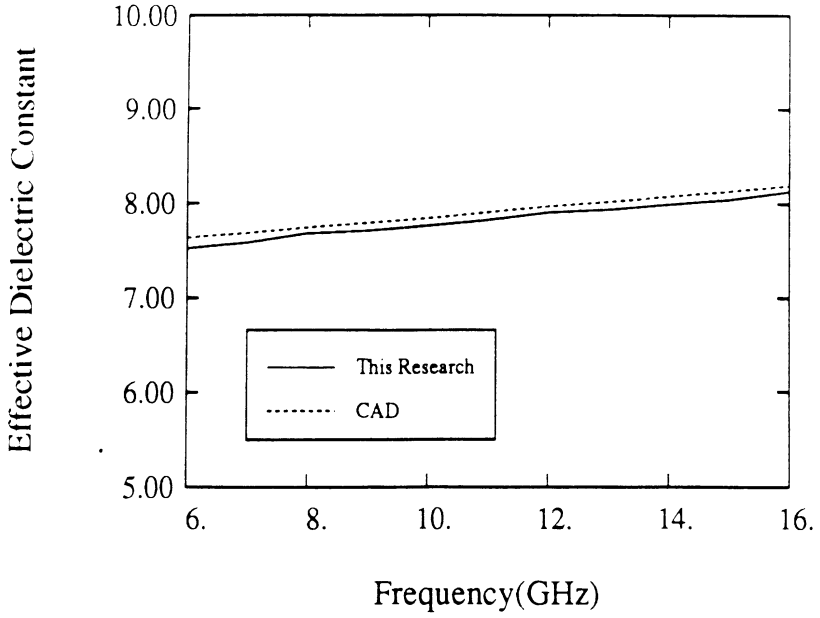

Figure 3.5: Effective Dielectric Constant For single layer substrate ($h = 25mil, W = 25mil, \epsilon_{r1} = 10.65$)

Consequently, it is important to obtain the effective dielectric constant from the full-wave simulation. In Figure 3.6, the fullwave results for a two layer structure are compared to a 2-dimensional simulation [55] with good agreement. Two-dimensional simulations are specifically formulated to determine propagation characteristics and are considered very accurate. Nevertheless, these results show that a three-dimensional simulation yields accurate values, which are more than adequate. The effect of the inclusion of a superstrate layer is shown in Figure 3.7, where a low dielectric material ($\epsilon_r = 2$) is covered by a thinner high dielectric constant ($\epsilon_r = 13$) material. The superstrate layer, which is often included for protection, increases the effective dielectric constant and line dispersion considerably.

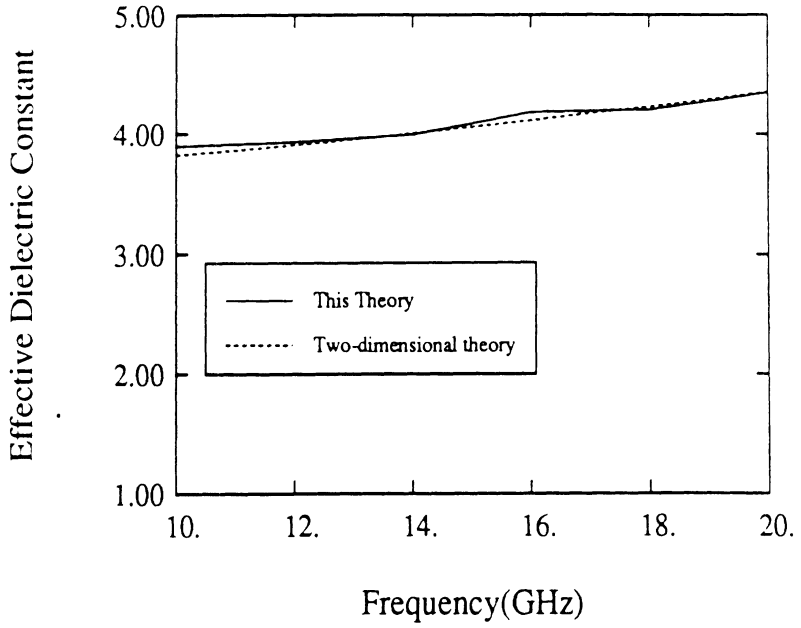

Figure 3.6: Effective Dielectric Constant For a two-layer substrate ($h_1 = 16mil, h_2 = 40mil, \epsilon_{r1} = 13, \epsilon_{r2} = 2$)

3.4 Convergence of Network Parameters

3.4.1 Convergence of network parameters for the choice of A

The choice of the parameter A in equation (3.1), influences both the accuracy and numerical convergence of the network parameters. The CPU time increase linearly with A for the calculation of $Z^A_{\xi\zeta}$, while it is independent of A in the computation of $Z^\infty_{\xi\zeta}$. Furthermore, the computer time for the computation of $Z^A_{\xi\zeta}$ is significantly greater than the time required for $Z^\infty_{\xi\zeta}$. Therefore, the value of A must be chosen as small as possible, while still achieving numerical convergence. Figures 3.8 and 3.9 show the convergence of the phase of S_{12} and the radiated power as a function of A. Table 3.4.1 shows the correspondence between the quantity A_t defined in equation (3.1), and the parameter shown in the graph. As shown, the network parameters

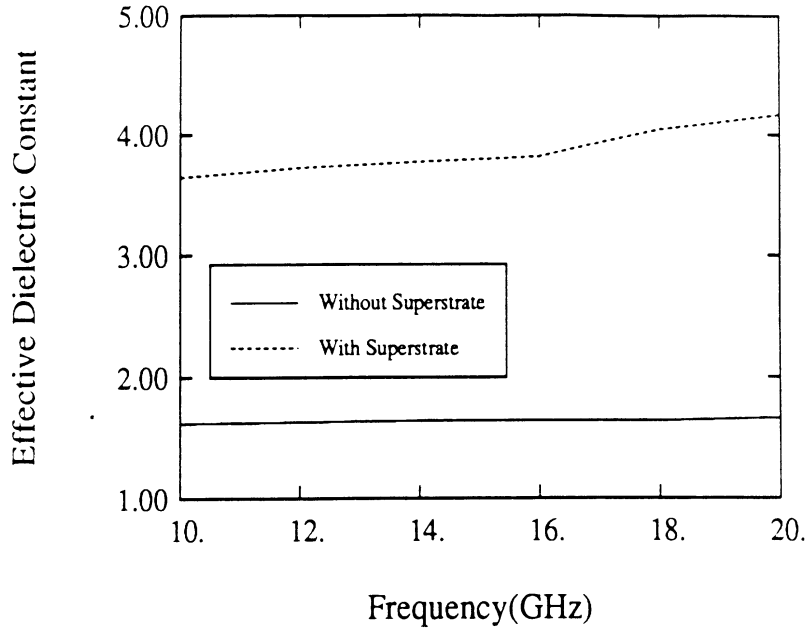

Figure 3.7: Effective Dielectric Constant for microstrip line with a superstrate ($h_1 = 16mil, h_2 = 40mil, \epsilon_{r1} = 13, \epsilon_{r2} = 2$) and without a superstrate($h_1 = 40mil, \epsilon_{r1} = 2$)

show no sensitivity to increasing A_t above .95. Below $A_t = .9$, the accuracy of the phase of S_{12} and the radiation loss gradually deteriorate until the estimated values become completely unacceptable at $A_t = .7$.

3.4.2 Convergence of network parameters with the choice of subsection size

In this method of moments characterization of microstrip discontinuities, the spacing of the nodes (number of subsections) in the mesh has a large influence on the CPU time. A larger subsection size results in faster execution times, but may result in inaccurate results. Obviously, the choice of this parameter must be made by seeking a balance between acceptable numerical error and computational effort.

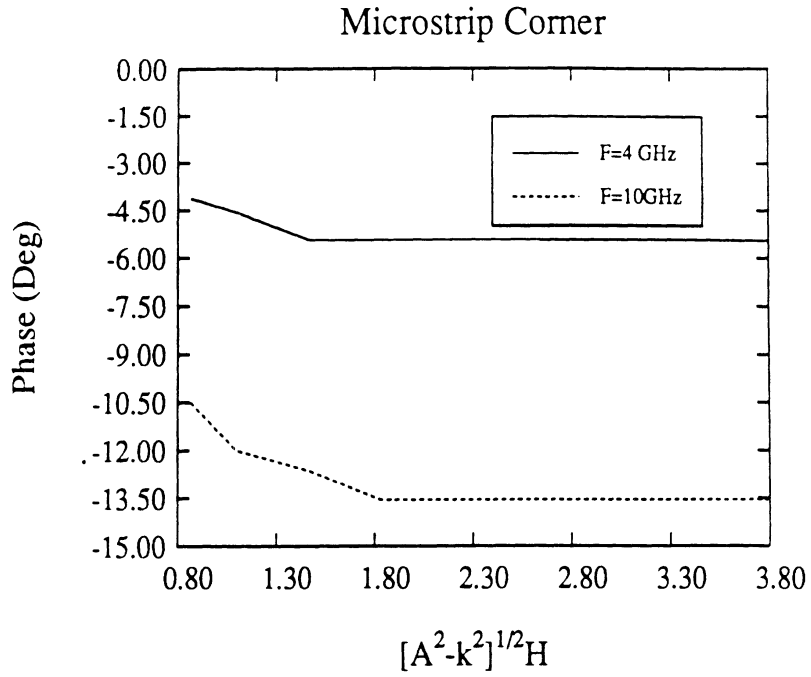

Figure 3.8: Convergence of the Phase of S_{12} as a function of the parameter A for a microstrip corner discontinuity ($w = 56mil, h_1 = 56mil, \epsilon_{r1} = 2$)

Fortunately, convergence has been achieved for a wide range of the subsection size. These results may be used to determine the optimum choice of the subsection size for a desired degree of accuracy.

Open-End

A convergence experiment was performed on a fifty ohm open-ended microstrip line printed on a 25 mil substrate ($\epsilon_r = 10.65$). Results at 10 GHz for the magnitude and phase of S_{11} were obtained for varying longitudinal discretizations. The transverse discretization remains constant and is equal to half the lines width. In Figure 3.10, the magnitude of S_{11} has converged within one percent for cases greater than 30 subsections/wavelength. Results obtained with a division of 20 subsections/wavelength show an error of almost two percent, and 10 subsections/wavelength

shows an error of 3.5 percent. Note that results from sparser discretizations indicate higher radiation loss than is actually occuring.

Figure 3.11 displays the convergence of the phase at the open end, which displays a similar behavior to the magnitude. The phase settles down within about 1 degree above 30 subsections/wavelength.

Two-port Rectangular Stub

Figures 3.12 and 3.13 show the convergence of [S]-parameters for a two-port rectangular stub printed on the same substrate as above. The phase and magnitude are very stable for discretizations of 30 subsections/wavelength or more. As was the case in the example above, discretizations below 30 subsections/wavelength yield results which show higher radiation losses than are actually occuring.

These examples indicate that discretizations of 30 subsections/wavelength will yield good results. Higher discretizations can be performed if accuracies smaller than one percent for the magnitude and one degree for the phase are desired. For the typical 2-port problem presented in this thesis, discretizations of up to 100 subsections/wavelength can be handled on desktop workstations.

Table 3.1: Choice of A for microstrip Corner Discontinuity of Figs. 3.8 and 3.9

$\frac{A}{\lambda_0}$ (10 GHz)	$\sqrt{A^2 - k^2} \cdot H$	$A_t = \tanh(\sqrt{A^2 - k^2} \cdot H)$
20	0.867	.7
24.8	1.098	.8
32.3	1.472	.9
39.6	1.832	.95
56.5	2.647	.99
80.6	3.800	.999

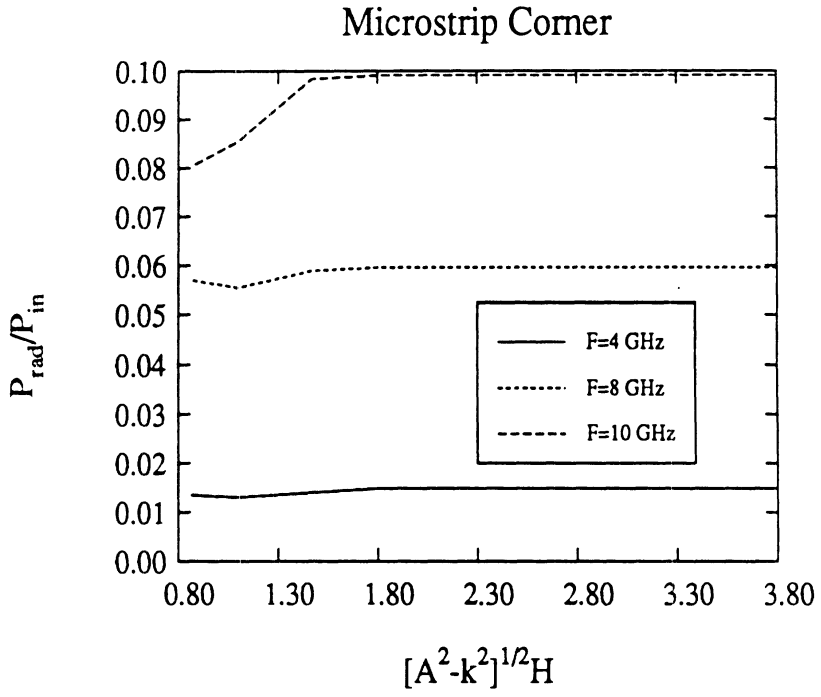

Figure 3.9: Convergence of the radiation loss as a function of the parameter A for a microstrip corner discontinuity ($w = 56mil, h_1 = 56mil, \epsilon_{r1} = 2$)

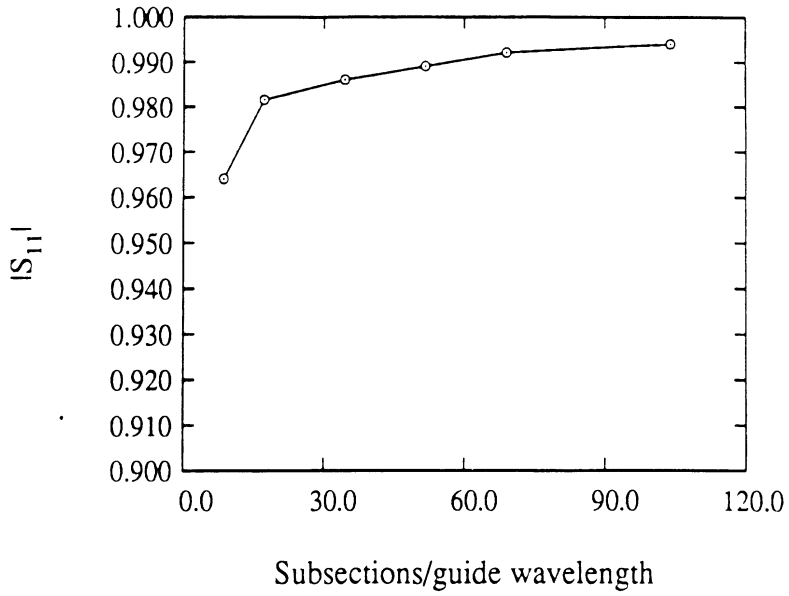

Figure 3.10: Convergence of the $|S_{11}|$ as a function of the longitudinal subsection size for a microstrip open end ($w = 25mil, h_1 = 25mil, \epsilon_{r1} = 10.65$)

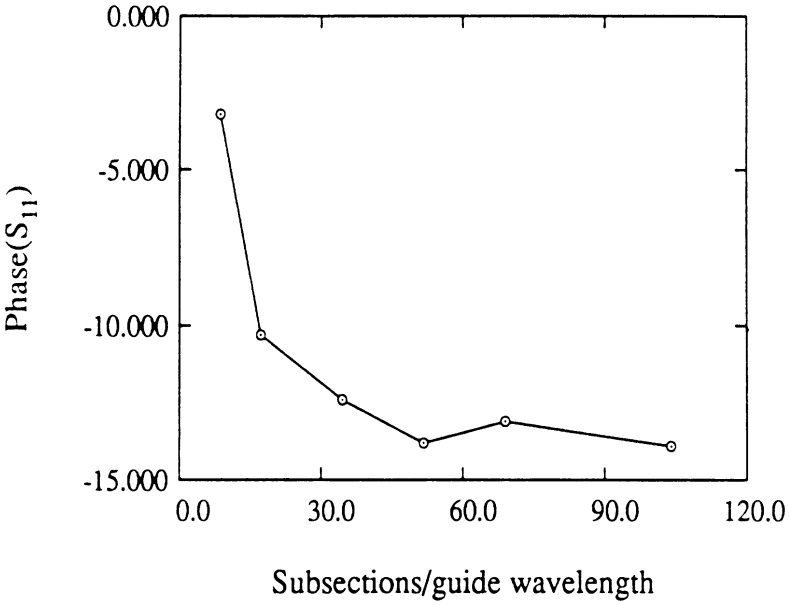

Figure 3.11: Convergence of the phase of S_{11} as a function of the longitudinal subsection size for a microstrip open end ($w = 25mil, h_1 = 25mil, \epsilon_{r1} = 10.65$)

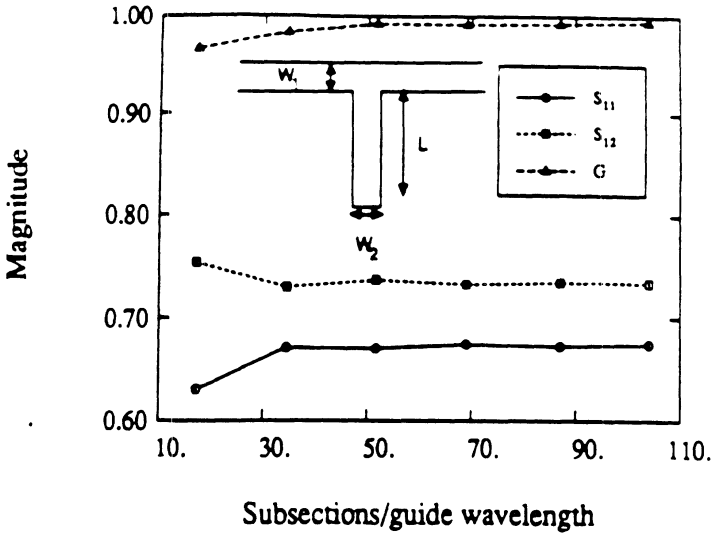

Figure 3.12: Convergence of S-parameter magnitudes as a function of the subsection size for a microstrip 2-port stub ($W1 = W2 = 25mil, h_1 = 25mil, \epsilon_{r1} = 10.65$)

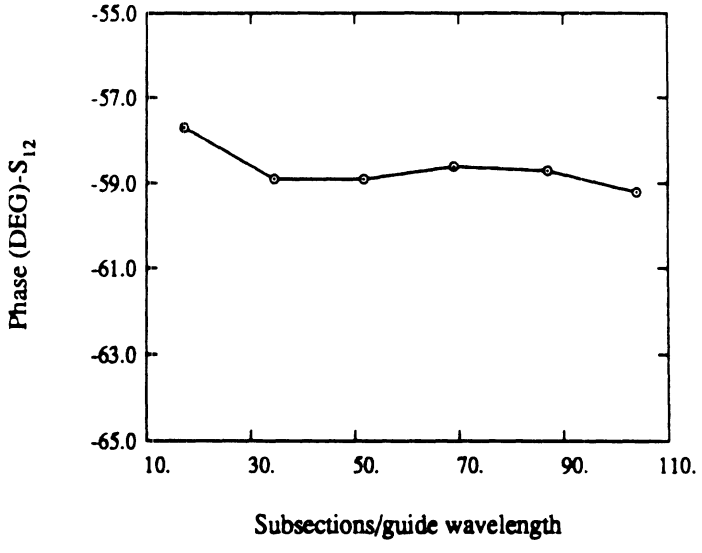

Figure 3.13: Convergence of the phase of S_{12} as a function of the subsection size for a microstrip 2-port stub ($W1 = W2 = 25mil, h_1 = 25mil, \epsilon_{r1} = 10.65$)

CHAPTER IV

RESULTS-CIRCUIT CHARACTERIZATION

4.1 Introduction

This chapter presents the results from an extensive study of microstrip structures, acquired with the theoretical and numerical techniques described in Chapters 2 and 3. In addition, results from the experimental study are presented . Although the literature provided experimental data for many microstrip discontinuities, an experimental study was undertaken to verify the "step" approximation used to analyze structures with curved boundaries, such as the radial stub, by a rectangular mesh. A TRL de-embedding method was used to obtain this data, and it is detailed in section 4.2. In addition, the repeatabilty of these measurements was investigated and results are presented.

The theoretical examples are arranged in order of increasing complexity. In sections 4.3, examples of step and two-port shunt stub discontinuities will be shown. For these examples, the accuracy of the fullwave technique will be demonstrated by comparisons to experimental data. In addition, a high frequency matching circuit containing two stub tuners will be presented to illustrate the performance limitations of microstrip circuitry at submillimeter-wave frequencies.

Microstrip meander lines are utilized for a variety of millimeter wave IC and

array applications including phase shifting and filtering. In section 4.3.4, examples of meander lines appropriate for phase shifting and/or filter applications will be presented. The effect of electromagnetic coupling, conductor loss, and radiation loss will be discussed for these lines.

It is well known that mitered bends and radial stubs exhibit improved performance over their right-angle and rectangular counterparts. Consequently, the application of the fullwave technique has been extended to structures having boundaries which are not rectilinear in section 4.3.5. In order to model these structures with a rectangular mesh, the curved boundaries must be approximated with a "step" approximation. The accuracy of this approximation has been verified experimentally, and examples of radial stubs and mitered bends are given.

Results for multi-port networks are shown in section 4.4. In particular, the network parameters for T- and cross junctions will be presented. These structures are frequently used in large numbers in array feeding structures, and therefore, accurate models are needed for their high frequency behavior.

Finally, fullwave analysis results for microstrip circuits printed on multi-layer dielectric substrates are given in section 4.4. The effects of these more complicated substrate structures on radiation loss will be discussed.

4.2 Experimental Results

TRL fixture de-embedding may be implemented in either one or two tiers. The two-tier approach requires that a standard 7 mm coaxial calibration be done for ANA error correction. The TRL calibration is then performed to move the reference plane within the test fixture. The [S]-parameters of the two fixture halves are determined in the process. The two-tier approach requires a computer and corresponding

software for data acquisition and processing. The one-tier approach does not require a 7 mm calibration and is therefore simpler and less time consuming, but does not yield the [S]-parameters for the fixture halves as in the case of two-tier. The computer is not required for data acquisition because test data may be obtained without additional processing on the ANA display in real time. With the availability of the HP 8510B and the TRL calibration kit [60], one tier de-embedding was selected for these experiments.

Fixture and Standard Design

As mentioned, network analyzer measurements of microstrip structures requires coaxial-to-microstrip transitions. This is usually accomplished by the use of a fixture, although wafer probe stations are also used. Probe station measurements would require coplanar waveguide to microstrip transitions, but the TRL de-embedding approach is still applicable. The fixture employed for these measurements is shown in figure 4.1. In this implementation, standards and devices are mounted to brass chip holders which fit into the fixture as shown in the figure. The fixture includes Eisenhart [59] coaxial-to-microstrip transitions which have shown good repeatability up to 20 GHz [57]. The TRL de-embedding procedure requires a thru-line, delay lines, and an open-ended line as shown in Figure 4.2 (a) and (b). This implementation uses two delay lines in order to cover the entire 2-16 GHz band. The reference plane is set at the center of the thru line. The standards and Devices Under Test (DUTs) were realized on 25 mil RT duroid dk-10($\epsilon_r = 10.25 \pm .25$). The DUTs, shown in figure 4.3(a),(b), and (c) are one-port radial, and two port rectangular and radial stubs. The reference planes, set by the thru line, are marked on the schematics as a-a and b-b.

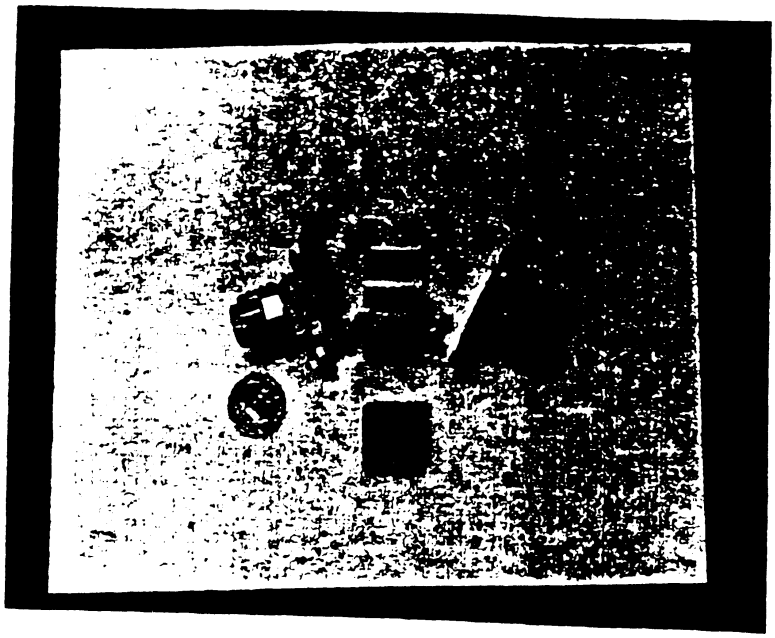

Figure 4.1: Microstrip Test Fixture with Eisenhart Launchers

Effective Dielectric Constant

As mentioned, the TRL de-embedding procedure does not require precise phase constant information at the onset. The phase constant is determined during the calibration procedure, and can be obtained from the de-embedded results. After calibration, the long delay line is re-inserted and measured. The phase of S_{12} is shown in Figure 4.4. The guide wavelength (λ_g) is related to the phase delay (ϕ_d) by the equation

$$\phi_d = -\beta_g l_g = \frac{2\pi l_g}{\lambda_g} \tag{4.1}$$

The effective dielectric constant is defined as

$$\epsilon_{eff} = (\frac{\lambda_0}{\lambda_g})^2 \tag{4.2}$$

and is plotted in Figure 4.5. Also plotted are the theoretical effective dielectric constants for various substrate permittivities. The dielectric constant of the substrate is found to be $10.6 \pm .1$.

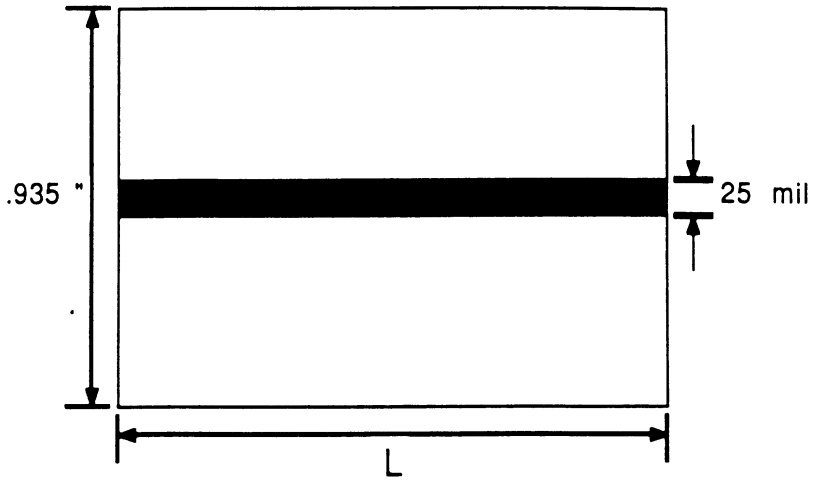

a. Thru/Delay Lines

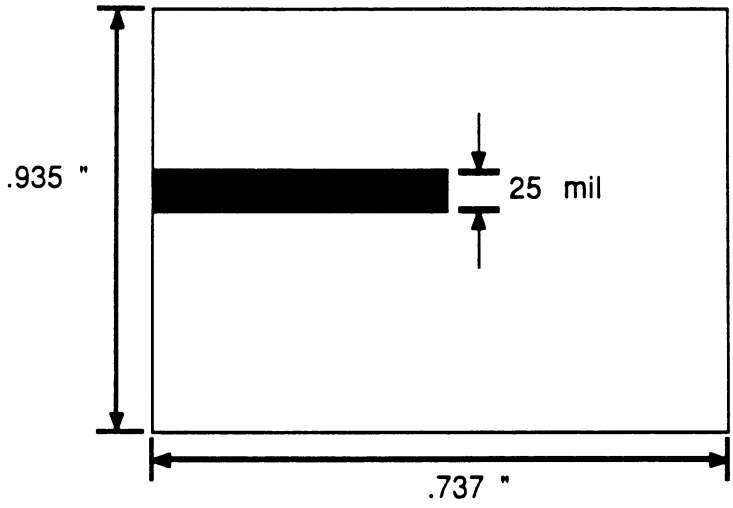

b. Open-ended Line

Figure 4.2: Standards for Microstrip De-embedding (L=.737" for thru line,L=1.014" and .835" for delay lines)

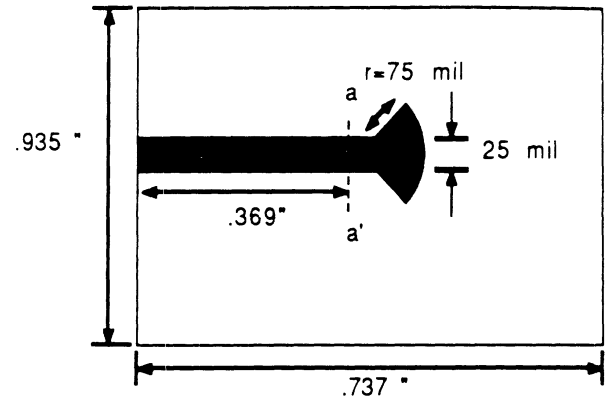

a. One-port Radial Stub

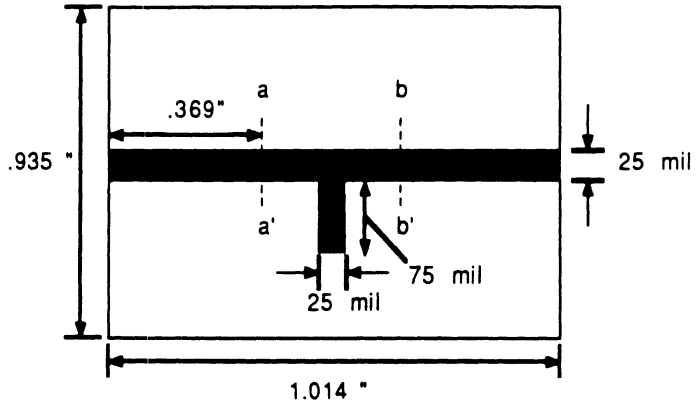

b. Two-port shunt Rectangular Stub

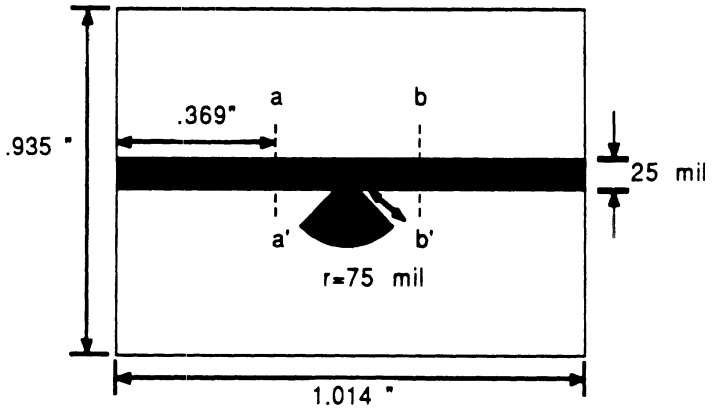

c. Two-port shunt Radial Stub

Figure 4.3: Microstrip Test Structures

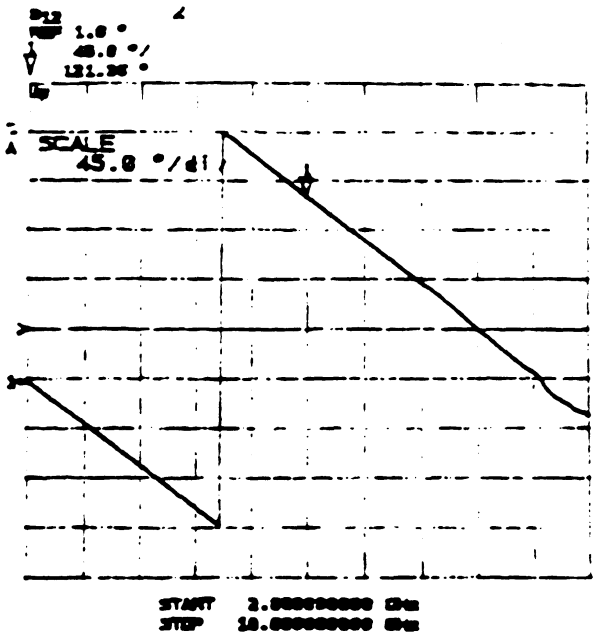

Figure 4.4: Phase of Long Delay Line After TRL Calibration

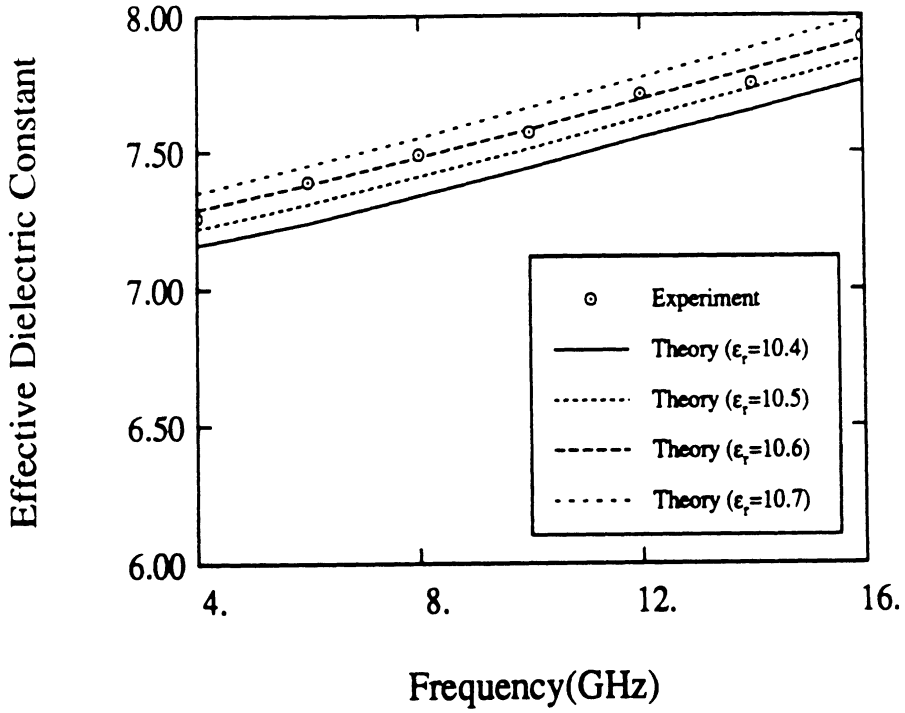

Figure 4.5: Experimental Effective Dielectric Constant

Repeatability

The TRL De-embedding technique requires that the coaxial-to-microstrip transitions be repeatable. Between measurements, the launcher transition is broken, the standard or test structure is removed, and a new one is inserted. The launcher transition is then re-established. This process is entitled cycling. To improve repeatability, all standards and test devices are etched from the same piece of material in the same process. Also, launcher and the microstrip line contacting the launcher are kept scrupulously clean. The specific fixture used has previously been shown to produce reasonably repeatable results to 20 GHz for shielded structures [58]. Two studies were performed to determine the repeatability of the open results. In the first study, a TRL calibration was performed and the rectangular stub was measured. The connections were broken to the stub device, re-established and the measurement was performed again. This procedure was done 10 times. Results are shown in Tables 4.1 and 4.2 for the phase and magnitude of S_{12}, respectively. The minimum, maximum, average, and standard deviation are shown for frequencies from 4 to 16 GHz. It can be seen that the cycling introduced phase errors less than 1 degree at lower frequency ranges. The error increases with frequency and reaches almost 4 degrees at 16 GHz. The magnitude showed good repeatability ranging from .0037 at the low end to .027 at the high end. The second study involved repeating the entire TRL calibration and measuring the radial stub 10 times. In this manner all connections for the standards and stub are cycled. Results are shown in Tables 4.3 and 4.4. The errors introduced in this repeatability study are slightly larger on average than the previous study. Nevertheless, both tests indicate that the fixture yields results which are reasonably repeatable in the frequency range it is employed.

The error bars that are present on the following graphs were determined by

Table 4.1: Repeatability for phase(Deg) of S_{12} for rectangular stub (10 trials)

f(GHz)	Min. Value	Max. Value	Avg.	Stnd. dev.
4	-103.9	-102.0	-102.9	.631
6	-154.4	-153.4	-154.0	.540
8	143.8	147.3	145.5	1.11
10	87.2	90.8	89.3	1.17
12	16.0	24.2	24.2	2.51
14	93.4	101.8	98.1	2.54
16	17.7	29.6	23.3	3.98

Table 4.2: Repeatability for magnitude of S_{12} for rectangular stub (10 trials)

f(GHz)	Min. Value	Max. Value	Avg.	Stnd. dev.
2	.989	1.01	.995	.0037
3.4	.971	.993	.985	.0063
4.8	.95	.979	.968	.011
6.2	.925	.971	.957	.019
7.6	.864	.9	.888	.015
9	.800	.832	.815	.011
10.4	.729	.803	.778	.023
11.8	.475	.505	.497	.010
13.2	.079	.117	.112	.012
14.6	.300	.336	.322	.012
16	.635	.714	.682	.027

Table 4.3: Repeatability for phase(Deg) of S_{12} for radial stub (10 trials)

f(GHz)	Min. Value	Max. Value	Avg.	Stnd. dev.
2	-56.3	-55.8	-56.0	.205
4	-116.9	-115.5	-116.1	.441
6	-172.3	-168.2	-169.9	1.34
8	121.9	126.6	124.9	1.54
10	68.6	74.7	71.6	1.70
12	1.9	7.4	5.3	2.08
14	98.3	106.3	101.0	2.85
16	7.7	13.0	10.35	2.07

Table 4.4: Repeatability for magnitude of S_{12} for radial stub (10 trials)

f(GHz)	Min. Value	Max. Value	Avg.	Stnd. dev.
2	.960	.972	.966	.00039
3.4	.915	.953	.935	.012
4.8	.818	.850	.835	.011
6.2	.708	.761	.738	.018
7.6	.623	.671	.653	.018
9	.471	.503	.491	.014
10.4	.368	.400	.382	.014
11.8	.130	.154	.151	.011
13.2	.130	.154	.143	.0092
14.6	.397	.429	.410	.011
16	.616	.714	.681	.038

adding the above standard deviation to the uncertainty introduced by variations in the dielectric constant ($\pm.1$), the substrate height ($\pm$1mil), and the conductor width ($\pm$1 mil).

4.3 Single Layer Microstrip Discontinuities and Circuits

4.3.1 Step Discontinuity

The discontinuity shown in figure 4.6 has been characterized by the preceeding fullwave analysis. This matching section is printed on a 10 mil alumina substrate ($\epsilon_r = 9.8$), and is characterized from 8-18 GHz. Radiation loss was found to be insignificant for this example, because the substrate thickness remains electrically small ($< \frac{1}{10}\lambda_g$) over this frequency range. Figures 4.6(a) and 4.6(b) show the magnitude and phase of the scattering parameters as compared to measurement. The agreement with measurements for magnitude and phase is excellent. In particular, the agreement of the phase is within 2 degrees across the entire frequency range.

4.3.2 Tuning Stubs

Two numerical examples of rectangular stubs, which are frequently used in filter and matching circuit applications, are presented in this section. Both examples show excellent agreement with measurement. In Figure 4.7 a two-port shunt stub is compared with measurements obtained by the TRL de-embedding technique of section 4.2. The stub was printed on a 25 mil duroid substrate ($\epsilon_r = 10.65$), and includes two type of discontinuities, a T-junction and open-end. Agreement between theory and experiment for both the phase and magnitude is excellent. In particular, note the close agreement in the resonant frequency at 13.5 GHz, indicated by the minimum in $|S_{12}|$ and the discontinuous increase in the phase.

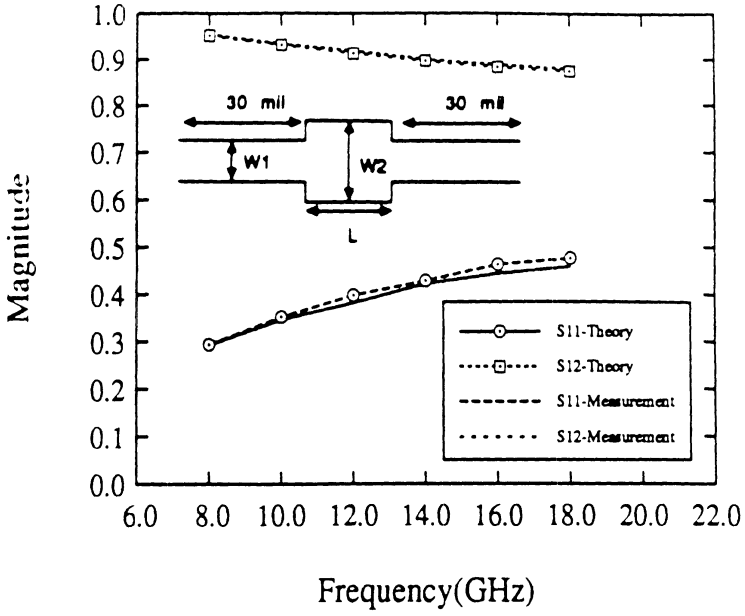

a. Magnitude

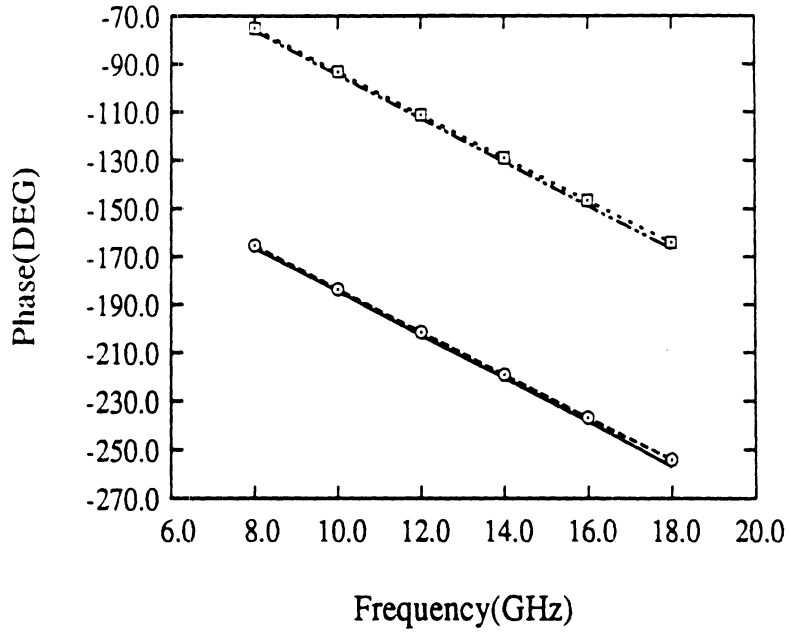

b. Phase

Figure 4.6: Scattering Parameters of Matching Section, numerical(experimental) dimensions: W1=9.2(9.2) mm, W2=23(23.1)mm, L=50.6(50.0), ϵ_r=9.8, h=10 mil

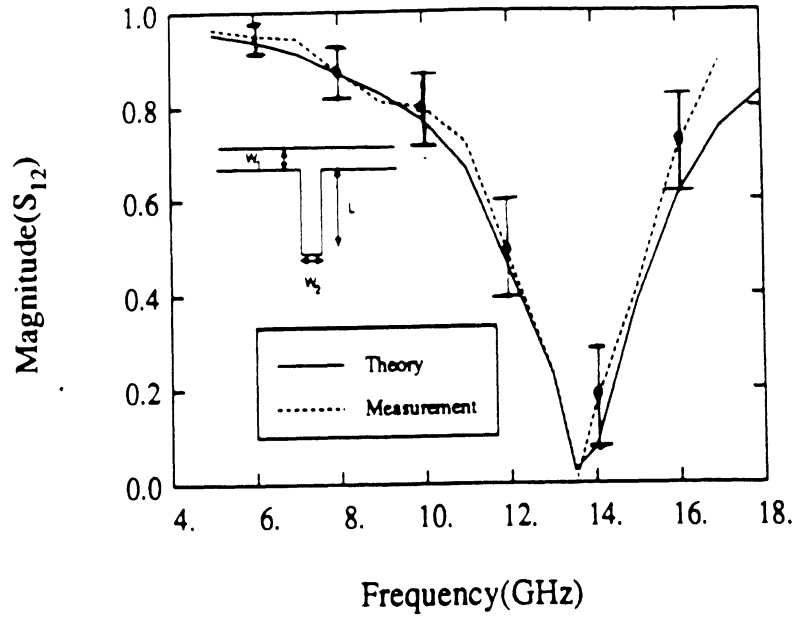

a. Magnitude

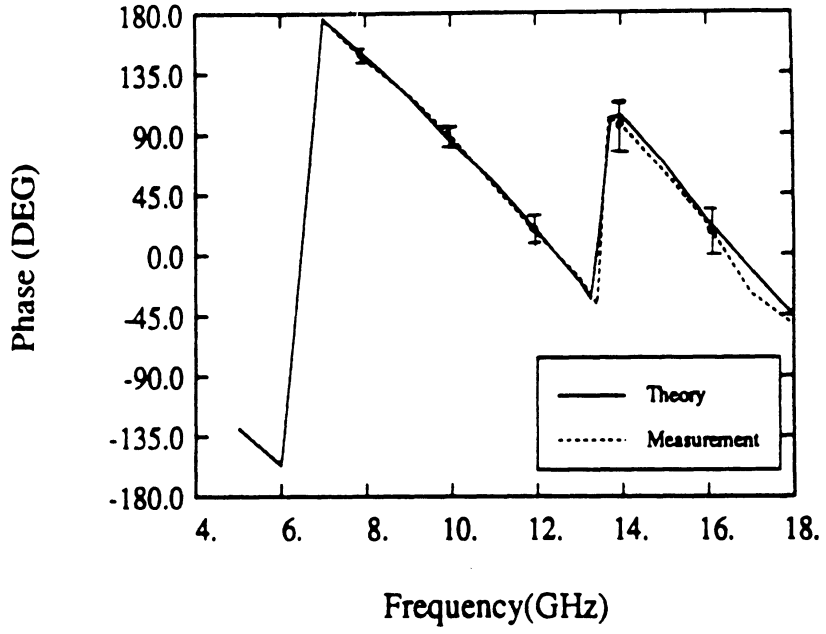

b. Phase

Figure 4.7: Scattering Parameters of Microstrip stub, theoretical(experimental) dimensions: W1=25 mil, W2=25mil, L=75 mil, ϵ_r=10.65, h=25 mil

A second microstrip stub printed on a 1.27 mm duroid substrate ($\epsilon_r = 10.65$) is shown in Figure 4.8 . In this example, radiation loss is more significant because of the thicker substrate. A major contribution of this research is the characterization of space and surface wave losses. The results are compared to published data obtained with the spectral domain technique[25]. As illustrated in the figure, the agreement between our space domain technique and the spectral domain technique is very good. Note the good agreement at the resonant frequency. The quantity denoted G in the graph corresponds to $|S_{11}|^2 + |S_{12}|^2$, which may be subtracted from 1 to determine the total radiated power. From this quantity it is seen that the radiation loss peaks at 10.5 GHz which is slightly beyond the stub resonance (10.2 GHz).

4.3.3 Matching Circuit for 94 GHz Oscillator

Figure 4.9 shows a matching circuit for a submillimeter-wave oscillator designed to operate at 94 GHz. The network is printed on 100 μm GaAs ($\epsilon_r = 12.8$). The analysis was applied to obtain scattering parameters individually for the cross junction stub (stub A), the T-junction stub (stub B), and the entire matching section. The results for this example are normalized to fifty ohms. Emphasis will be put on the radiation losses experienced as the stubs pass through a quarter wave resonance, and the coupling between the stubs. Frequently, such a design would be done with available CAD by individually modeling the two stubs, and combining the results with linear network theory. Consequently, electromagnetic interactions between the stubs would not be included. For this case, electromagnetic effects will be significant, because the stubs are in close proximity and have approximately the same resonant frequency.

Shown in Figures 4.10(a) and (b) are the scattering parameters for the cross junction and the T-junction stub, respectively. The quarter wave resonance of the

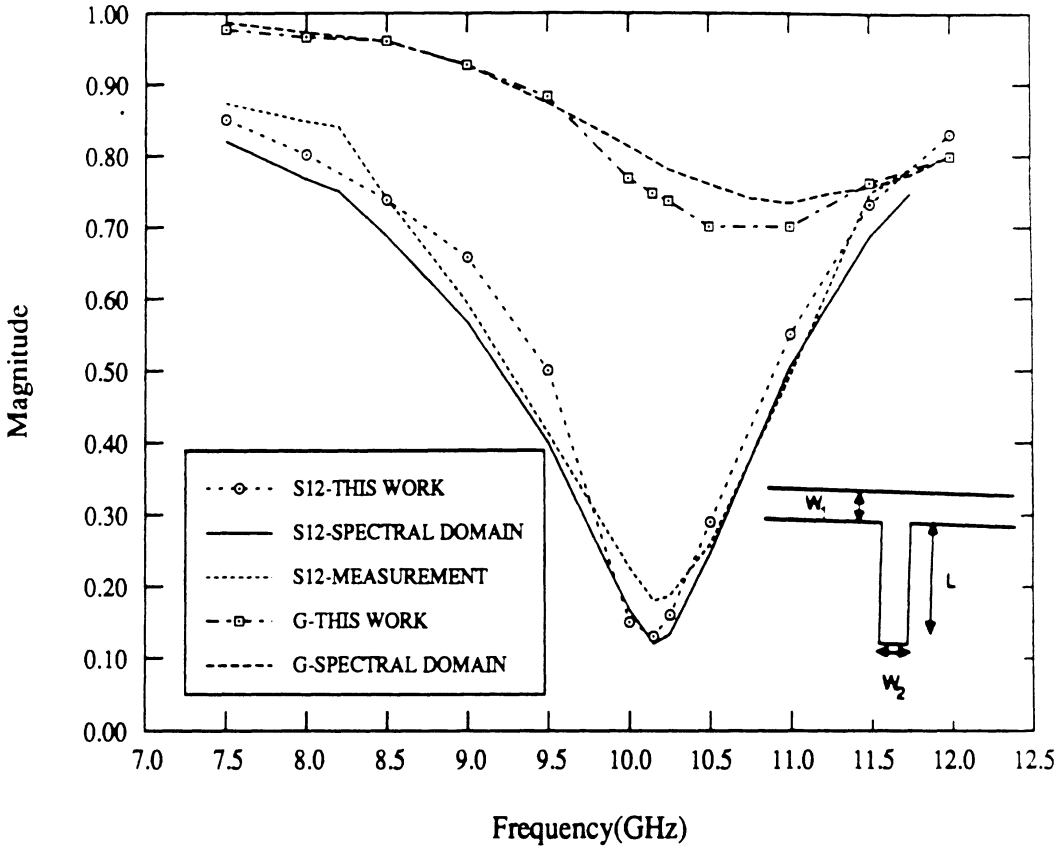

Figure 4.8: Scattering Parameters for Microstrip Stub, space(spectral) dimensions: W1=1.44(1.40), W2=1.44(1.40), L=2.16(2.16), ϵ_r=10.65, h=1.27 mm

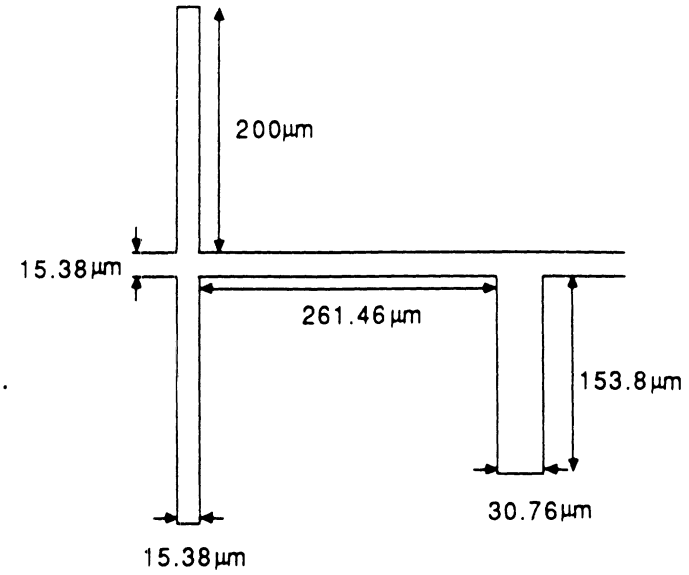

Figure 4.9: Microstrip Oscillator matching network ($\epsilon_r = 12.8, h = 100\mu m, W = 15.38\mu m$)

stubs are 145 GHz for stub A and 160 GHz for stub B as determined by the minima in the magnitude of S_{12}. There is appreciable radiation loss beyond the resonances of the two stubs. This radiation causes a degradation in the magnitude of S_{11} at the high frequency end of the simulations for both stubs. The cross-junction stub radiates less than the T-junction stub because of its balanced resonator geometry which results in a cancellation of radiated fields. As shown in Figure 4.12, the T-junction stub is radiating almost half of its input power at 200 GHz.

The scattering parameters for the entire matching network are shown in Figure 4.11. At the lower frequency range (below 140 GHz), the radiation losses are not significant. Thus, the network should function adequately at the oscillation frequency. In this example, although the $100\mu m$ substrate is physically thin for present technology, it becomes electrically thick at higher frequencies (one-fifth of a wavelength

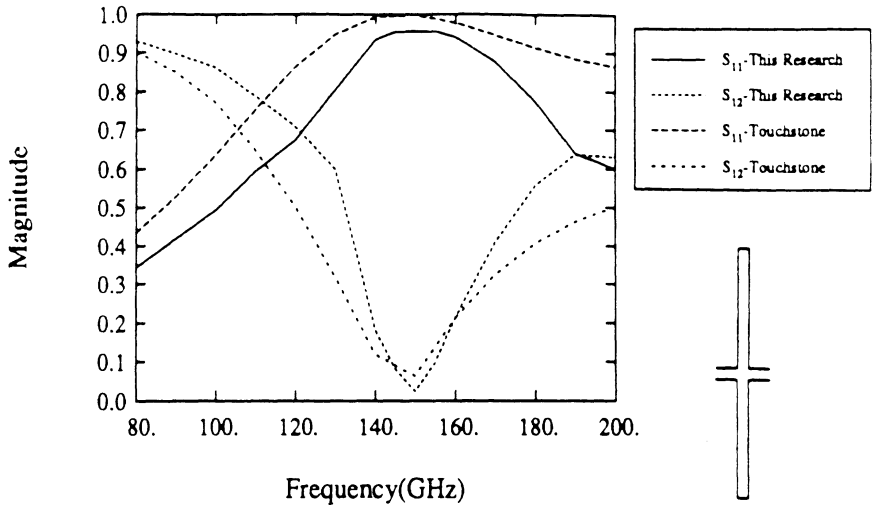

a. Scattering parameters of stub A

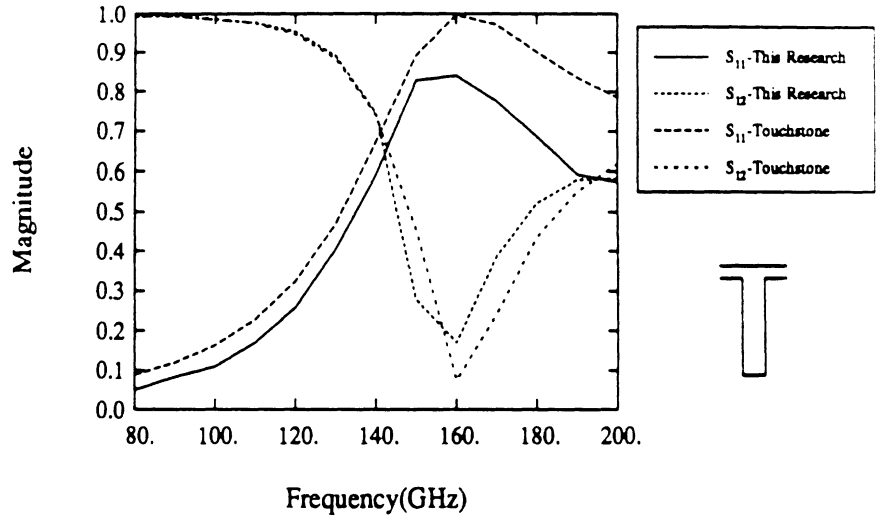

b. Scattering parameters of stub B

Figure 4.10: Scattering parameters of individual stubs found in oscillator matching circuit ($\epsilon_r = 12.8, h = 100\mu m, W = 15.38\mu m$)

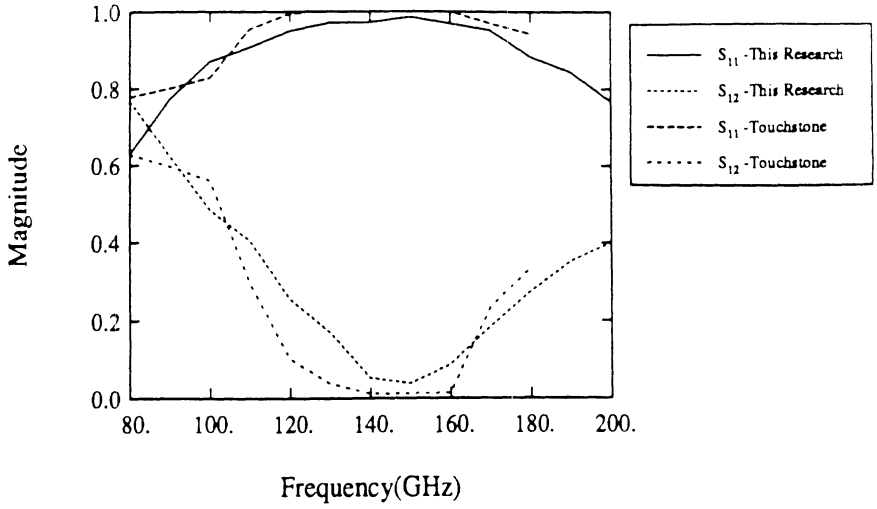

Figure 4.11: Scattering parameters of microstrip matching network ($\epsilon_r = 12.8, h = 100\mu m, W = 15.38\mu m$)

in the dielectric at 170 GHz), and high radiation losses are encountered, as shown in Figure 4.12. This result illustrates the difficulty with using microstrip circuits at submillimeter-wave frequencies.

The entire matching network radiates less than Stub B alone. At first glance this appears anomalous, but it results from an increased return loss and additional phase cancellation in the radiated fields. The spacing of the stubs is approximately one half wavelength at the upper frequencies, therefore, they are radiating fields which are approximately 180 degrees out of phase. Also note in this example that radiation loss continues to increase beyond the quarter wave resonance of the stubs.

4.3.4 Meander Lines

Meander lines are often used in (M)MICS as delay or slow wave lines, and also in monolithic antenna arrays for the phasing of the radiating elements as illustrated

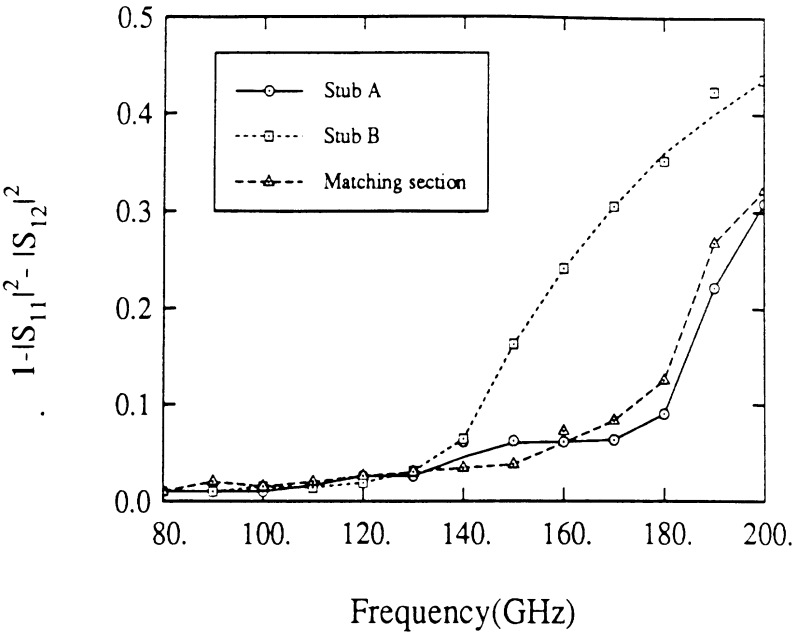

Figure 4.12: Radiation loss in microstrip matching network ($\epsilon_r = 12.8, h = 100\mu m, W = 15.38\mu m$)

in Figure 4.13. In this application, a two layer structure is shown with an embedded meander line feeding the antenna elements on the top of the substrate. Such a feed structure is also capable of exciting a slot array. The ability to adjust the spacing (S), the depth (d), the period length (L_p), and the number of periods (N) provides flexibility in the phasing of the radiating elements. Therefore, meander lines are particularly suited for use in beam forming and steering[61].

Meander lines traveling wave feed with conductor loss

Successful design of such structures requires accurate models, which include the presence of bend discontinuities and the effect of electromagnetic coupling. Radiation and conductor loss may also have significant effects. Figure 4.14 presents the transmission parameter as a function of line length for a meander line printed on a

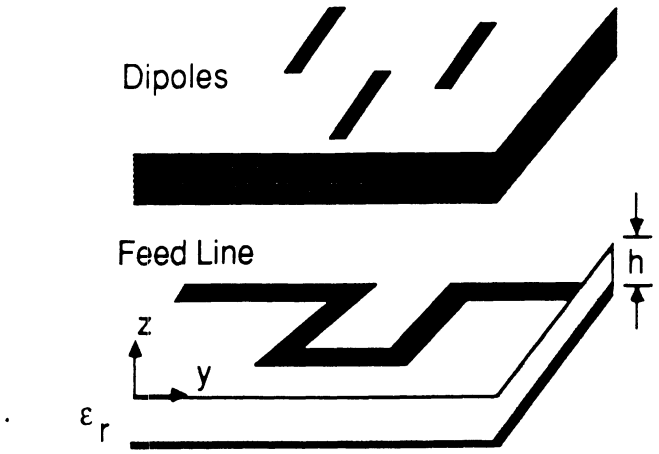

a. Cross-Sectional View

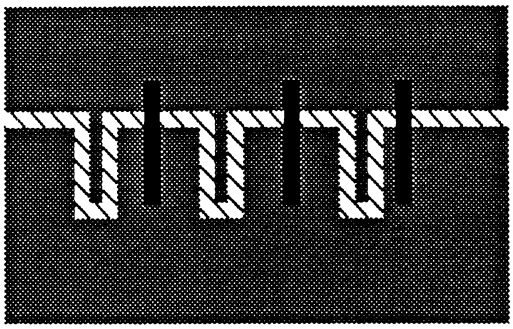

b. Top View

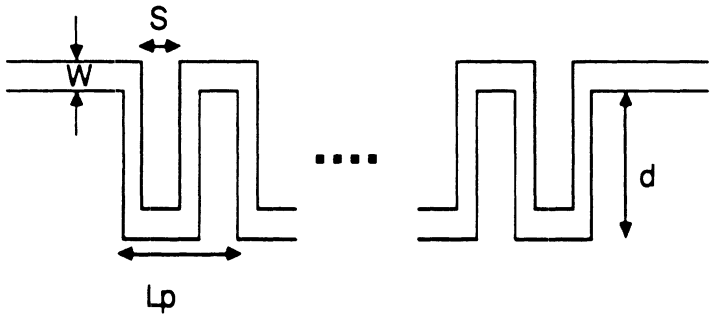

c. Meander Line Parameters

Figure 4.13: Microstrip Meander Line Feeding Dipoles

20 mil duroid substrate ($\epsilon_r = 2.2$) at 20 GHz. Two cases are shown: 1) with both resistive and radiation loss, and 2) radiation loss only. In this example, the substrate is electrically thin and radiation loss is not large. Conductor loss is essentially the difference between the two curves, and increases steadily with line length. This example illustrates an interesting point concerning the relative importance of radiation and resistive losses. Radiation loss from microstrip circuits are associated with fringing fields present at discontinuities, and are minimized through the reduction of the number of discontinuites, the use of electrically thin substrates, and through creative designs to be discussed further in the following sections. Resistive loss depends on the composition and shape of conductors, and increases with line length. For the following examples, where discontinuites are considered with relatively short lengths of line, only radiation loss will be included. The unit phase delay (Pd_1) can be defined as the phase shift (Pd) of the line divided by the number of periods (N). To demonstrate the effect of the cascading of several sections has on the phase, a meander delay line on a 25 mil alumina substrate has been analyzed. In Figure 4.15, the unit phase delay is shown as a function of frequency for cascades of 1, 2 and 3 periods, respectively. As shown, the unit phase delay is independent of the length of the line from 5-12 GHz. Thus, it can be used to accurately determine the phase for a line having many cascaded sections ($pd_N = N \times pd_1$). Deviations in the linear phase characteristic at the high frequency end result from high radiation and return loss. Shown in Figures 4.16 are the transmission parameter and radiation loss of the same line. In this example, the line has good transmission below 13 GHz, but the performance deteriorates rapidly after that. Furthermore, at high frequencies, the transmission through the line decreases while the radiation loss increases with line length. From these observations, in addition to acting as a delay line, the

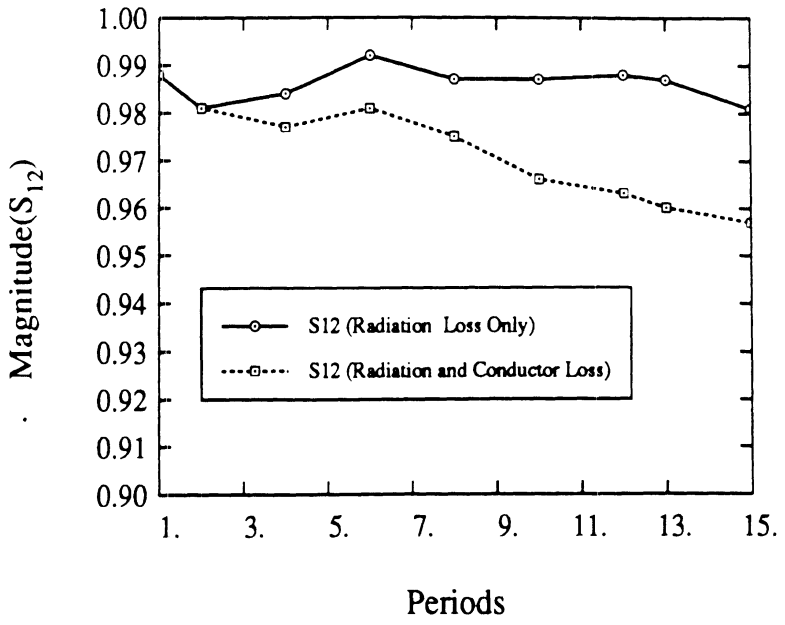

Figure 4.14: Transmission parameter magnitude of meander line as a function of length ($f = 20GHz, \epsilon_r = 2.2, h = 20mil, W = 10mil, S = 40mil, d = 50mil, t = 12\mu m, \sigma = 4x10^7 S/m$)

meander line is particularly well suited for filtering applications. This is true because the spacing and number of periods control the pass-band corner frequencies and slopes, respectively. This is a well known characteristic of periodic structures in general[62],[63],[64].

Meander line narrowband filter

Shown in Figures 4.17 and 4.18, theoretical results from this research are compared to theoretical results and experimental data derived by Jansen [17],[28] for shielded and open meander lines, respectively. There is good agreement between the open experimental results and our simulation. This structure has two pass-bands over the frequency range shown. Radiation losses are quite severe and result in

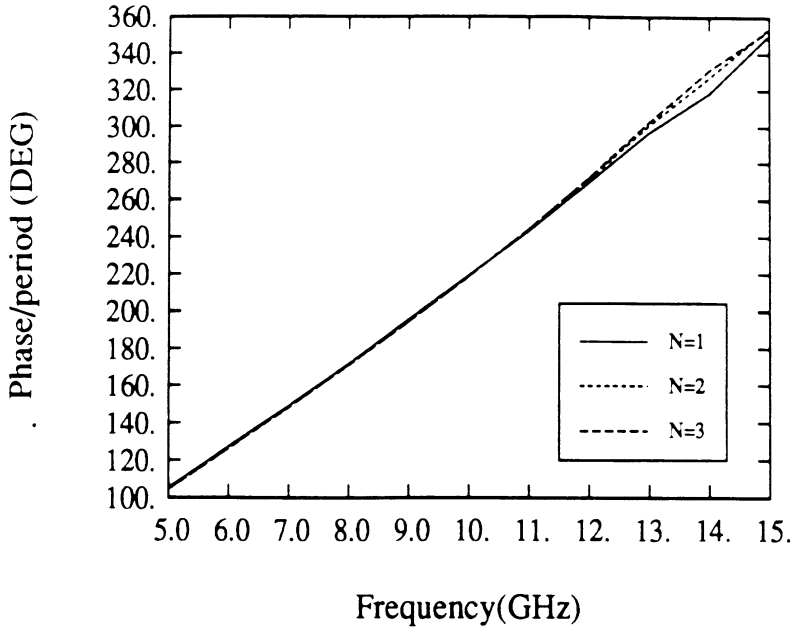

Figure 4.15: Phase of transmission parameter for meander line as a function of frequency ($\epsilon_r = 9.878, h = 25mil, W = .305mm, S = 4W, d = 5W$)

degradation of the transmitted power in the 13-20 GHz stopband, and the pencil-thin passband centered at 22.5 GHz. In particular, notice the difference at 22.5 GHz between the open and shielded simulations. This example illustrates that meander lines may be useful for narrowband applications in monolithic arrays, but also that they may experience severe radiation loss.

Effect of bend discontinuities in meander line

The propagation through a single loop of a meander line is investigated in the next example, revealing the effect of distributed discontinuities and electromagnetic coupling on the slow-wave properties of the structure.

The line is printed on a 10 mil alumina substrate ($\epsilon_r = 9.8$). The magnitude of S_{21} is shown in Figure 4.20 (a) as a function of frequency for three values of the width

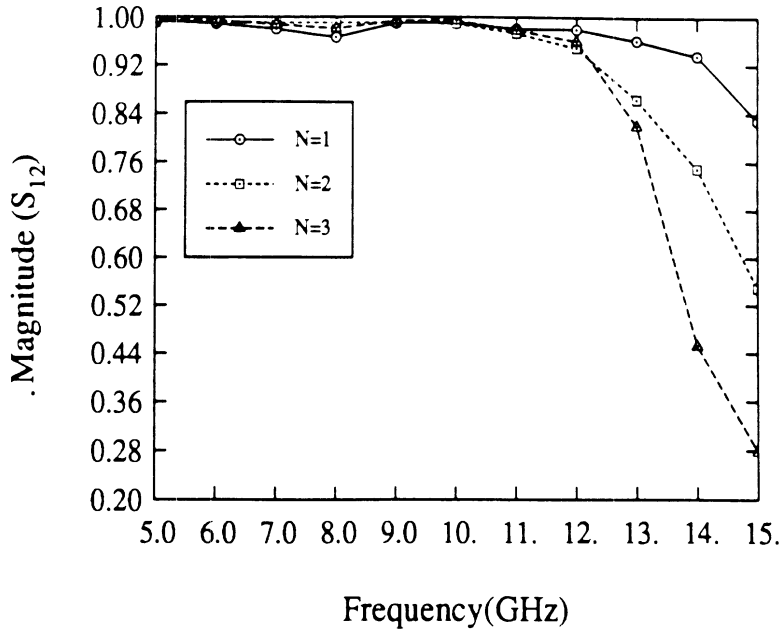

a. Transmission Parameter

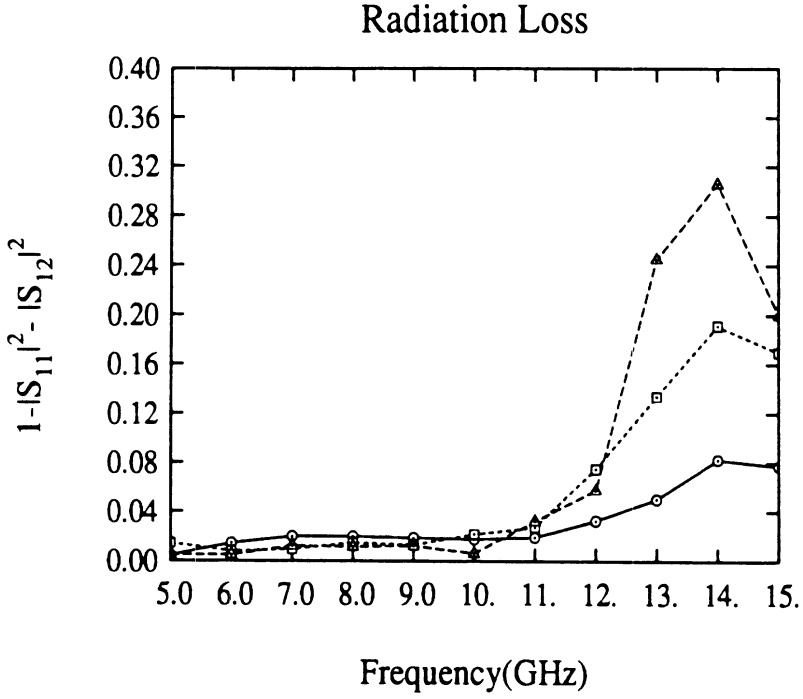

b.Radiation Loss

Figure 4.16: Magnitude of transmission parameter and radiation loss for meander line as a function of frequency ($\epsilon_r = 9.878, h = 25mil, W = .305mm, S = 4W, d = 5W$)

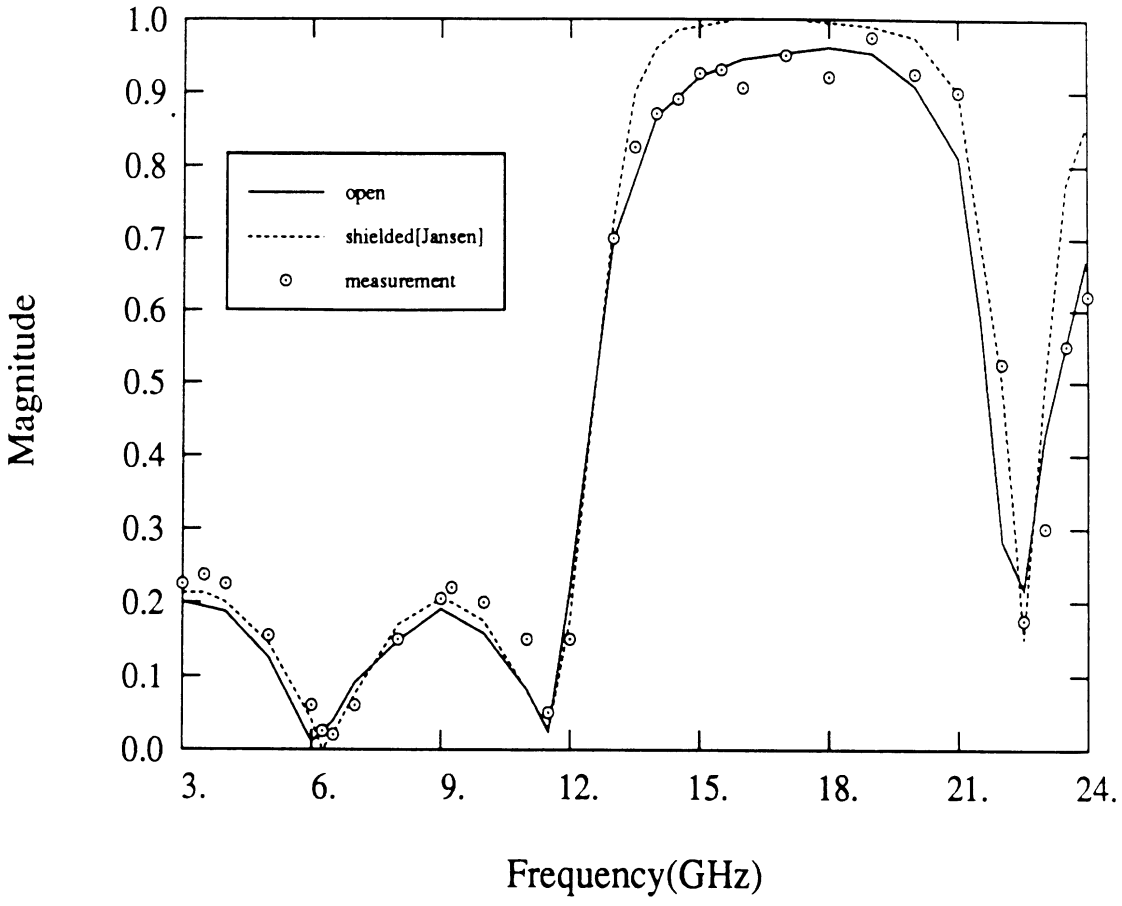

Figure 4.17: Magnitude of Reflection Coefficient for meander line filter as a function of frequency ($\epsilon_r = 9.878, h = 25mil, W = .61mm, S = \frac{1}{2}W, d = 4W$)

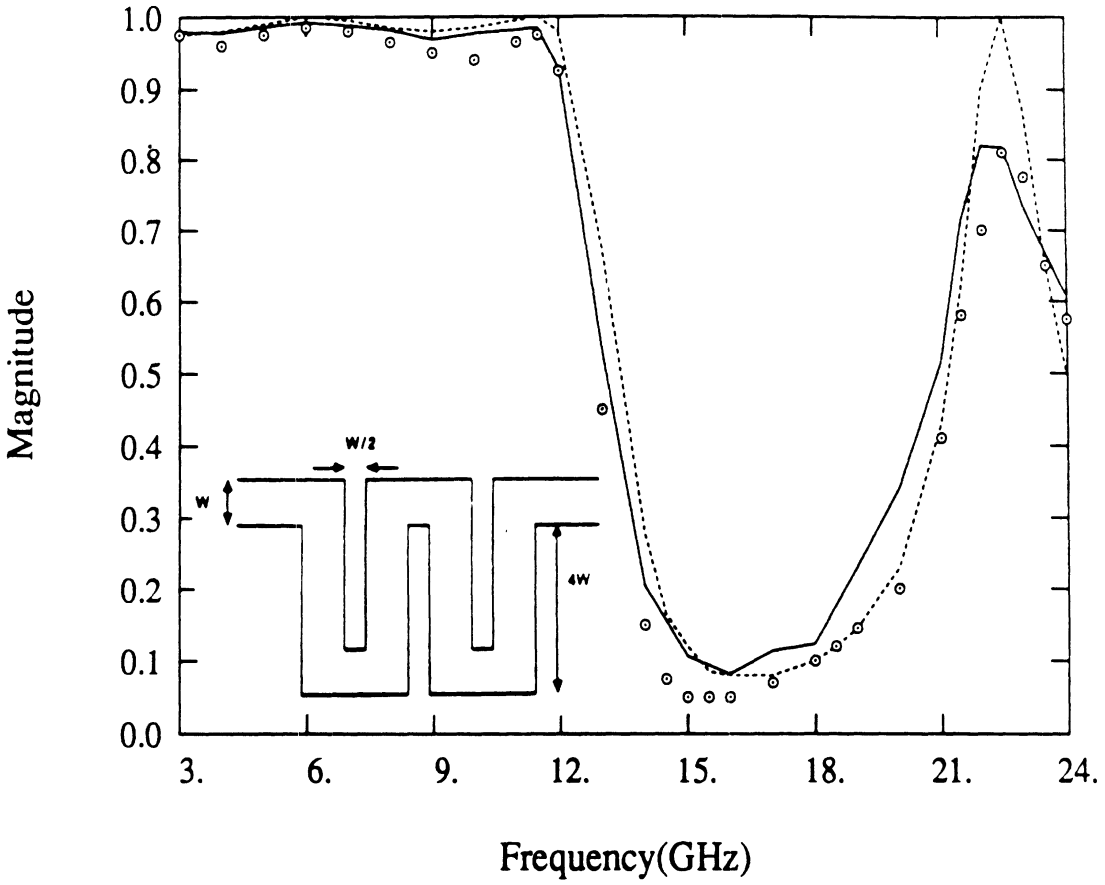

Figure 4.18: Magnitude of Transmission Parameter for meander line filter as a function of frequency ($\epsilon_r = 9.878, h = 25mil, W = .61mm, S = \frac{1}{2}W, d = 4W$)

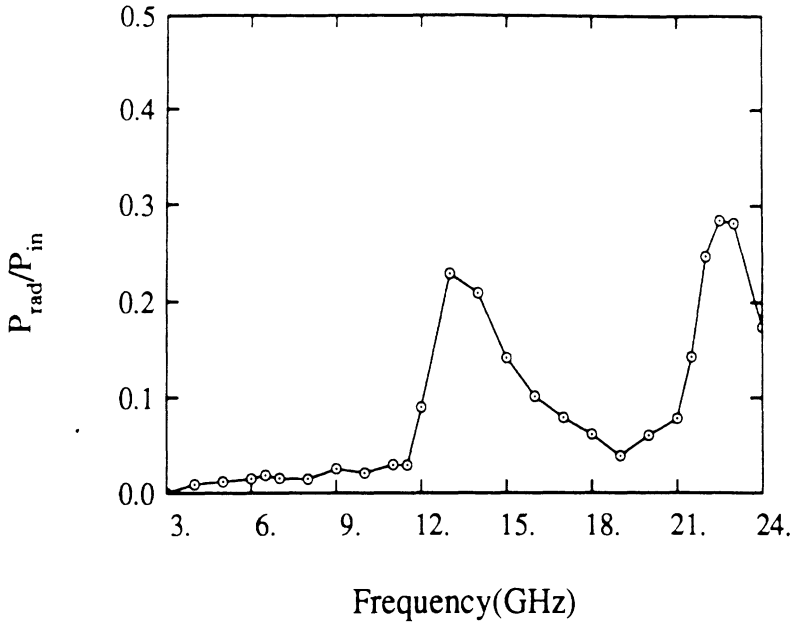

Figure 4.19: Radiation Loss for meander line filter as a function of frequency ($\epsilon_r = 9.878, h = 25mil, W = .61mm, S = \frac{1}{2}W, d = 4W$)

to spacing ratio ($\frac{w}{s}$). In addition, Figure 4.20(b) shows the normalized phase velocity around the loop (v'/v) as a function of frequency where v is the phase velocity on a microstrip line of length equal to the mean path length of the loop. These results indicate, in this frequency range, that the parasitics in the loop increase the phase velocity v' which in turn tends to reduce the overall slow-wave effect of the meander line.

4.3.5 Using the Step Approximation

Radial Stub

Microstrip radial stubs were fabricated and measured to test the validity of the step approximation for analysis of microstrip discontinuities. In Figure 4.21, the

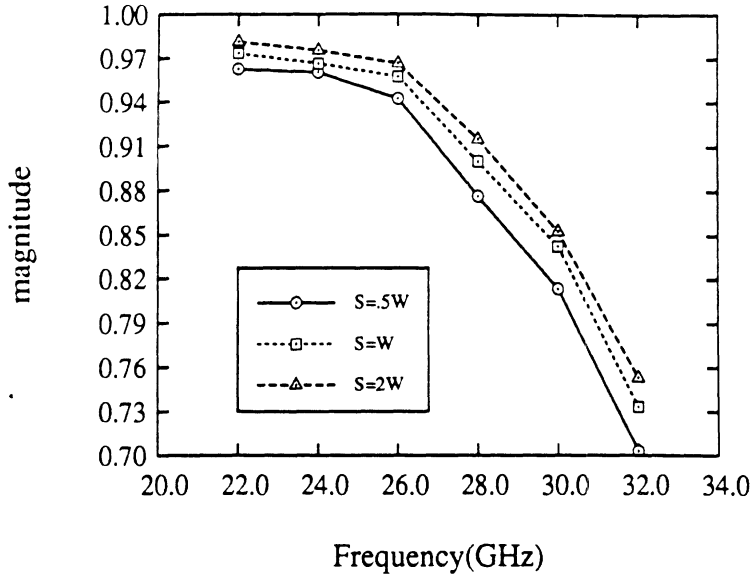

a. Transmission parameter

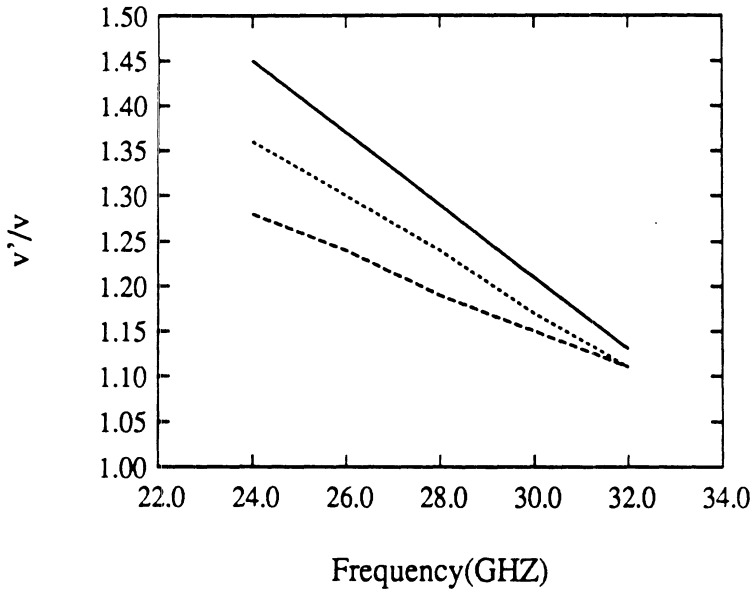

b. Phase Velocity

Figure 4.20: Design Curves for Meander Line (ϵ_r=9.8,h=.254 mm,W=.2,d=.8,N=1)

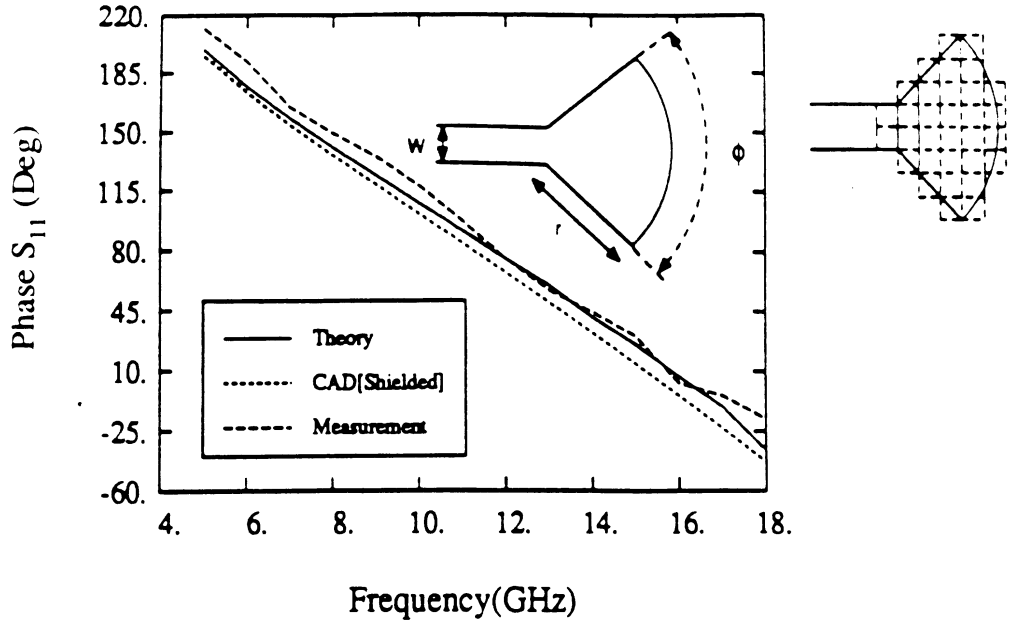

Figure 4.21: Phase of radial stub (W=25 mil, r=75 mil, ϕ=90 Deg, ϵ_r=10.65, h=25 mil)

results for a one-port radial stub are shown. Included in the figure is the discretization employed for its analysis. The agreement between measurement and theory is good, particularly at higher frequencies. At lower frequencies, the measurements may be influenced by the proximity of the launchers and fixturing, as well as the finite size of the substrate. In this experiment, the substrate was of smaller size than for the two-port structures measured. Also, included is a CAD[56] analysis which are in good agreement at lower frequencies, but deviate at higher frequencies because it models a shielded, lossless structure. A radial stub with the preceeding dimensions and substrate was also fabricated in a shunt configuration across a 50 ohm microstrip line. The results are shown in figure 4.22 with the corresponding theoretical data. The resonant frequency of the numerical results (again using the step approximation)

is smaller by about 100 MHz. This is due to a combination of the step approximation and experimental error.

Mitered Bend

Figure 4.23(a) displays the network parameters for mitered and right-angle bend discontinuities. The mitered case has superior behavior as illustrated by its improved return loss. Nonetheless, it is interesting to note that the two structures exhibit almost identical radiation properties at lower frequencies as shown in Figure 4.23(b). At higher frequencies the radiation loss of the right-angle bend becomes higher. It was found that the mitering, in this case, sharply lowers the return loss by decreasing the excess capacitance of the bend, and at higher frequencies it lowers the radiation loss as well.

Comparison of Rectangular, Radial and Triangular Stubs

Open circuit stubs are often used in microstrip matching networks, particularly in (M)MIC amplifiers. Radiation loss and spurious coupling from a matching network have a direct impact on the noise performance of an amplifier and must therefore be minimized. Several stub geometries have been proposed for enhancing various circuit characteristics including reduced loss. The fullwave analysis presented has been employed to evaluate three types of stubs: a)rectangular, b)radial, and c) triangular in terms of their bandwidth, resonant characteristics, and radiation properties. The stubs are printed on a 25 mil GaAs substrate ($\epsilon_r = 12$), and have dimensions shown in Figure 4.24. For comparison purposes, all of the stubs are designed to have first resonance at about 24 GHz. Two-port scattering parameters have been obtained by positioning the stubs shuntly across a transmission line, as shown. At resonance,

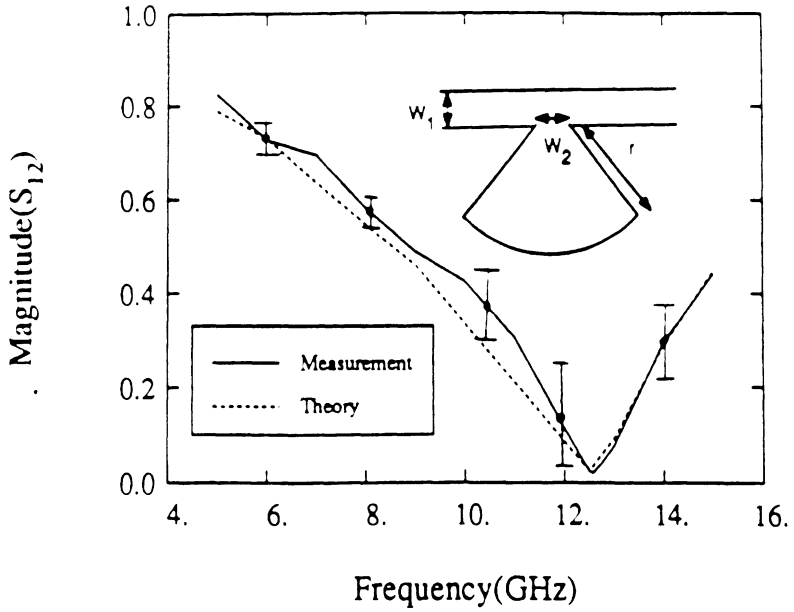

a. Magnitude

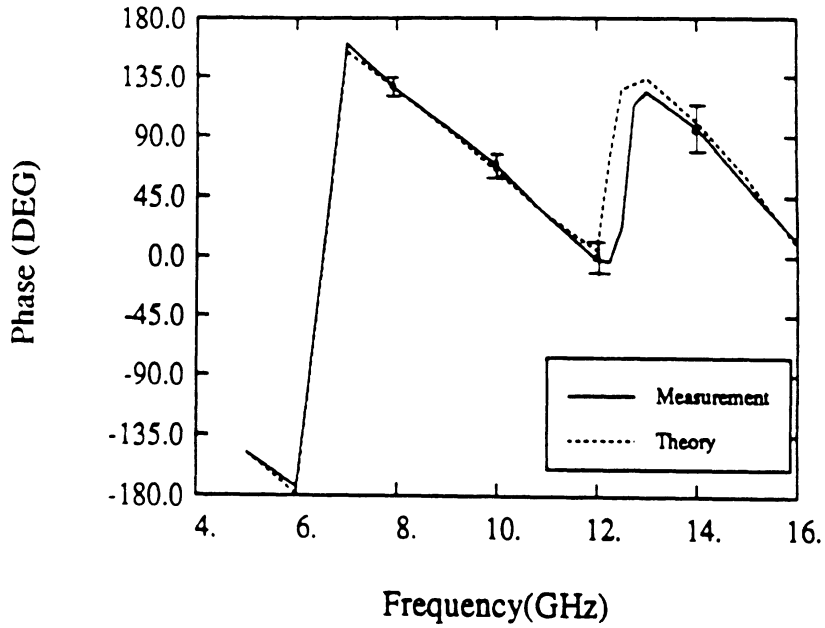

b. Phase

Figure 4.22: Scattering Parameters of Microstrip radial stub, theoretical(experimental) dimensions: W1=25 mil, W2=25mil, r=75 mil, ϕ=90 Deg, ϵ_r=10.65, h=25 mil

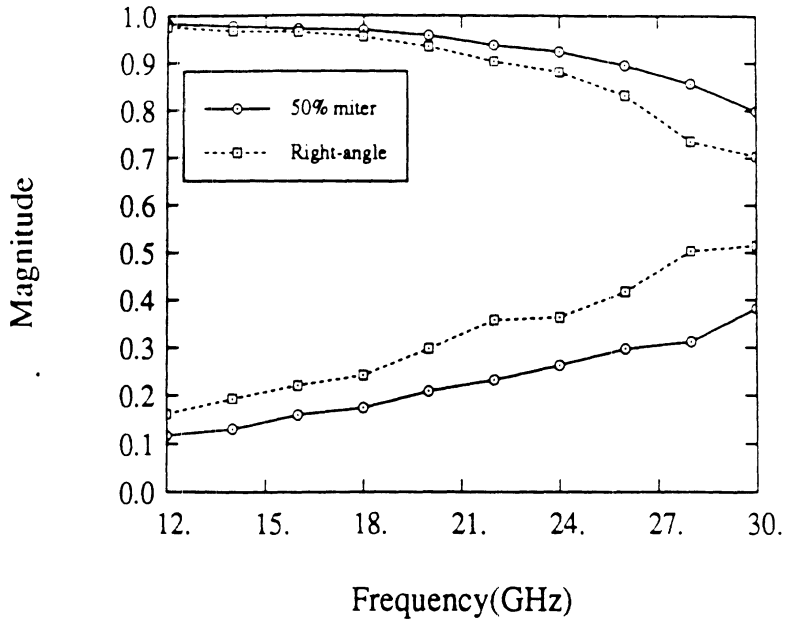

a. Scattering Parameters

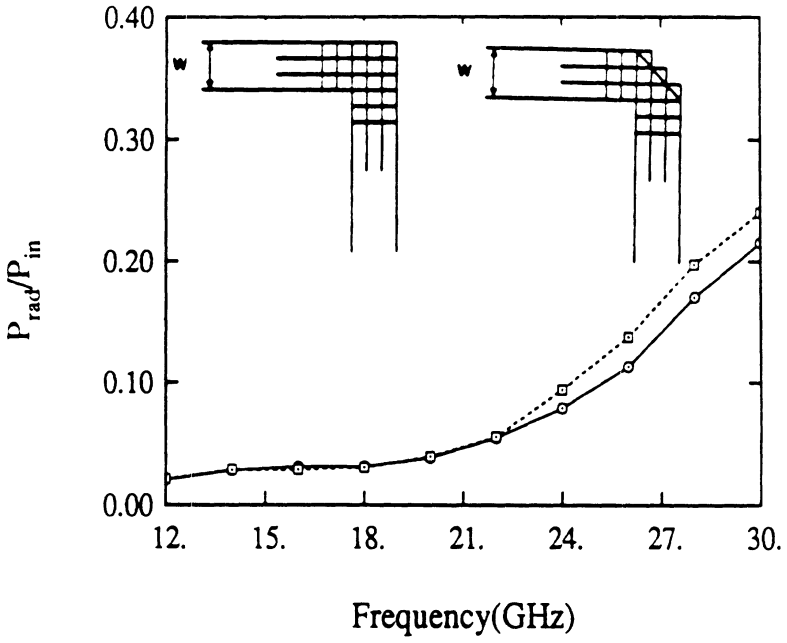

b. Radiation Loss

Figure 4.23: Network Parameters(magnitude) for right-angle and mitered bends ($\epsilon_r = 12, h = 25mil, W = 15mil$)

the magnitude of the transmission parameter reaches a minimum. Due to radiation loss, which may be viewed as a radiation resistance at the junction, this minimum is not zero as it would be in the lossless case. Figure 4.25(a) shows the transmission parameters for the three cases from 15 to 28 GHz. As shown, the radial stub has the broadest bandwidth, and the triangular stub has the narrowest. These results indicate that the bandwidth may be adjusted by varying the angle of the radial stub. However, it should be noted that such a modification will also shift the resonant frequency.

As previously mentioned, radiation from matching networks has a direct and derogatory effect on noise performance in (M)MIC amplifiers. Figure 4.25(b) shows quite clearly that the triangular shape radiates more than the other two types. Additionally, the radial stub shows moderate improvement over the rectangular type. The loss peaks for all three cases at 27 GHz (about 3-4 GHz beyond resonance), indicating that the radiation properties are heavily influenced by the characteristics of the substrate. For the given substrate at this operating frequency, the loss is primarily due to the TM_0 substrate mode. We conclude that since the triangular stub has the smallest bandwidth, and radiates most severely, it is only recommended for narrowband applications where the additional loss may be tolerated. The rectangular and radial stubs have similar radiation properties, with the radial stub having a broader band response.

4.4 Multi-Port Networks

Transmission line junctions are found in virtually every type of microstrip layout and are integral parts of power splitters, matching networks, and couplers. Consequently, a thorough understanding of their parasitic behavior is crucial in high

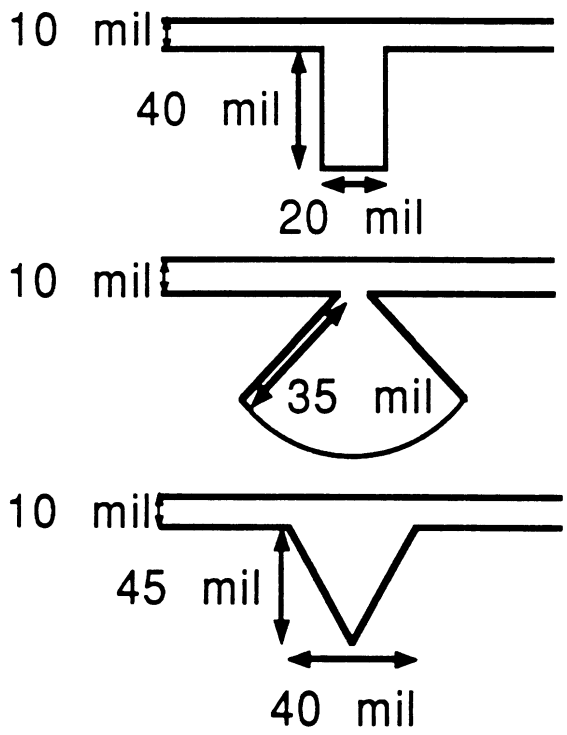

Figure 4.24: Types of Microstrip stubs ($\epsilon_r = 12, h = 25mil$)

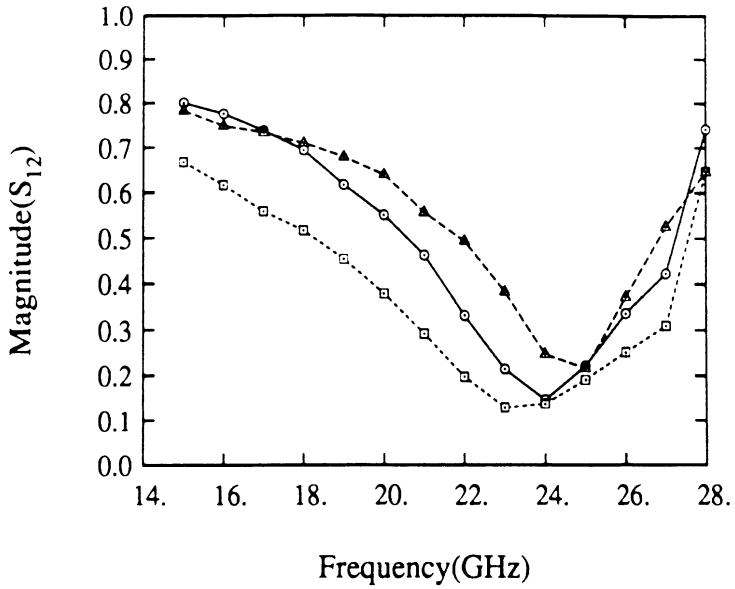

a. Transmission parameters

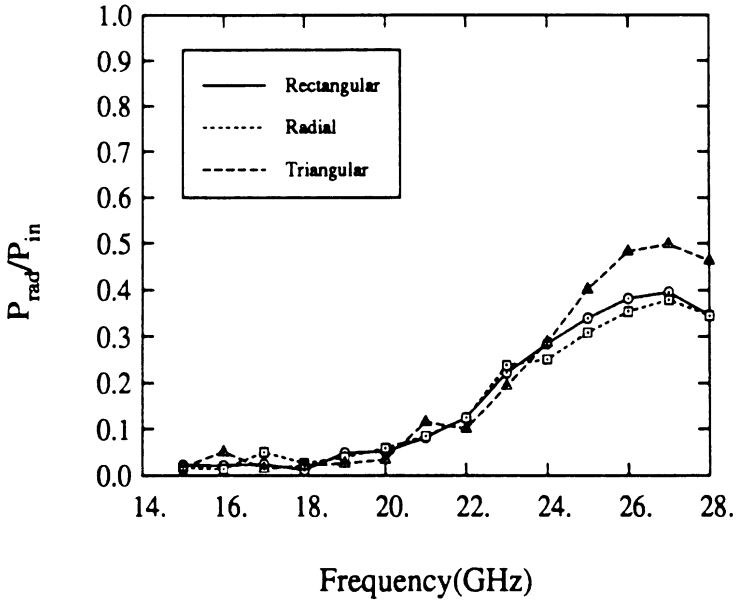

b. Radiation Loss

Figure 4.25: Transmission parameter and fRadiation Loss of microstrip stubs ($\epsilon_r = 12, h = 25mil$)

frequency (M)MIC design. Network parameters have been determined for three-port T-junction and four-port cross junction discontinuities with interesting results.

4.4.1 Cross and T-junction discontinuities

As shown in Figure 4.26, the magnitude of the S-parameters of a T-junction on a 25 mil duroid ($\epsilon_r = 2.2$) substrate agree well with available CAD results [56]. On the the other hand, as shown in Figures 4.27 and 4.28 for tee and cross junctions respectively, the phase can disagree appreciably with those predicted by commercial CAD, particularly between ports at right angles. The disagreement arises because of the parasitic reactance and radiation loss (shown in Figure 4.29) at the junction.

Also shown in Figure 4.29 are the radiation losses of a right-angle bend having the same strip width and printed on the same substrate. The three types (right-angle bend, cross, and tee) of junctions exhibit similar radiation losses. The lowest loss corresponds to the cross junction which is the only one of the three not having a port current terminate at an edge.

4.5 Multi Dielectric Layer Structures

A powerful advantage of the presented formulation is the ability to model multi-layer substrates by replacing the single layer Green's function with a more general multi-layer Green's function. This allows the analysis of a much wider class of problems, previously uninvestigated, involving substrates made of combinations of materials and/or the presence of a superstrate. The fullwave procedure was applied to a microstrip corner discontinuity on a substrate having two dielectric layers. The magnitude of the scattering parameters is shown in Figure 4.30. The multilayer corner has been analyzed on four different substrates: A) a 40 mil layer of alumina

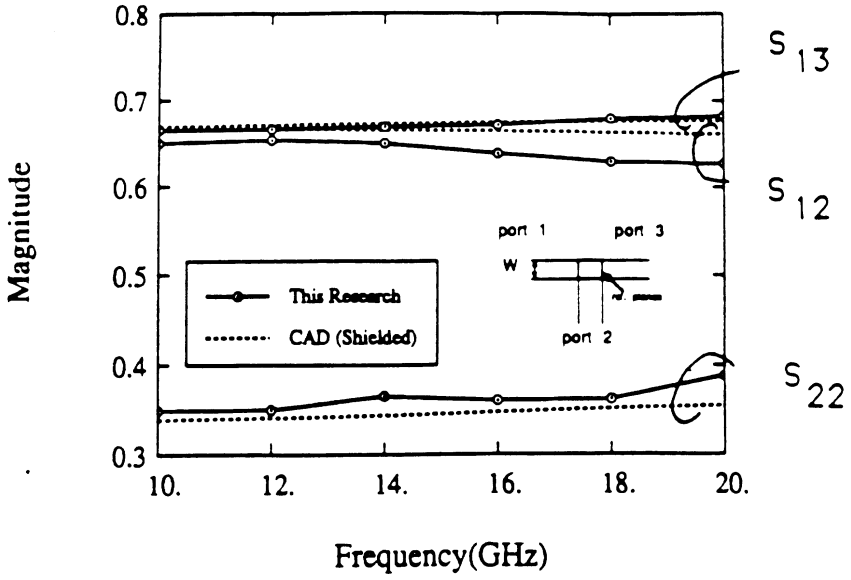

Figure 4.26: Scattering Parameters(magnitude) for microstrip T-junction as a function of frequency ($\epsilon_r = 2.2, h = 25mil, W = 25mil$)

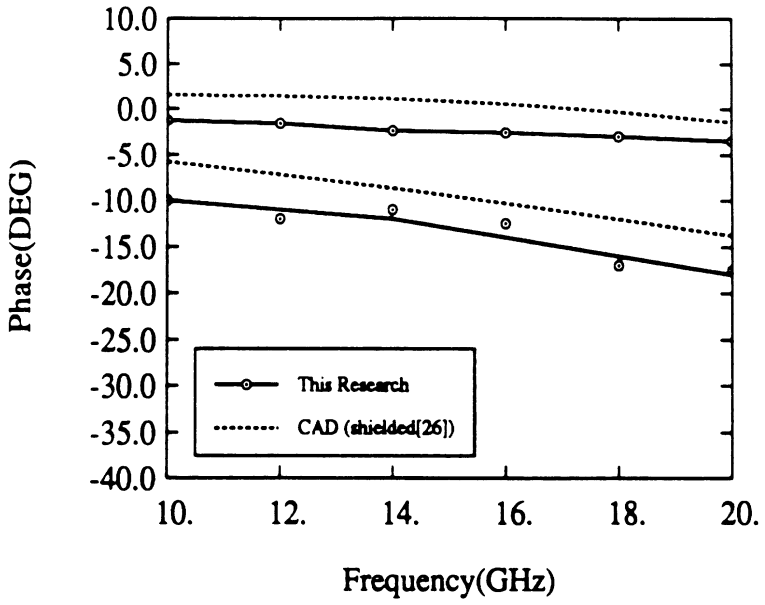

Figure 4.27: Scattering Parameters(phase) for microstrip T-junction as a function of frequency ($\epsilon_r = 2.2, h = 25mil, W = 25mil$)

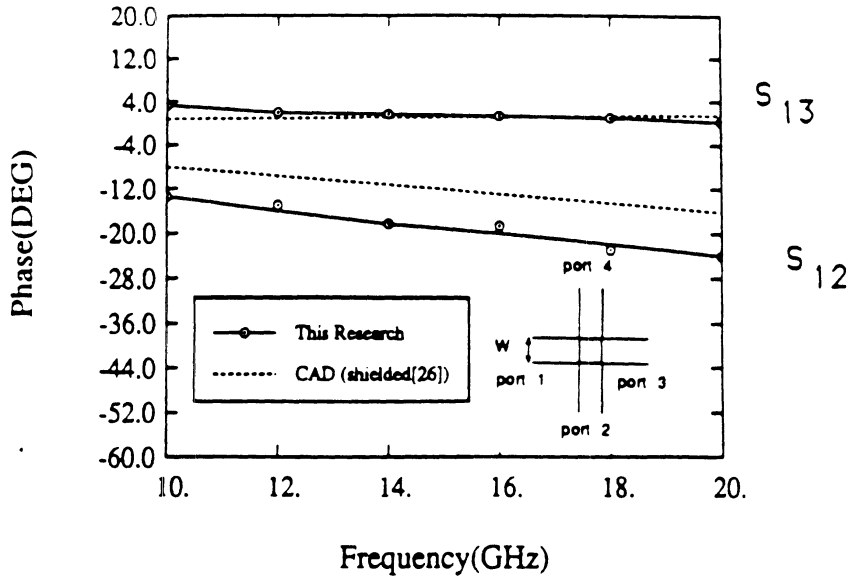

Figure 4.28: Scattering Parameters(phase) for microstrip cross junction as a function of frequency ($\epsilon_r = 2.2, h = 25mil, W = 25mil$)

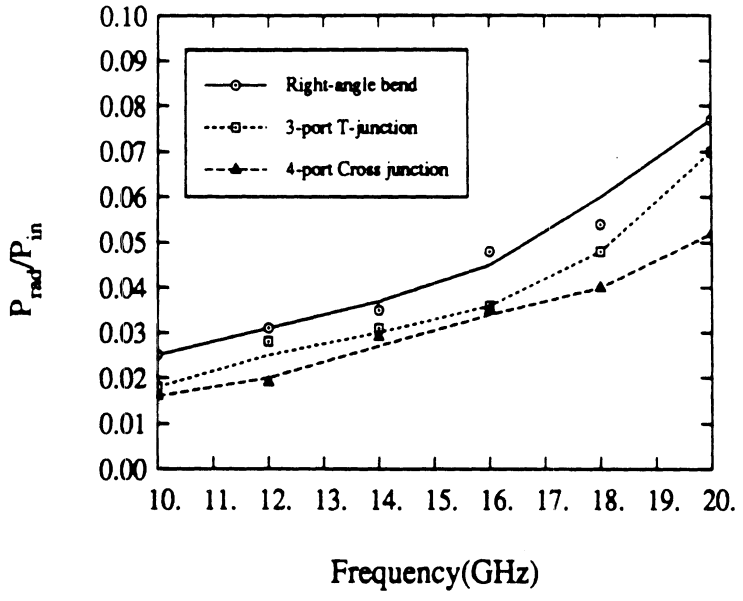

Figure 4.29: Radiation Loss in microstrip junctions (bend,cross,tee) ($\epsilon_r = 2.2, h = 25mil, W = 25mil$)

Table 4.5: Substrate parameters of multilayer microstrip bends

Case	ϵ_{r1}	ϵ_{r2}	$h_1(mil)$	$h_2(mil)$
A	10.2		40	0
B	2.2		40	0
C	2.2	10.2	20	20
D	10.2	2.2	20	20

($\epsilon_r = 10.2$), B) a 40 mil layer of duroid ($\epsilon_r = 2.2$), C) a 20 mil layer duroid on a 20 mil layer of alumina, and D) a 20 mil layer of alumina on a 20 mil layer of duroid. It was found that there is significant difference in radiation between the two multilayer cases. The radiation from the structure having duroid over alumina is considerably more than the structure having alumina over duroid, as illustrated in Figure 4.31. The loss is primarily due to surface wave radiation in this structure. Therefore, case D couples less power into surface waves than case C. This will be discussed more extensively in Chapter 6.

A two-layer microstrip stub was also analyzed. Shown in Figure 4.32 is the magnitude of the scattering parameters for a stub on substrate having a layer of GaAs ($\epsilon_r = 12.2$) on Quartz ($\epsilon_r = 4.0$). Both layers are .2 mm thick. Also included are the scattering parameters for a stub having the same dimensions on a single layer of quartz. The single layer example has a resonant frequency at 41 GHz. The higher effective dielectric constant for the 2-layer case creates a stub having a smaller resonant length, reflected in a downward shift in the null of $|S12|$. The radiation losses for both stubs are included in Figure 4.33. As illustrated, the multilayer stub shows a tendency to radiate less. This indicates that multilayer substrates may be utilized to reduce radiation losses.

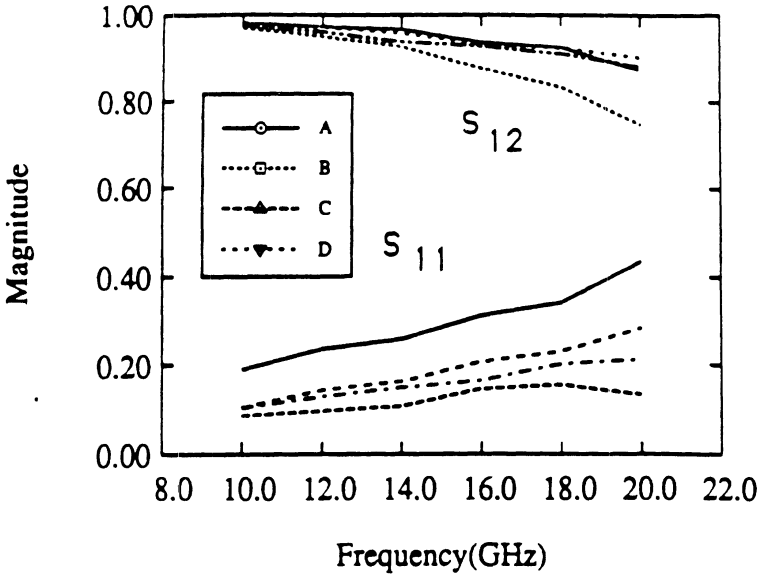

Figure 4.30: Scattering Parameters For Multilayer Microstrip Corner (W=20 mil)

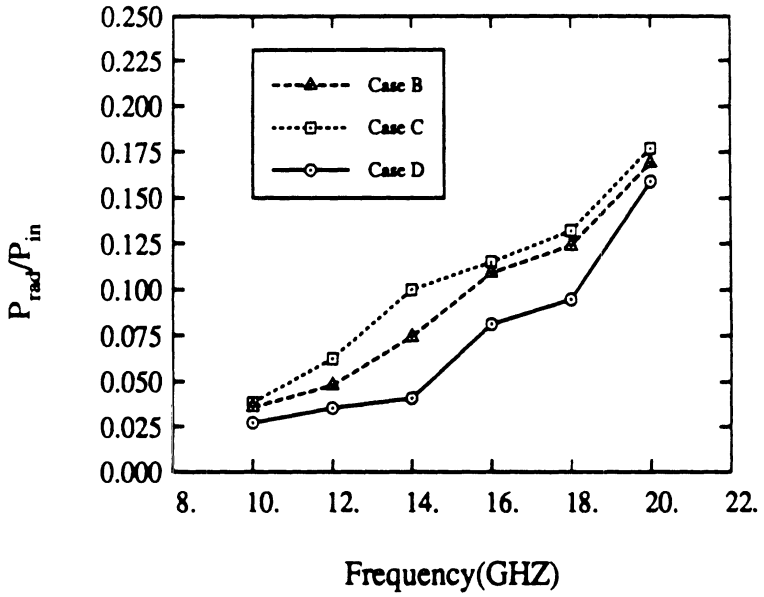

Figure 4.31: Radiation From Multilayer Microstrip Corner(W=20 mil)

Table 4.6: Substrate parameters of multilayer microstrip stubs

Case	ϵ_{r1}	ϵ_{r2}	$h_1(mil)$	$h_2(mil)$
1 layer	10.2		40	0
2 layer	10.2	2.2	20	20

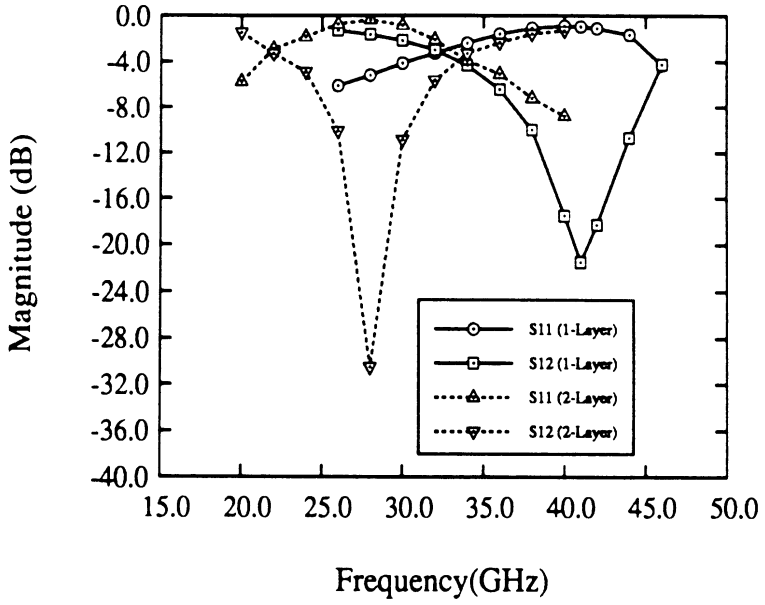

Figure 4.32: Scattering Parameters For Multilayer Microstrip Stub (W1=W2=.25mm,L=1 mm)

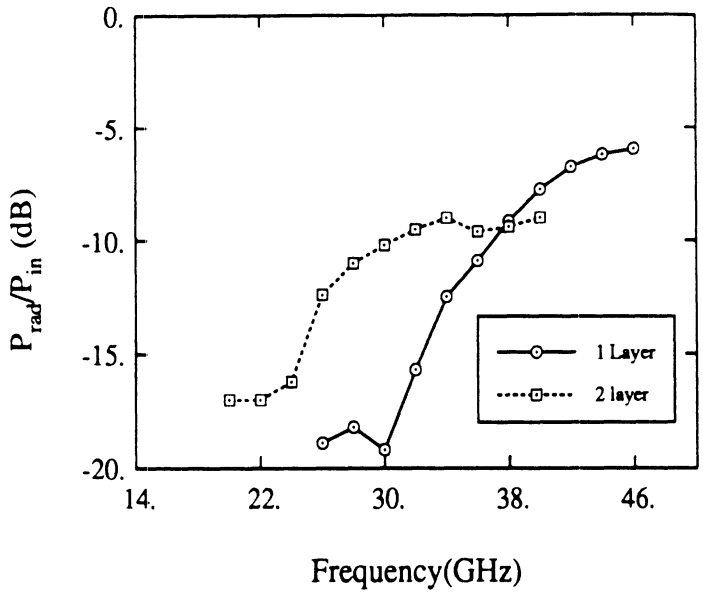

Figure 4.33: Radiation From Multilayer Microstrip Stub (W1=W2=.25mm,L=1 mm)

CHAPTER V

RADIATION PROPERTIES

5.1 Introduction

In previous chapters, open microstrip structures were analyzed with the method of moments. Circuit elements were characterized by their network parameters, from which total radiation loss was obtained. In this chapter, total radiation loss is separated into the individual contributions of space and surface wave loss. Space waves refer to the modes radiated into the semi-infinite region above the dielectric; and surface waves are modes bound in the substrate, which forms a grounded dielectric waveguide. In addition, theoretical and experimental surface wave patterns depicting the direction of propagation of surface wave radiation in the dielectric substrate are presented. These far-field patterns are useful for determining where coupling through surface wave excitation may be strong. Space wave far-field patterns have a null along the dielectric substrate, except under very rare circumstances (at the cutoff of higher order surface wave modes), which are not applicable to the presented results. Furthermore, surface wave radiation is in the form of cylindrical waves which decay less rapidly with distance than spherical space waves. It is therefore reasonable to conclude that surface waves play a major role in undesirable electromagnetic interference. In addition, substrate composition will be shown to have a strong influence

on radiation properties.

Results in this chapter will provide guidelines for the development of low-loss microstrip elements. For example, it is well known that the shape of discontinuities can be altered to improve circuit performance (eg. mitered bend, radial stub). However, finding the influence of these and similar modifications on the radiation loss is also important. This analysis will provide the necessary quantitative results for determining when and why a specific circuit modification decreases radiation loss.

In section 5.2, the experimental approach for obtaining surface wave patterns is presented. This is followed by experimental and theoretical results for far-field patterns, which illustrate the direction of surface wave propagation in the substrate. Section 5.3 will give examples of total surface and space wave losses for microstrip stubs and bends. Finally, in section 5.4 the effect of substrate composition on radiation properties is investigated. Microstrip examples presented will include substrate/superstrate and two layer substrate combinations.

5.2 Surface Wave Measurements

Power measurements were made of the dominant surface wave mode excited by microstrip discontinuities. This mode (TM_0) is polarized with its electric field in the direction perpendicular to the microstrip substrate. The measurements were made on a 96 mil duroid substrate ($\epsilon_r = 2.3$). The relatively thick substrates were chosen to facilitate positioning of the receiving antenna. The substrates were machined into 5 inch diameter circular sections whose edges were gradually tapered as shown in Figures 5.1 and 5.2 for open-end and radial stub discontinuities, respectively. This was to minimize the reflection of the surface wave at the edge of the substrate. The microstrip element, in this case a radial stub, was etched from the copper metalliza-

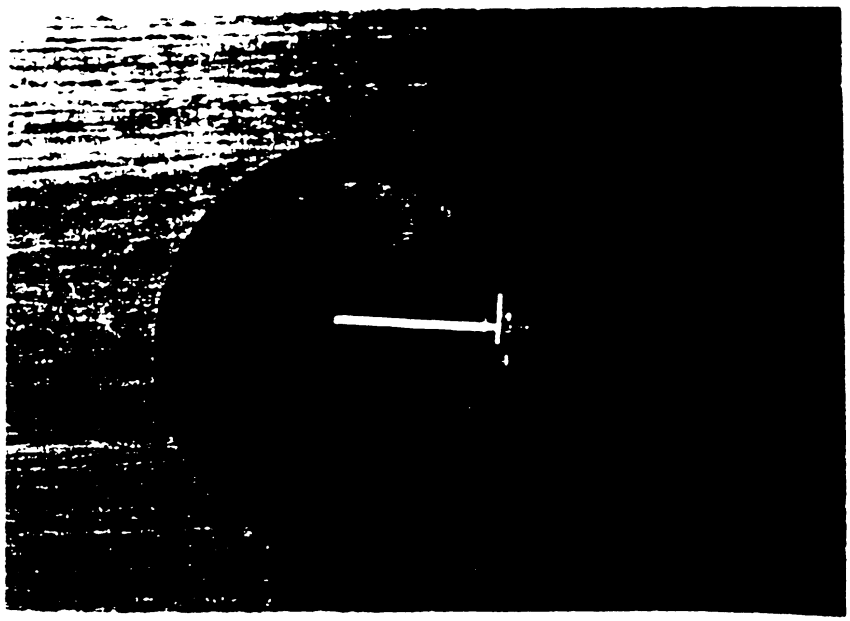

Figure 5.1: Open end discontinuity on Printed Duroid Substrate ($\epsilon_r = 2.3, h = 95mil, W = 100mil$)

tion on the top face of the substrate. The experimental setup is shown in Figure 5.3. The substrates were elevated onto a rotating pedestal and surrounded by absorber to minimize multiple reflections. Absorber was placed over the microstrip coax-to-microstrip launcher to minimize extraneous radiation. Each element was fed at the edge of the substrate with a 10 GHz signal and a resonant dipole was positioned near the edge to measure the pattern. The pedestal was then rotated to alter the observation angle (ϕ). Care was exercised in maintaining the dipole at a constant substrate level as the substrate was rotated. A typical pattern is obtained in Figure 5.4. The pattern represents the power in the TM_0 surface wave mode, because far-field space wave fields are zero along the dielectric interface, and no higher order surface wave modes are excited at the 10 GHz operating frequency.

Open-Ended Line

The experimental results for a 100 ohm (W=100 mil) open-ended line was compared to the theoretical results derived by the previously presented method. Initially,

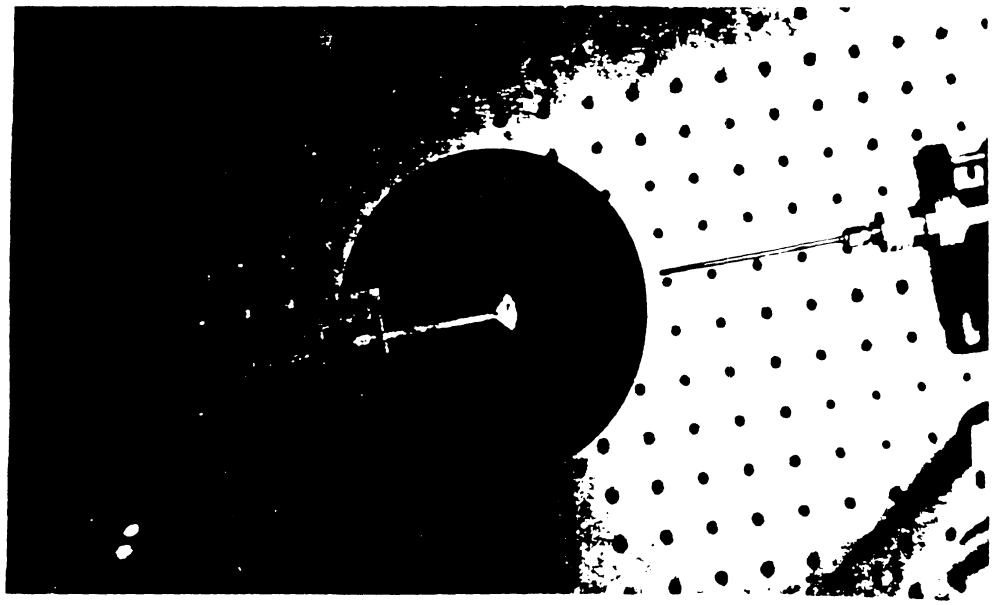

Figure 5.2: Microstrip Radial Stub on Printed Duroid Substrate ($\epsilon_r = 2.3, h = 95mil, W = 100mil$)

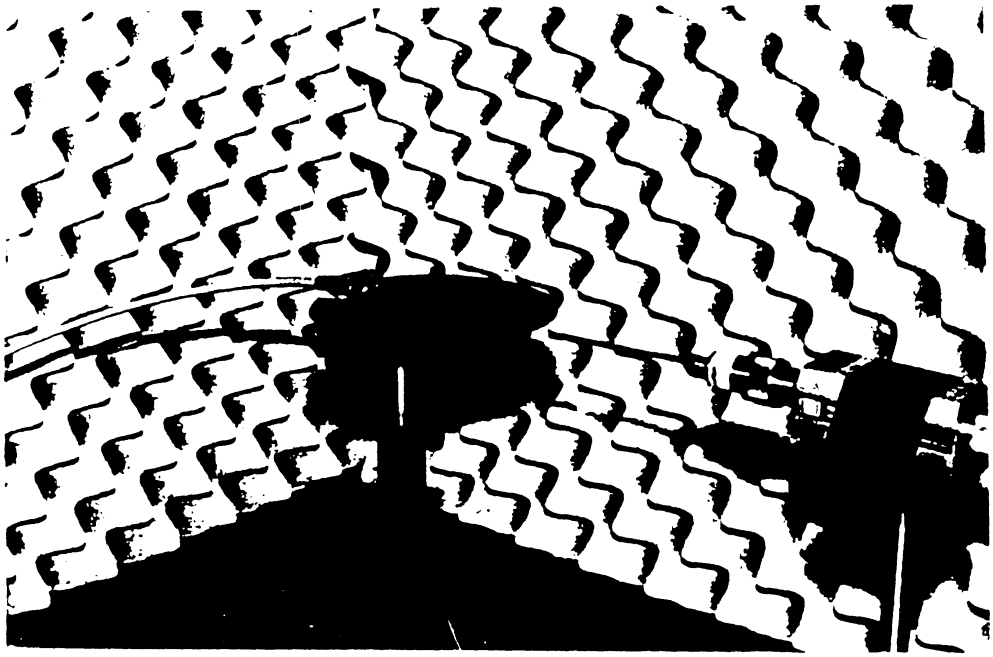

Figure 5.3: Experimental Setup for Surface Wave Pattern Measurements ($\epsilon_r = 2.3, h = 95mil, W = 100mil$)

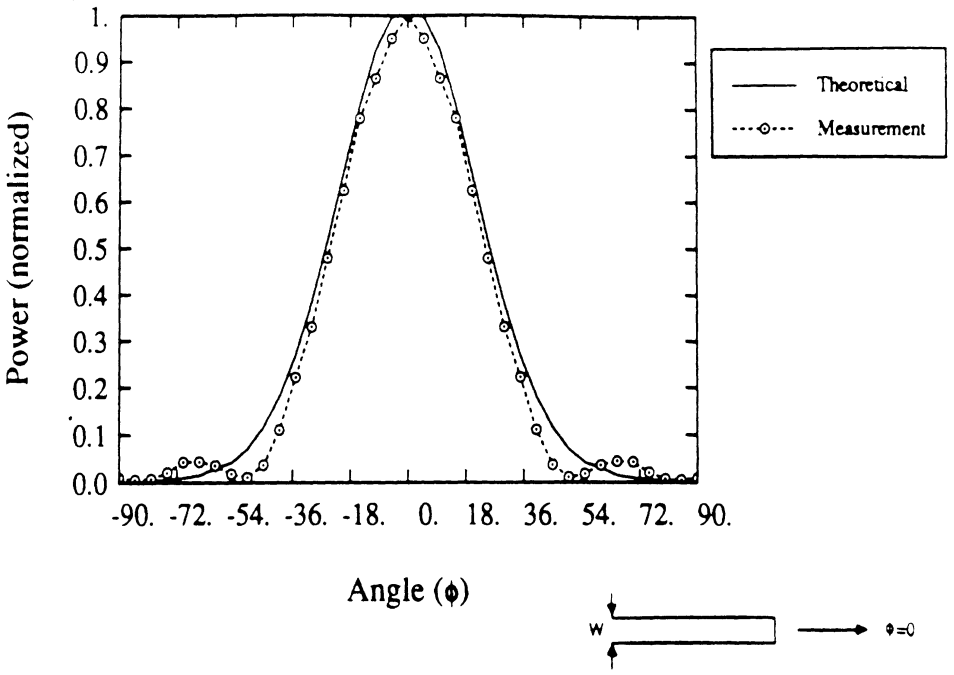

Figure 5.4: Surface Wave Pattern of Open-ended Line (semi-infinite feed) ($\epsilon_r = 2.3, h = 95mil, W = 100mil$)

the theoretical model assumed that the discontinuity was fed by a semi-infinite line. to remove the radiation effects of the finite line length and isolate the radiation of the open-end. Figure 5.4 shows that the theoretical results agree well with the experimental results. The open-ended line radiates power in the TM_0 surface wave along the longitudinal axis of the line. The experimental results include the effect of finite line length as demonstrated by the side-lobes in the pattern. To verify the presence of these lobes, the theoretical results were re-computed considering the finite length of line as utilized in the experiment. The new theoretical results and experimental data were now in excellent agreement (Figure 5.5). Also note that the beamwidth of the surface wave pattern becames narrower.

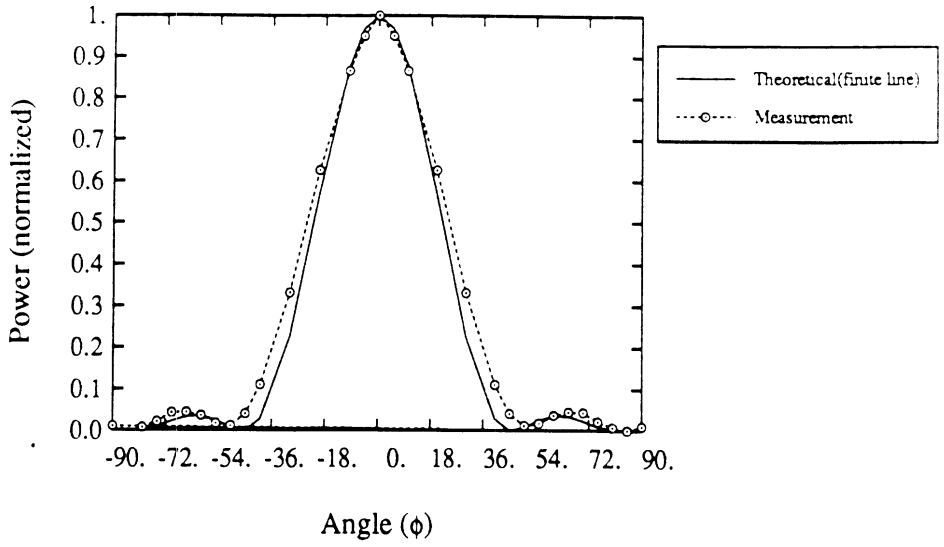

Figure 5.5: Surface Wave Pattern of Open-ended Line (finite feed) ($\epsilon_r = 2.3, h = 95mil, W = 100mil$)

Radial Stub

The TM_0 surface wave pattern of the previously shown radial stub (Figure 5.2). was measured. The 350 mil radial portion swept out an angle of 90 degrees and was fed by a 100 ohm microstrip line. Radial stubs are useful as broader band elements in (M)MIC design. Figure 5.6 shows the theoretical results for semi-infinite and finite length lines, as compared to experiment. The results are very similar to those obtained for the open-ended line, with the surface wave power excited along the longitudinal axis.

Bend Discontinuity

A two-port right-angle bend discontinuity, shown in Figure 5.7, was fabricated and measured. Experimentally, port 2 was left open-ended at a distance of two free

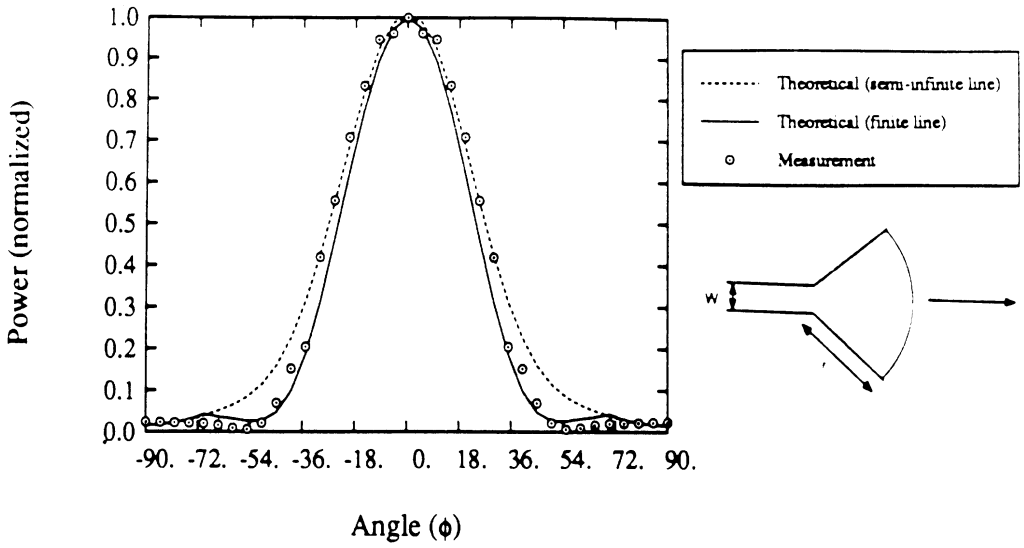

Figure 5.6: Surface Wave Pattern of Radial Stub ($\epsilon_r = 2.3, h = 95mil, W = 100mil, r = 300mil$)

Bend Discontinuity

A two-port right-angle bend discontinuity, shown in Figure 5.7, was fabricated and measured. Experimentally, port 2 was left open-ended at a distance of two free space wavelengths from the bend discontinuity. The theoretical model assumed a semi-infinite feed line (shown as $\phi = 0$ direction in picture), and that the second port was left open-ended, but extended far from the discontinuity. This extension maintains the standing wave ratio on the line, but removes the effects of the open end and finite line lengths; thus, isolating the effect of the bend. Shown in Figure 5.7, the agreement between theory and experiment is good. The experimental results show the combined effects of finite line length and the open-end. This results in the disagreement between the theory and experiment around 45 degrees. The side-lobe present at 90 degrees in both the theoretical and experimental results comes from

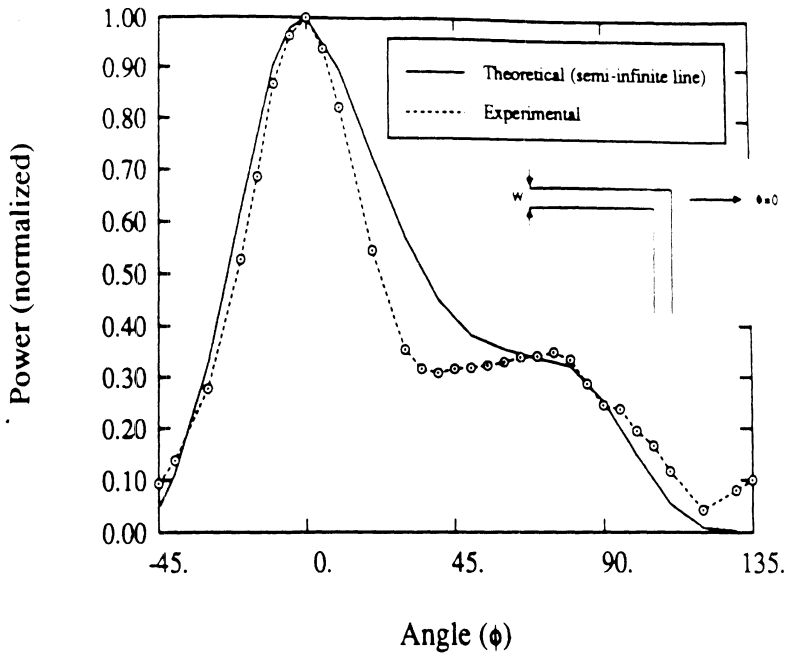

Figure 5.7: Surface Wave Pattern of Right-Angle Bend ($\epsilon_r = 2.3, h = 95mil, W = 100mil$)

the power reflected at the open-end which returns to the bend and radiates there. This lobe would be smaller, if the second port were matched.

5.3 Space and Surface Wave Radiation Losses

Stubs

In Figure 5.8, examples of open-ended and radial microstrip stubs are shown. These elements are frequently utilized in matching networks. The radial stub is generally utilized for its greater bandwidth. In Figure 5.9, the contributions of space and surface waves to total radiation loss is given for the open-ended stub. In the lower frequency range, the space wave contribution is slightly larger. However, the surface wave loss increases sharply with frequency, overtaking the space wave power

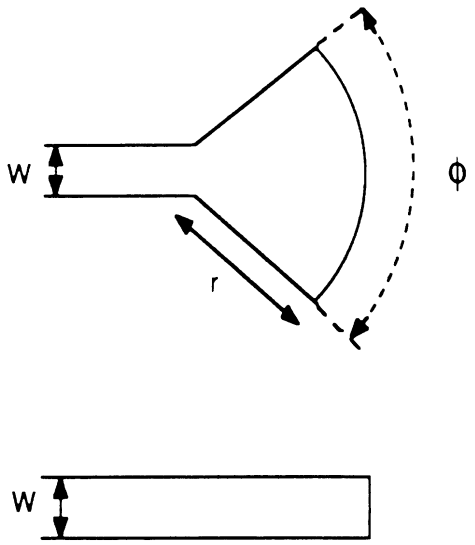

Figure 5.8: Microstrip Open-ended and Radial Stubs ($\epsilon_r = 12, h = 25mil, W = 10mil$)

at 20 GHz. Beyond 20 GHz, the total radiation loss increases sharply due to a corresponding increase in surface wave loss. The total radiation loss approaches half of the input power at 34 GHz.

Radiation loss for the radial stub, shown in Figure 5.10, exhibits a similar behavior to the open-ended stub, except that the sharp increase in surface wave and total radiated power is shifted upward. This behavior results in less radiation loss in the 20-30 GHz range of operation, but greater loss above 30 GHz. The lowest order TE_0 mode activates between 35 and 36 GHz, therefore, only one surface wave mode is excited in this example. The loss is expected to continue to increase until the first higher order mode is excited, and then it will oscillate as reported in [20]. Although the shape of the metallization has a strong influence on the total loss, it does not appear to have a greater influence on either type at lower frequencies as shown in

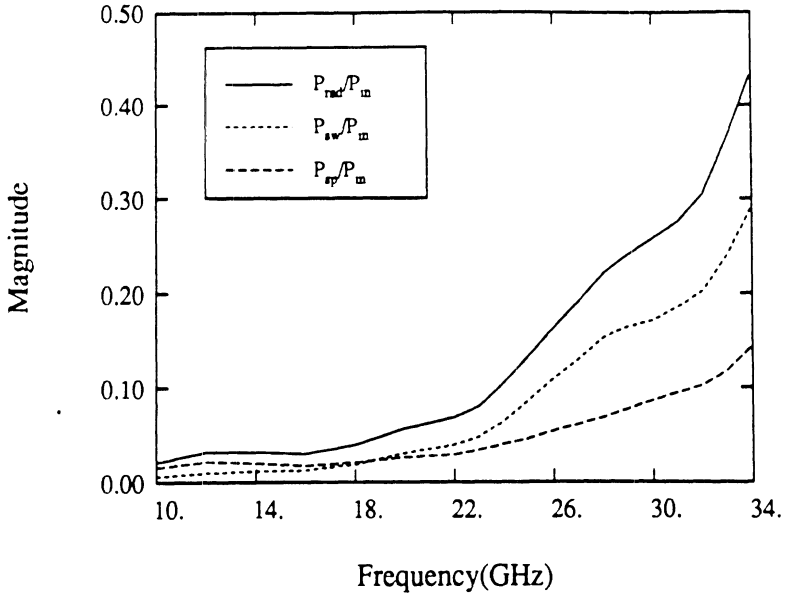

Figure 5.9: Radiation Loss of Open-Ended Stub ($\epsilon_r = 12, h = 25mil, W = 10mil$)

Figure 5.11. However, above 30 GHz the radial stub radiates a higher percentage of power into the excited surface wave mode.

Mitered bend

Chamfering of microstrip bends is a common practice for the reduction of input VSWR. The example shown in Figure 5.12 clearly illustrates that mitering can result in lower radiation loss as well. The losses between the mitered and right-angle bend are effectively equal until 20 GHz ($h = .127\lambda_g$). Beyond this frequency, the right-angle bend clearly radiates more power. Figure 5.13 shows that, once again, the radiation is dominated by surface waves at higher frequencies. However, the mitering produces a reduction in both space and surface wave power as illustrated in Figure 5.14, where both the mitered and unmitered cases exhibit identical percentages of

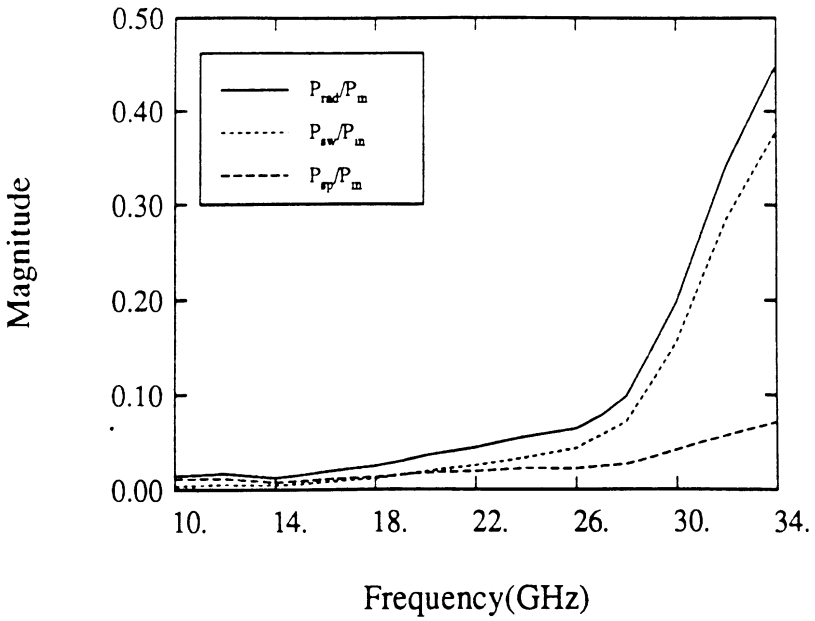

Figure 5.10: Radiation Loss of Radial Stub ($\epsilon_r = 12, h = 25mil, W = 10mil$)

surface wave loss. Therefore, mitering effectively increases the useful range of operation of the bend element. A similar discontinuity printed on a lower permittivity substrate would exhibit lower, but still significant, surface wave losses.

5.4 Reduction of Surface Wave Power with Multiple Layers

As discussed extensively in the literature [70], the efficiency of a printed antenna depends on the shape and size of the antenna and on the properties of the dielectric substrate. An extensive study performed by [70],[71] has shown that the use of an appropriate combination of substrate and superstrate layers can improve the radiation performance by eliminating surface wave excitation. In monolithic array applications, where the individual antennas are fed by extensive feeding networks, an improvement in the radiation efficiency of the antennas will increase parasitic

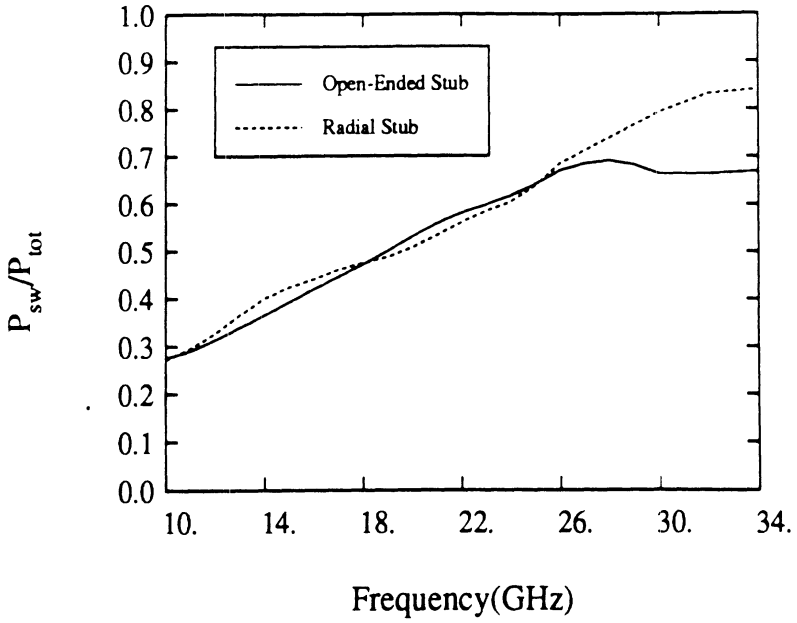

Figure 5.11: Percentage of Surface Wave Loss ($P_{tot} = P_{sw} + P_{sp}$) from open-ended and radial stubs ($\epsilon_r = 12, h = 25mil, W = 10mil$)

radiation. Consequently, the techniques for surface wave suppression have to be re-evaluated.

In this section, discontinuities on substrate/superstrate and two-layer substrate combinations made of duroid ($\epsilon_r = 2.2$) and GaAs ($\epsilon_r = 13$) are considered. Specifically, total radiation losses, and the percentages of surface wave and space wave power are evaluated as functions of the frequency and are compared to the single-layer substrate case.

Substrate-Superstrate Configuration

Figure 5.15 shows the total radiated power as a function of frequency for a right-angle bend printed on a 40 mil duroid substrate with and without a 16 mil GaAs cover. The comparison shows clearly the effects of the superstrate from 10 GHz to

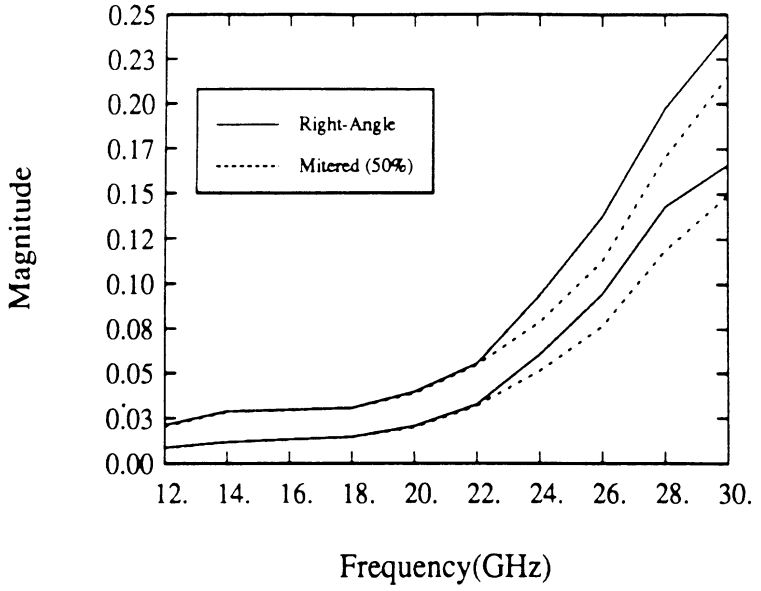

gure 5.12: Total Radiation Loss of Mitered and Right-angle Bend ($\epsilon_r = 12, h = 25mil, W = 15mil$)

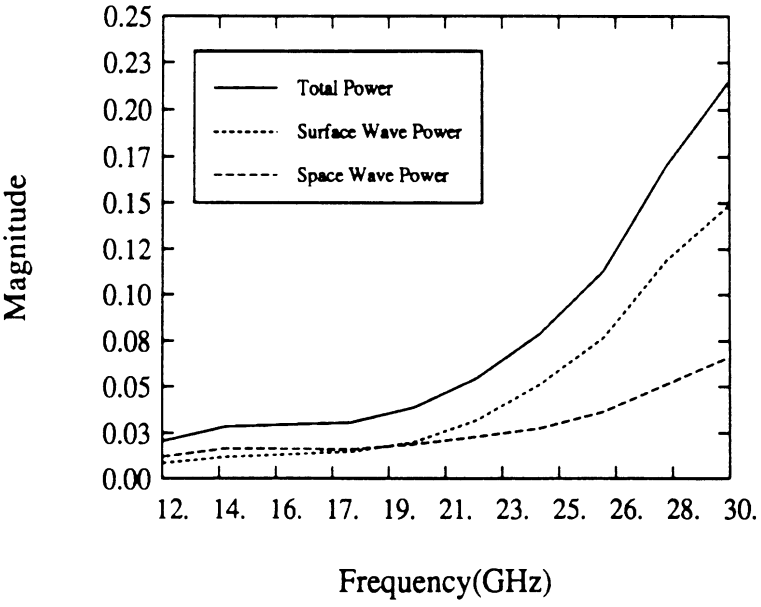

Figure 5.13: Radiation Loss of Mitered Bend ($\epsilon_r = 12, h = 25mil, W = 15mil$)

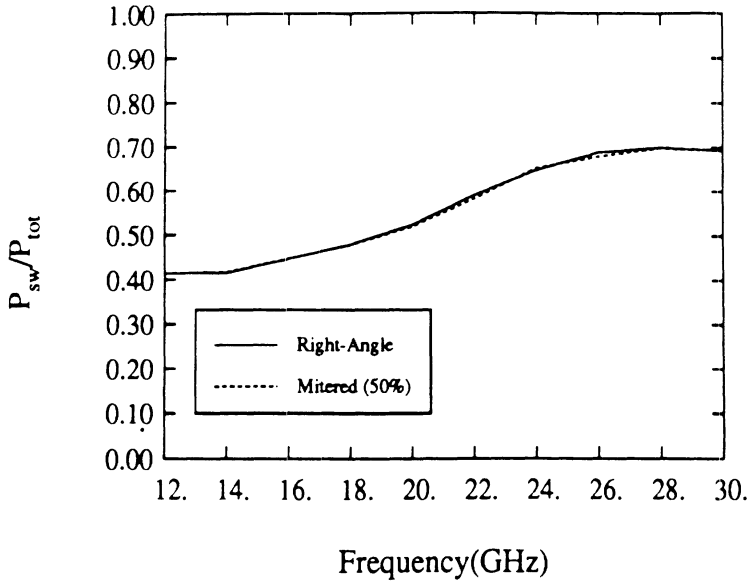

ure 5.14: Percentage of Surface Wave Loss ($P_{tot} = P_{sw} + P_{sp}$) From Mitered and Right-angle Bends ($\epsilon_r = 12, h = 25mil, W = 15mil$)

GHz. In the lower half of the frequency band, the superstrate tends to reduce es slightly. However, at higher frequencies, the total radiated power is increased he presence of the cover. As Figures 5.16 and 5.17 indicate, this excess radiated er comes from the enhancement of space wave radiation which is very desirable in ennas. On the other hand, in monolithic arrays printed on single layer dielectric strate a careful design of the feeding network could provide parasitic radiation ıy dBs lower than the primary radiation from the array. The replacement of the le layer by a substrate/superstrate configuration for array efficiency improvement d increase the power radiated by all the discontinuities included in the feeding cture, and as a result, the level of the total parasitic radiation could become cceptably high and could deteriorate the array pattern substantially. Therefore, adeoff exists in the design of multilayer structures, and reliable CAD models are

required for correct design.

Two-Layer substarte

In this case, two different comparisons are performed. At first the total power radiated by a right-angle bend printed on a 56 mil duroid is compared to the same bend printed on 40mil-duroid/16mil-GaAs substrate and shows a 20% increase at the upper end of the frequency band mainly coming from the enhancement of the space wave radiation (see Figures 5.18 and 5.19). Much higher radiated power is observed when the geometry of the single layer bend is modified to preserve the $100\Omega m$ input/output-port characteristic impedance observed in the two-layer case. The excess loss observed in this case is due to the effects of electrically thick substrates which have been reported in [20].

In both of the above reported cases, the frequency range was chosen so that only one mode is excited in the substrate. Furthermore, the presence of the superstrate or of a second layer with a higher dielectric constant tends to reduce the power of the excited surface wave and increase the power radiated into space waves. These effects have to be taken into account when techniques for enhancement of the radiation efficiency are applied in arrays fed by extensive feeding networks.

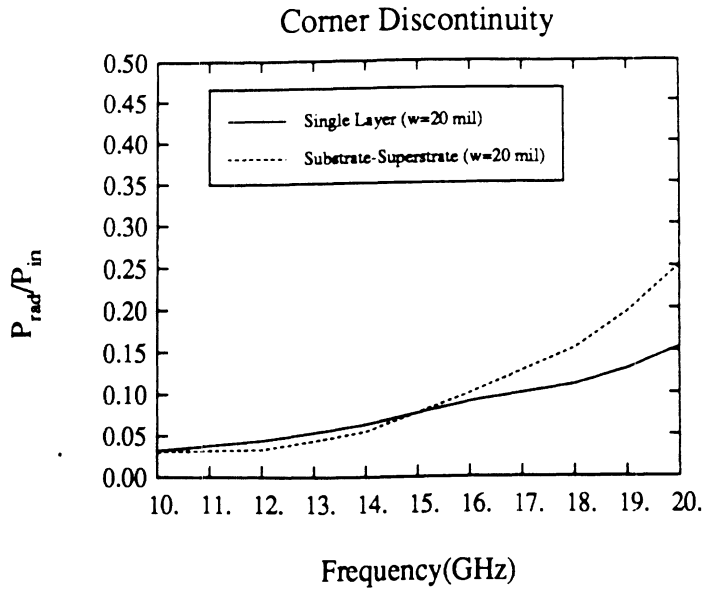

Figure 5.15: Total Radiation Loss for a microstrip corner discontinuity with ($h_1 = 16mil, h_2 = 40mil, \epsilon_{r1} = 13, \epsilon_{r2} = 2$) and without a superstrate($h_1 = 40mil, \epsilon_{r1} = 2$)

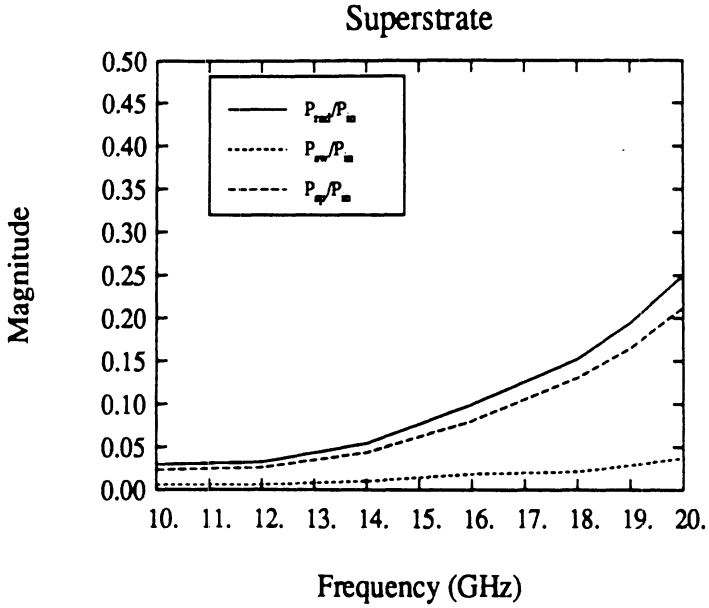

Figure 5.16: Radiation Loss for a microstrip corner discontinuity with a superstrate ($h_1 = 16mil, h_2 = 40mil, \epsilon_{r1} = 13, \epsilon_{r2} = 2$)

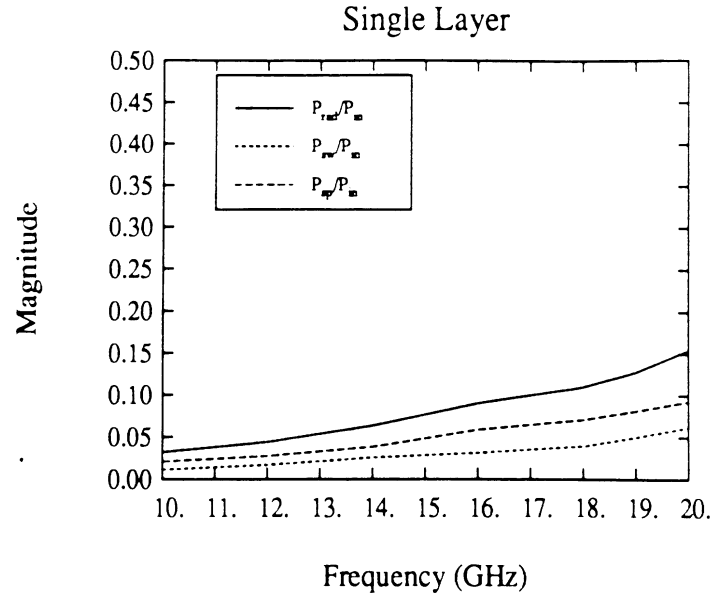

Figure 5.17: Radiation Loss for a microstrip corner discontinuity on a single layer($h_1 = 40mil, \epsilon_{r1} = 2$)

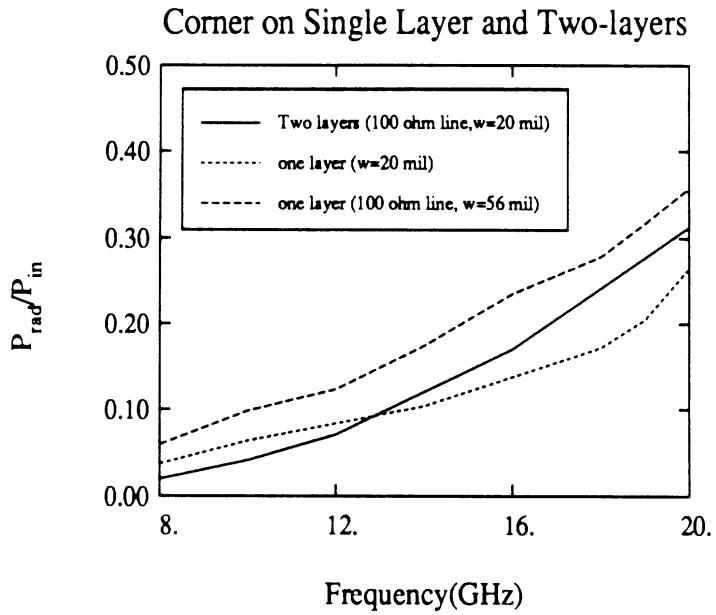

Figure 5.18: Total Radiation Loss for a microstrip corner discontinuity with a two-layer substrate ($h_1 = 16mil, h_2 = 40mil, \epsilon_{r1} = 13, \epsilon_{r2} = 2$) and with a single layer substrate($h_1 = 56mil, \epsilon_{r1} = 2$)

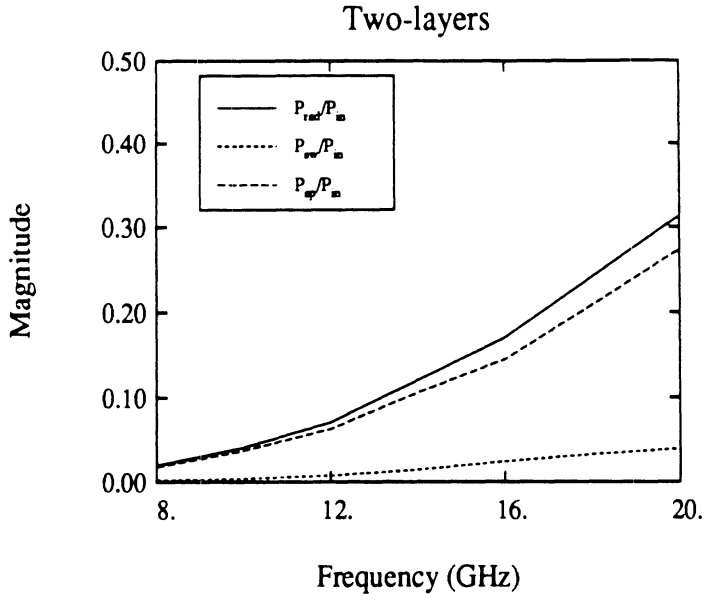

Figure 5.19: Radiation Loss for a microstrip corner discontinuity with a two-layer substrate ($h_1 = 16mil, h_2 = 40mil, \epsilon_{r1} = 13, \epsilon_{r2} = 2$)

CHAPTER VI

CONCLUSIONS

A study of open microstrip discontinuities by the Space Domain Integral Equation (SDIE) Technique has been presented. The SDIE approach involves the application of the method of moments to the electric field integral equation in the space domain. The integral equation contains the Green's function appropriate for the open microstrip geometry, which was formulated such that substrate structures involving multiple dielectric layers and/or dielectric superstrates could be analyzed. Results inherently include radiation loss, and conductor loss is included by the replacement of the conducting strips with surface impedance boundaries. Radiation loss results from two distinct mechanisms, space wave or surface wave excitation. Space waves refer to the modes radiated into the semi-infinite region above the dielectric; and surface waves are modes propagating in the grounded dielectric substrate. A saddle point analysis was used to separate the total power into these two types. Extensive results illustrate important and interesting aspects concerning the high frequency behavior of microstrip discontinuities. Numerical results were validated by experimental data. In the following sections conclusions of the study are presented.

6.1 Numerical Considerations

The application of method of moments to the electric field integral equation produced expressions involving complicated integro-differential operators. In particular, the elements of the impedance matrix of section 2.4.1 contained a semi-infinite Sommerfeld integral and quadruple spatial integrals. A numerical evaluation of these integrals would result in unacceptable numerical errors and unfeasible computer costs. Therefore, a combination of analytical and numerical methods was employed. For example, the evaluation of the semi-infinite Sommerfeld integral, performed along the positive real axis in the complex plane, was divided into two regions: i) From [0-A] and ii) from [A-∞). The parameter A was chosen so that the integrand could be approximated by an asymptotic expression in the second interval, allowing a closed form evaluation to be done. Over the first interval, a numerical evaluation was carried out with fixed point gaussian quadrature.

The quadruple spatial integrals were also computed by a combination of analytical and numerical techniques. Through an analytical process involving integration by parts, taylor expansions, and trigonometric identities, the four integrals were represented by convergent series. These series could be computed far more quickly and accurately than a full numerical integration.

The analytical and numerical techniques mentioned above were implemented in powerful computer codes capable of the analysis of advanced open microstrip structures previously uninvestigated by fullwave techniques. For instance, a meander line filter structure whose performance was influenced by strong electromagnetic coupling and radiation losses was studied. For this structure, existing CAD software is completely inadequate and fullwave analysis is needed.

Another important aspect of the analysis, discussed in section 3.4, is that of umerical convergence of network parameters. Two types of convergence were inves-gated: i) convergence pertaining to the choice of the asymptotic parameter A, and) convergence relating to the choice of subsection size. The choice of both of these arameters has implications on accuracy and CPU time. In the case of the former, ccellent convergence was shown for a wide range of the parameter A. As mentioned, naller values of A result in shorter execution times. Regarding the convergence lating to the subsection size, results were found to be very stable and accurate for scretizations greater than 30 subsections/guide wavelength. Results from sparser scretizations result in less accuracy, but may be acceptable in some applications. urves in section 3.4.2 may be used to determine the level of discretization required r a specific application.

.2 Conclusions From Numerical Results

Numerical results were presented in Chapters 4 and 5. In Chapter 4, microstrip ements were treated as circuit elements and characterized by network parameters, ıile in Chapter 5, their radiation properties were studied. Experimental verifica-on demonstrated that the SDIE technique is an extremely accurate method for aracterizing microstrip structures. From the results several conclusions may be ade:

2.1 Circuit Performance

icrostrip Tuning Stubs

Results indicate that open microstrip tuning stubs may radiate 20-30 percent of eir input power when printed on a high density substrate (eg. alumina,GaAs) of

practical thickness. The total radiation loss is influenced by the substrate thickness and the width of the stub. In addition, when stubs are in a balanced configuration (Two stubs, one on either side of the line forming a cross) they tend to radiate less than a single stub because of phase cancellation in the radiated fields.

Meander Lines

Two microwave applications of meander lines were investigated. In the first, meander lines suitable for use as antenna array traveling wave feeds were modeled. It was found that the phase delay for a long meander line could be accurately determined from the phase delay of a single period. In addition, meander lines experienced radiation and conductor losses which increased with increasing line length and frequency.

The second meander line application investigated was filtering. Since meander lines are periodic structures they exhibit stop and passbands. An example was given which exhibited a pencil thin passband. This element had high radiation loss, which must be compensated for if it were to be incorporated into a larger design.

Step Approximation

Experimental results showed that the simulation of irregular structures by the step approximation was accurate. The approximation was used in the analysis of a mitered bend discontinuity and a radial tuning stub. The mitered bend demonstrated superior performance to its right-angle counterpart, having lower return and radiation loss. The radial stub showed improved bandwidth over the rectangular stub and a moderate improvement in radiation loss.

Multi-port junctions

A general procedure, discussed in section 2.5, was developed for extracting [S]-parameters from a multi-port microstrip network, and was successfully employed to characterize three-port and four port junctions. It was found that junction parasitics were greater between ports at right-angles, and that this was not adequately modeled with existing CAD. In addition, it was also found that the radiation loss of a right-angle, T-, and cross junction with the same material dimensions were similar; nonetheless, the cross junction radiated less because of its symmetrical nature. Radiation loss from microstrip junctions increased steadily with frequency until the excitation of higher order surface wave modes. In general, junctions experienced lower radiation losses than resonant tuning stubs.

3.2.2 Radiation Properties

A saddle point analysis was applied to study the radiation properties of open microstrip discontinuities in Chapter 6. The technique utilized microstrip current distributions obtained with the method of moments. Total radiation loss was separated into the individual contributions of space wave and surface wave radiation, and the direction of surface wave propagation within the substrate was shown. These new results represent a substantial contribution to the understanding of the radiation properties of open microstrip discontinuities.

Surface Wave Excitation

It was shown that on high density substrates of practical electric thickness, radiation loss is dominated by the TM_0 surface wave at high frequencies. This mode is excited along the longitudinal axis for the open-ended stub and bend discontinuities,

and may have a narrow beamwidth.

An example of a mitered bend was shown to radiate less power than its right-angle counterpart. Such a minor topology change had a significant influence on total radiated power, without having a more significant impact on either of the two types. This was reflected in an equal percentage reduction in both space and surface wave radiation.

Multi-layered Substrates and Superstrates

It is well known that substrate composition plays a major role in microstrip radiation losses. Examples of microstrip bends printed on two-layered substrates indicated that combinations having a low permittivity layer over a high permittivity layer radiated far more than the opposite configuration.

It was found that a superstrate, often used for protection or gain enhancement of antenna elements, may increase the loss of the microstrip feed network considerably. This would result in lower overall gain. Therefore, a tradeoff exists between the enhancement of radiation from the antennas and the undesirable radiation in the feed network.

A comparison between a corner discontinuity on a single layer of duroid, and on a two layer structure (GaAs/duroid) having the same total thickness, showed that the radiation loss was comparable when the conducting strips were of the same width. However, it was found that the loss was influenced by the strip width. Specifically, when the width in the single layer case was widened to create the same characteristic impedance as the two layer case, the loss was substantially higher.

APPENDICES

APPENDIX A

Green's Function

This appendix contains the functions included in the expression of the Green's function in equations (2.18) and (2.19) The functions are given below for three different substrate configurations.

- *Substrate-Superstrate Configuration*

  The functions for the substrate-superstrate geometry of Figure 1(a) in the region $(0 < Z < h_1)$ are given by

$$\mathcal{N}_{\xi\xi}(\lambda) = \lambda \tag{A.1}$$

$$\mathcal{N}_{z\xi}(\lambda) = \frac{j}{u_1} \tag{A.2}$$

$$\mathcal{Z}_{\xi\xi} = u_1 \cosh\left[ju_1(z-h_1)\right] - u_0 \sinh\left[ju_1(z-h_1)\right] \tag{A.3}$$

$$\begin{aligned}\mathcal{Z}_{z\xi} &= \left[u_1^2 u_2 f_1(\lambda) - u_0^3 f_2(\lambda)\right] \cosh\left[ju_1(z-h_1)\right] \\ &+ u_1 u_0 \left[u_0 f_2(\lambda) - \epsilon_{r1} u_2 f_1(\lambda)\right] \sinh\left([ju_1(z-h_1)\right]\end{aligned} \tag{A.4}$$

  with $u_i = \sqrt{k_i^2 - \lambda^2}$. The expressions $f_1(\lambda)$ and $f_2(\lambda)$ are the characterisic equations for surface wave modes given by

$$f_1(\lambda) = u_0 \left[u_1 \cosh\left(ju_1 h_1\right) + u_2 \coth\left(ju_2 h_2\right) \sinh\left(ju_1 h_1\right)\right]$$

$$+ \quad u_1 \left[u_1 \sinh\left(ju_1h_1\right) + u_2 \coth\left(ju_2h_2\right) \cosh\left(ju_1h_1\right) \right] \tag{A.5}$$

$$f_2(\lambda) = u_1 \left[\epsilon_{r2} u_1 \sinh\left(ju_1h_1\right) \coth\left(ju_2h_2\right) + \epsilon_{r1} u_2 \cosh\left(ju_1h_1\right) \right]$$

$$+ \quad \epsilon_{r1} u_0 \left[\epsilon_{r2} u_1 \coth\left(ju_2h_2\right) \cosh\left(ju_2h_2\right) + \epsilon_{r1} u_2 \sinh\left(ju_1h_1\right) \right] \tag{A.6}$$

- *Two-Layer Substrate*

The functions for the two-layer case in Figure 1(b) for the region ($Z > 0$) are given by

$$\mathcal{N}_{\xi\xi}(\lambda) = \left[u_1 \cosh\left(ju_1h_1\right) + u_2 \sinh\left(ju_1h_1\right) \coth\left(ju_2h_2\right) \right] \lambda \tag{A.7}$$

$$\mathcal{N}_{z\xi}(\lambda) = j\epsilon_r u_0^2 \left[\epsilon_{r2} u_1 \cosh\left(ju_1h_1\right) \coth\left(ju_2h_2\right) + \epsilon_{r1} u_2 \sinh\left(ju_1h_1\right) \right]$$

$$\left[u_1 \cosh\left(ju_1h_1\right) + u_2 \coth\left(u_2h_2\right) \sinh\left(ju_1h_1\right) \right]$$

$$- \quad ju_1^2 \left[u_1 \sinh\left(ju_1h_1\right) + u_2 \coth\left(ju_2h_2\right) \cosh\left(ju_1h_1\right) \right] \tag{A.8}$$

$$\left[\epsilon_{r2} u_1 \coth\left(ju_2h_2\right) \sinh\left(ju_2h_2\right) + \epsilon_{r1} u_2 \cosh\left(ju_1h_1\right) \right] \tag{A.9}$$

$$\mathcal{Z}_{\xi\xi} = \mathcal{Z}_{z\xi} = e^{-ju_0 z} \tag{A.10}$$

- *Single-Layer Substrate*

The expressions for the single layer case may be obtained from equations (57)-(60). After some simplification they can be written as

$$\mathcal{N}_{\xi\xi}(\lambda) = \sinh\left(ju_1h_1\right)\lambda \tag{A.11}$$

$$\mathcal{N}_{z\xi}(\lambda) = \left[(1 - \epsilon_r) \sinh ju_1h \cosh ju_1h \right] \lambda^2 \tag{A.12}$$

$$f_1(\lambda) = u_0 \sinh ju_1h + u_1 \cosh ju_1h \tag{A.13}$$

$$f_2(\lambda) = \epsilon_r u_0 \cosh ju_1h + u_1 \sinh ju_1h \tag{A.14}$$

APPENDIX B

Single Layer Green's Function

The components of the space domain green's function for a single layer are given by

$$G_{xx} = G_{yy} = -\frac{\omega\mu_0}{2\pi k_0^2}\int_0^\infty J_0(\lambda\rho)\frac{\sinh ju_1h}{f_1(\lambda)}e^{-ju_0z}\lambda d\lambda \quad Z > 0 \tag{B.1}$$

$$\begin{aligned} G_{zx} &= \tan(\phi)G_{zy} \\ &= -\frac{\omega\mu_0}{2\pi k_0^2}(1-\epsilon_r)\cos\phi\int_0^\infty J_1(\lambda\rho)e^{-ju_0z}\frac{\sinh ju_1h\cosh ju_1h}{f_1(\lambda)f_2(\lambda)}\lambda^2 d\lambda \end{aligned} \tag{B.2}$$

$$G_{xx} = G_{yy} = -\frac{j\omega\mu_0}{2\pi k^2}\int_0^\infty J_0(\lambda\rho)\frac{\sinh u(z+h)}{f_1(\lambda)}\lambda d\lambda \quad Z < 0 \tag{B.3}$$

$$\begin{aligned} G_{zx} &= \tan(\phi)G_{zy} \\ &= -\frac{j\omega\mu_0}{2\pi k^2}(1-\epsilon_r)\cos\phi\int_0^\infty J_1(\lambda\rho)\frac{\sinh ju_1h\cosh u(z+h)}{f_1(\lambda)f_2(\lambda)}\lambda^2 d\lambda \end{aligned} \tag{B.4}$$

with $\rho = \sqrt{(x-x')^2+(y-y')^2}$, $u_0 = \sqrt{\lambda^2 - k_0^2}$, and $u_1 = \sqrt{\lambda^2 - k_1^2}$. The equations $f_1(\lambda)$ and $f_2(\lambda)$ represent characterisic equations for surface wave modes given by

$$f_1(\lambda) = u_0\sinh ju_1h + u\cosh ju_1h \tag{B.5}$$

$$f_2(\lambda) = \epsilon_r u_0\cosh ju_1h + u\sinh ju_1h \tag{B.6}$$

where in the above, ϵ_{r1} is the relative dielectric constant, and h is the thickness of the substrate. These components of the Green's function may be tranformed

from semi-infinite integration along the positive real axis to infinite integrations by the relationships

$$J_0(\lambda\rho) = \frac{1}{2}[H_0^{(1)}(\lambda\rho) + H_0^{(2)}(\lambda\rho)] \tag{B.7}$$

$$J_1(\lambda\rho) = \frac{1}{2}[H_1^{(1)}(\lambda\rho) + H_1^{(2)}(\lambda\rho)] \tag{B.8}$$

$$H_0^{(2)}(\lambda\rho) = -H_0^{(1)}(-\lambda\rho) \tag{B.9}$$

$$H_1^{(2)}(\lambda\rho) = H_1^{(1)}(-\lambda\rho) \tag{B.10}$$

Resulting in the expressions in the free-space region ($z > 0$)

$$G_{xx} = G_{yy} = -\frac{j\omega\mu_o}{4\pi k_0^2}\int_{-\infty}^{\infty} H_0^{(1)}(\lambda\rho)e^{-u_0 z}\frac{\sinh ju_1 h}{f_1(\lambda)}\lambda d\lambda \tag{B.11}$$

$$\begin{aligned} G_{zx} &= \tan\phi G_{zy} \\ &= -\frac{j\omega\mu_o}{4\pi k_0^2}(1-\epsilon_r)\cos\phi\int_{-\infty}^{\infty} H_1^{(1)}(\lambda\rho)e^{-u_0 z}\frac{\sinh ju_1 h\cosh ju_1 h}{f_1(\lambda)f_2(\lambda)}\lambda^2 d\lambda \end{aligned} \tag{B.12}$$

APPENDIX C

Surface Wave Fields

)urface wave fields resulting from application of Cauchy's theroem.

$$E_z = \frac{k_0\omega\mu_0}{2}\sqrt{\frac{2j}{\pi\rho k_0}}\cos(\phi)\sum_{n=0}^{NTM}\frac{\sqrt{\epsilon_r - cosh^2(\nu_n)}}{\sqrt{\cosh\nu_n}}\frac{\cosh^2(\nu_n)\sinh(\nu_n)}{[f_2'(\alpha,h)]|_{\frac{\pi}{2}+j\nu_n}} \quad \text{(C.1)}$$
$$\sin[k_0\sqrt{\epsilon_r - cosh^2(\nu_n)}h]e^{-jk_0\rho\cosh(\nu_n)}e^{-k_0 z\sinh(\nu_n)} \qquad Z > 0$$

$$H_\phi = -\frac{k_0^2}{2}\sqrt{\frac{2j}{\pi\rho k_0}}\cos(\phi)\sum_{n=0}^{NTM}\frac{\sqrt{\epsilon_r - cosh^2(\nu_n)}}{\sqrt{\cosh\nu_n}}\frac{\cosh(\nu_n)\sinh(\nu_n)}{[f_2'(\alpha,h)]|_{\frac{\pi}{2}+j\nu_n}} \quad \text{(C.2)}$$
$$\sin[k_0\sqrt{\epsilon_r - cosh^2(\nu_n)}h]e^{-jk_0\rho\cosh(\nu_n)}e^{-k_0 z\sinh(\nu_n)} \qquad Z > 0$$

$$E_z = \frac{k_0\omega\mu_0}{2}\sqrt{\frac{2j}{\pi\rho k_0}}\cos(\phi)\sum_{n=0}^{NTM}\frac{\cosh^2(\nu_n)\sinh^2(\nu_n)}{\sqrt{\cosh\nu_n}}e^{-jk_0\rho\cosh(\nu_n)} \quad \text{(C.3)}$$
$$\frac{\cos[k_0\sqrt{\epsilon_r - cosh^2(\nu_n)}(z+h)]}{[f_2'(\alpha,h)]|_{\frac{\pi}{2}+j\nu_n}} \qquad Z < 0$$

$$H_\phi = -\frac{\epsilon_{r1}k_0^2}{2}\sqrt{\frac{2j}{\pi\rho k_0}}\cos(\phi)\sum_{n=0}^{NTM}\frac{\cosh(\nu_n)\sinh^2(\nu_n)}{\sqrt{\cosh\nu_n}}e^{-jk_0\rho\cosh(\nu_n)} \quad \text{(C.4)}$$
$$\frac{\cos[k_0\sqrt{\epsilon_r - cosh^2(\nu_n)}(z+h)]}{[f_2'(\alpha,h)]|_{\frac{\pi}{2}+j\nu_n}} \qquad Z < 0$$

nd for the TE case

$$H_z = -\frac{k_0^2}{2}\sqrt{\frac{2j}{\pi\rho k_0}}\sin(\phi)\sum_{m=0}^{NTE}\frac{cosh^2(\nu_m)sinh(\nu_m)}{\sqrt{\cosh\nu_m}[f_1'(\alpha,h)]|_{\frac{\pi}{2}+j\nu_m}} \quad \text{(C.5)}$$
$$\sin[k_0\sqrt{\epsilon_r - cosh^2(\nu_n)}h]e^{-jk_0\rho\cosh(\nu_m)}e^{-k_0 z\sinh(\nu_m)} \qquad Z > 0$$

$$E_\phi = -\frac{k_0\omega\mu_0}{2}\sqrt{\frac{2j}{\pi\rho k_0}}\sin(\phi)\sum_{m=0}^{NTE}\frac{cosh(\nu_m)sinh(\nu_m)}{\sqrt{\cosh\nu_m}[f_1'(\alpha,h)]|_{\frac{\pi}{2}+j\nu_m}} \quad \text{(C.6)}$$

$$\sin\left[k_0\sqrt{\epsilon_r - cosh^2(\nu_n)}h\right]\epsilon^{-jk_0\rho\cosh(\nu_m)}\epsilon^{-k_0 z\sinh(\nu_m)}$$

$$H_z = -\frac{k_0^2}{2}\sqrt{\frac{2j}{\pi\rho k_0}}\sin(\phi)\sum_{m=0}^{NTE}\frac{cosh^2(\nu_m)sinh(\nu_m)}{\sqrt{\cosh\nu_m}[f_1'(\alpha,h)]|_{\frac{\pi}{2}+j\nu_m}} \qquad (C.7)$$

$$\epsilon^{-jk_0\rho\cosh(\nu_m)}\sin\left[k_0\sqrt{\epsilon_r - cosh^2(\nu_n)}(z+h)\right] \qquad Z<0$$

$$E_\phi = -\frac{k_0\omega\mu_0}{2}\sqrt{\frac{2j}{\pi\rho k_0}}\sin(\phi)\sum_{m=0}^{NTE}\frac{cosh(\nu_m)sinh(\nu_m)}{\sqrt{\cosh\nu_m}[f_1'(\alpha,h)]|_{\frac{\pi}{2}+j\nu_m}} \qquad (C.8)$$

$$\epsilon^{-jk_0\rho\cosh(\nu_m)}\sin\left[k_0\sqrt{\epsilon_r - cosh^2(\nu_n)}(z+h)\right] \qquad Z<0$$

APPENDIX D

Evaluation of Quadruple Spatial Integrals

The quadruple integrals in equation (2.40) for direct coupled x-x interactions can be written

$$\langle f_{n_x}(x')g_{m_x}(y'),\ J_0(\lambda\rho),\ f_{\nu_x}(x)g_{\mu_x}(y)\rangle \tag{D.1}$$
$$= \int\int_{S'} dx'dy' \int\int_S dxdy\,[f_{n_x}(x')g_{m_x}(y')\,J_0(\lambda\rho)\,f_{\nu_x}(x)g_{\mu_x}(y)]$$

$$\langle f_{n_x}(x')g_{m_x}(y'),\ \frac{\partial^2}{\partial x^2}J_0(\lambda\rho),\ f_{\nu_x}(x)g_{\mu_x}(y)\rangle \tag{D.2}$$
$$= \int\int_{S'} dx'dy' \int\int_S dxdy\left[f_{n_x}(x')g_{m_x}(y')\,\frac{\partial^2}{\partial x^2}J_0(\lambda\rho)\,f_{\nu_x}(x)g_{\mu_x}(y)\right]$$

and for cross coupled x-y terms

$$\langle f_{n_x}(x')g_{m_x}(y'),\ \frac{\partial^2}{\partial x\partial y}J_0(\lambda\rho),\ f_{\nu_y}(x)g_{\mu_y}(y)\rangle \tag{D.3}$$
$$= \int\int_{S'} dx'dy' \int\int_S dxdy\left[f_{n_x}(x')g_{m_x}(y')\,\frac{\partial^2}{\partial x\partial y}J_0(\lambda\rho)\,f_{\nu_y}(y)g_{\mu_y}(x)\right]$$

Employing the integral representation for the first order bessel function in equations (31)-(32), the above may be simplified to the expressions

$$\langle f_{n_x}(x')g_{m_x}(y'),\ J_0(\lambda\rho),\ f_{\nu_x}(x)g_{\mu_x}(y)\rangle$$
$$= \frac{1}{2\pi}\int_{-\pi}^{\pi} e^{j\lambda(x_{\nu_x}-x'_{n_x})\cos(\phi)}e^{j\lambda(y_{\mu_x}-y'_{m_x})\sin(\phi)}$$

$$(\mathcal{R}(\lambda\cos(\phi)))^2\mathcal{U}(\lambda\sin(\phi))\mathcal{U}(-\lambda\sin(\phi))d\phi \tag{D.4}$$

$$\begin{aligned}
&\langle f_{n_x}(x')g_{m_x}(y'),\ \frac{\partial^2}{\partial x^2}J_0(\lambda\rho),\ f_{\nu_x}(x)g_{\mu_x}(y)\rangle \\
&= \frac{1}{2\pi}\int_{-\pi}^{\pi}(j\lambda\cos\phi)^2 e^{j\lambda(x_{\nu_x}-x'_{n_x})\cos(\phi)}e^{j\lambda(y_{\mu_x}-y'_{m_x})\sin(\phi)} \\
&\quad \mathcal{R}(\lambda\cos(\phi))^2\mathcal{U}(\lambda\sin(\phi))\mathcal{U}(-\lambda\sin(\phi))d\phi
\end{aligned} \tag{D.5}$$

$$\begin{aligned}
&\langle f_{n_x}(x')g_{m_x}(y'),\ \frac{\partial^2}{\partial x\partial y}J_0(\lambda\rho),\ f_{\nu_y}(y)g_{\mu_y}(x)\rangle \\
&= \frac{1}{2\pi}\int_{-\pi}^{\pi}(j\lambda\sin\phi)(j\lambda\cos\phi)e^{j\lambda(x_{\mu_y}-x'_{n_x})\cos(\phi)}e^{j\lambda(y_{\nu_y}-y'_{m_x})\sin(\phi)} \\
&\quad \mathcal{R}(\lambda\cos(\phi))\mathcal{R}(\lambda\sin(\phi))\mathcal{U}(\lambda\cos(\phi))\mathcal{U}(-\lambda\sin(\phi))d\phi
\end{aligned} \tag{D.6}$$

The quantaties $\mathcal{R}$ and $\mathcal{B}$ are convergent series having the form

$$\mathcal{R}(\lambda\cos(\phi)) = \sum_{k=0}^{\infty}A_{2k}(\lambda\cos(\phi))^{2k} \tag{D.7}$$

$$\mathcal{U}(\lambda\cos(\phi)) = \sum_{l=0}^{\infty}B_l(\lambda\cos(\phi))^l \tag{D.8}$$

where

$$A_{2k} = \frac{2}{k^{2k+1}}\left([1-\cos(kl_x)] + \sum_{\mu=1}^{k}(-1)^{\mu}\frac{(kl_x)^{2\mu}}{(2\mu)^2}\right) \tag{D.9}$$

$$B_{2n} = (-1)^n(l_x)^{2n} \tag{D.10}$$

$$B_{2n+1} = j(-1)^n(l_x)^{2n+1}.$$

considering the integral representation for the zero'th order Bessel function these expressions can be re-written as a summation of derivatives of the zero'th order Bessel function appearing in the main text (equations (3.8)-(3.9)).

BIBLIOGRAPHY

BIBLIOGRAPHY

[1] M. Maeda, "Analysis of Gap in Microstrip Transmission Lines", *IEEE Trans. Microwave Theory Tech.*, Vol. MTT-20, pp.390-396, Jun. 1972.

[2] P. Benedek and P. Silvester, "Equivalent Capacitance of Microstrip Gaps and Steps", *IEEE Trans. Microwave Theory Tech.*, Vol. MTT-20, pp.729-733, Nov. 1972.

[3] P. Silvester and P. Benedek, "Equivalent Capacitance of Microstrip Open Circuits," *IEEE Trans. Microwave Theory Tech.*, Vol. MTT-20, pp. 511-516, Aug. 1972.

[4] P. Silvester and P. Benedek, "Equivalent discontinuities capacitances for Right-Angle Bends, T-junctions, and Crossings," *IEEE Trans. Microwave Theory Tech.*, Vol. MTT-21, pp. 341-346, May 1973.

[5] R. Horton, "The Electrical Characterization of a Right-Angle Bends in Microstrip Line," *IEEE Trans. Microwave Theory Tech.*, Vol. MTT-21, pp.427-429, Jun. 1973.

[6] C. Gupta, A. Gopinath, "Equivalent circuit capacitance for microstrip change in width", it IEEE Trans. Microwave Theory Tech., Vol. MTT-25, pp.819-821, Oct. 1977.

[7] T. Itoh,"Analysis of Microstrip resonators", *IEEE Trans. Microwave Theory Tech.*, Vol. MTT-22, pp.946-952, Nov. 1974.

[8] I. Wolf, G. Kompa, and R. Mehran, "Calculation Method For Microstrip Discontinuities and T-Junctions," *Electron. Lett.*, Vol. 8, 1972.

[9] W. Menzel and I. Wolf,"A Method For Calculating the frequency Dependent Properties of Microstrip Discontinuities," *IEEE Trans. Microwave Theory Tech.*, Vol. MTT-25, pp. 107-112, Feb. 1977.

[10] M. Kirschning, R.H. Jansen, and H.L. Koster, "Measurement and Computer-Aided Modeling of Microstrip Discontinuities by an Improved Resonator Method", 1983 "IEEE MTT-S International Microwave Symposium Digest", May, 1983.

[11] R. H. Jansen, "The Spectral Domain Approach for Microwave Integrated Circuits," *IEEE Trans. Microwave Theory Tech.*, Vol. MTT-33, pp.1043-1056, Oct. 1985.

[12] J. C. Rautio and R.F. Harrington. "An electromagnetic timeharmonic analysis of shielded microstrip circuits," *IEEE Trans. Microwave Theory Tech.*, Vol. MTT-35, pp. 726-730, Aug. 1987.

[13] L. P. Dunleavy and P. B. Katehi. "A Generalized Method for Analyzing Shielded Thin Microstrip Discontinuities ," *IEEE Trans. Microwave Theory Tech.*, Vol. MTT-36, pp.178-1766, Dec. 1988.

[14] L. P. Dunleavy and P.B. Katehi, "Shielding Effects in Microstrip Discontinuities," *IEEE Trans. Microwave Theory Tech.*, Vol. MTT-36, pp.1767-1774, Dec. 1988.

[15] R. H. Jansen, "Full-wave Theory Based Development of mm-Wave Circuit Models for Microstrip Open End, Ga, Step, Bend, and Tee," *IEEE Microwave Symposium Digest*, pp. 779-782, June 1989.

[16] C.J. Railton and T. Rozzi, "Complex Modes in Boxed Microstrip," *IEEE Trans. Microwave Theory Tech.*, Vol. MTT-36, pp. 865-874, May 88.

[17] W. Wertgen, and R. H. Jansen, "Novel Green's Function Database Technique For Efficient Full-Wave analysis of Complex Irregular (M)MIC-Structures", European Microwave Conference Proceedings, September 1989, pp.199-204.

[18] W. Wertgen, and R. H. Jansen, "Efficient Direct and Iterative Electrodynamic Analysis of Geometrically Complex IrregularMIC and MMIC-Structures", International Journal of Numerical Modelling, September 1989, pp.153-186.

[19] P.B. Katehi and N. G. Alexopoulos, "On the Effect of Substrate Thickness and Permittivity and Permittivity On Printed Circuit Dipole performance," *IEEE Transactions on Antennas and Propagation*, Vol AP-31, pp. 34-38, Jan. 1983.

[20] N. G. Alexopoulos, P.B. Katehi, and D. Rutledge, "Substrate Optimization for Integrated Circuit Applications," *IEEE Trans. Microwave Theory Tech.*, Vol. MTT-31, pp. 550-557, July, 1983.

[21] P.B. Katehi and N. G. Alexopoulos, "Frequency-Dependent Characteristics of Microstrip Discontinuities in Millimeter-Wave Integrated Circuits",*IEEE Trans. Microwave Theory Tech.*, Vol. MTT-33, Oct. 85, pp. 1029-1035.

[22] J. R. Mosig, "Arbitrarily shaped microstrip structures and their analysis with a mixed potential integral equation," *IEEE Trans. Microwave Theory Tech.*, Vol. MTT-36, pp. 314-323, Feb. 1988.

[23] R. W. Jackson, and D. M. Pozar, "Full-Wave Analysis of Microstrip Open-End and Gap Discontinuities",*IEEE Trans. Microwave Theory Tech.*, Vol. MTT-33,Oct. 85, pp. 1036-1042.

[24] H. Yang, N. G. Alexopoulos, and D. R. Jackson, "Analysis of Microstrip Open-End and Gap Discontinuities in a Substrate-Superstrate Configu-

ration." *IEEE MTT-S Microwave Symposium Digest*, pp. 705-708, June 1988.

[25] R. Jackson, "Full-Wave Finite Element Analysis of Irregular Microstrip Discontinuities," *IEEE Trans. Microwave Theory Tech.*, Vol. MTT-37, pp. 81-89, Jan. 89.

[26] W. P. Harokopus, Jr. and P. B. Katehi, "An Accurate Characterization of Open Microstrip Discontinuities Including Radiation Losses", *IEEE Microwave Symposium Digest*, pp. 231-234, June 1989.

[27] W. P. Harokopus, Jr. and P. B. Katehi, "Characterization of Open Microstrip Discontinuities on Multilayer Substrates Including Radiation Losses", *IEEE Trans. Microwave Theory Tech.*, Vol. MTT-37, Dec. 89, pp. 1964-1972.

[28] W. P. Harokopus, Jr. and P. B. Katehi, "Electromagnetic Coupling and Radiation Loss Considerations for Open Microstrip Discontinuities," accepted for publication in *IEEE Trans. Microwave Theory Tecniques.*

[29] H. A. Wheeler, "Transmission Line Properties of a Strip on a Dielectric Sheet on a Plane," *IEEE Trans. Microwave Theory Tech.*, Vol. MTT-25, 1977, pp. 631-647.

[30] H. E. Stinehelfer, "An Accurate Calculation of Uniform Microstrip Transmission Lines," *IEEE Trans. Microwave Theory Tech.*, Vol. MTT-16, 1968, pp. 439-444.

[31] H. E. Green, "The Numerical Solution of some Important Transmission Line Problems," *IEEE Trans. Microwave Theory Tech.*, Vol. MTT-13, 1965, pp. 676-692.

[32] G. Kompa, and R. Mehran, "Planar Waveguide Model For Calculating Microstrip Components," *Electron. Lett.*, Vol. 11, 1975.

[33] W. J. Getsinger, "Microstrip Dispersion," *IEEE Trans. Microwave Theory Tech.*, Vol. MTT-21, 1973, pp. 34-39.

[34] D. G. Corr and J. B. Davis, "Computer Analysis of the Fundamental and Higher Order Modes In Single and Coupled Microstrip," *Microwave Theory Tech.*, Vol. MTT-20, 1972, pp. 669-678.

[35] D. M. Sheen, S. M. Ali, M. D. Abouzahra, and J. A. Kong, " Application of the Three-Dimensional Finite-Difference Time-Domain Method to the analysis of Planar Circuits," *IEEE Trans. Microwave Theory Tech.*, Vol. MTT-38, pp. 849-857,July. 90.

[36] T. Itoh and R. Mittra, "Spectral-Domain Approach for Calculating Dispersion Characteristics of Microstrip Lines," *IEEE Trans. Microwave Theory Tech.*, Vol. MTT-21, 1973, pp. 496-498.

[37] V.Rizzoli, "A General Approach to the Resonance Measurement of Asymmetric Microstrip Discontinuities," 1980 IEEE MTT-S Digest, pp. 422-424.

[38] M. Hines and H. Stinehelfer, "Time-Domain Oscillographic Microwave Network Analysis Using Frequency-Domain Data," *IEEE Trans. Microwave Theory Tech.*, Vol. MTT-22, March 74, pp. 276-282.

[39] H. F. Pues and V. Capelle, "Computer-Aided Experimental Characterization of Microstrip-to-Coaxial transitions," 14_{th} *European Microwave Conference*, 1984, pp. 137-144.

[40] N. R. Franzen and R. A. Speciale, "A New Procedure for System Calibration and Error Removal in Automated S-Parameter Measurements."5_{th} *European Microwave Conference*, 1975, pp. 69-73.

[41] G. Engen anf C. Hoer, "Thru-Reflect-Line: An Improved Technique for Calibrating the Six-Port Automatic Network Analyzer," *IEEE Trans. Microwave Theory Tech.*, Vol. MTT-27, Dec. 79, pp. 987-993.

[42] M. Maury, S. March, and G. Simpson, "LRL Calibration of Vector Automatic Network Analyzers," *Microwave Journal*, May 87, pp. 387-391.

[43] L. P. Dunleavy, "Discontinuity Characterization In Shielded Microstrip: A Theoretical and Experimental Study, Ph. D. Dissertation, University of Michigan, Ann Arbor Michigan, 1988.

[44] D. Brubaker, "Measure S-parameters With the TSD Technique," *Microwaves and RF*, Nov. 1985, pp. 97-102.

[45] R. E Collin, Field Theory of Guided Waves, McGraw Hill, New York, 1960.

[46] A. Sommerfeld, Partial Differential Equations in Physics, New York, N.Y., Academic Press, 1949.

[47] R.S. Elliott, "The Green's Function For Electric Dipoles Parallel To and Above or Within a Grounded Dielectric Slab", Hughes Technical Correspondence, 1978.

[48] R. F. Harrington, Field Computation By Moment Methods, Macmillan,N.Y. ,1968.

[49] T. Itoh, Numerical Techniques For Microwave and Millimeter-Wave Passive Structures, Wiley, New York, 1989, pp. 137-140.

[50] M. Drissi, V. Fouad Hanna, and J. Citerne, "Theoretical and Experimental Investigation of Open Microstrip Gap Discontinuities," *18th European Microwave Conference Proceedings*, pp. 203-208, September 1988.

[51] A.C. Cangellaris, "The Importance of Skin-Effect in Microstrip Lines at High Frequencies,"*IEEE MTT-International Symposium Digest*, pp 197-198, May 1988.

[52] T.E. van Deventer, P. B. Katehi, and A. C. Canggellaris, "An Integral Equation Method For The Evaluation of Conductor and Dielectric Losses in High Frequency Interconnects", *IEEE Trans. Microwave Theory Tech.*, pp. 1964-1971, Dec. 1989.

[53] L.B. Felsen and N. Marcuvitz. Radiation and Scattering of Waves.Prentice Hall, Englewood Cliffs, N.J. 1973.

[54] P.B. Katehi and N. G. Alexopoulos, "Real Axis Integration of sommerfeld Integrals With Applications To Printed Circuit Antennas," *J. Math. Phys.*, vol. 24(3), Mar. 1983.

[55] N. L. Vandenberg,

[56] EESOF, *Touchstone*, EESOF INC., Westlake Village, CA. 91362.

[57] L. P Dunleavy and P.B. Katehi, "Repeatability Issues for De-embedding Microstrip Discontinuity S-parameter Measurements By the TSD Technique," *Automatic RF Techniques Group (ARFTG) Digest* , June 76.

[58] L. P Dunleavy and P.B. Katehi, "Eliminate Surprises When De-embedding Microstrip Launchers," *Microwaves and RF*, August 87, pp. 117-122.

[59] R. L. Eisenhart, "A Better Microstrip Connector," *IEEE Microwave Symposium Digest*, pp. 318-320, 1978.

[60] HP Product Note 8510-8, "Applying the HP 8510B TRL calibration fir non-coaxial measurements," Oct. 1987.

[61] P.S. Hall and S.J. Vetterlein, "Microstrip Patch Array With Multiple beams", European Microwave Conference Proceedings, September 1989, pp. 343-348. *IEEE Trans. Microwave Theory Tech.*, Dec. 1989.

[62] R. E Collin, Field Theory of Guided Waves, McGraw Hill, New York, 1960.

[63] J. A. Weiss, "Dispersion and Field Analysis of a Microstrip Meander-Line Slow-Wave Structure," *IEEE Trans. Microwave Theory Tech.*, Vol. MTT-22, No. 12, pp. 1194-1201.

[64] V. Rizzoli, and A. Lipparini, "Bloch-Wave Analysis of Stripline- and Microstrip-Array Slow-Wave Structures," *IEEE Trans. Microwave Theory Tech.*, Vol. MTT-29, No. 29, pp. 143-149.

[65] W. P. Harokopus, Jr. and P. B. Katehi, "Radiation properties of microstrip discontinuities," *IEEE Ap Digest*, June 1989.

[66] W. P. Harokopus, Jr. and P. B. Katehi, "Radiation properties of microstrip discontinuities," *1990 Radio Science Meeting Program and Abstracts*, page 337, May 1990.

[67] T. S. Horng, S. C. Wu, H. Y. Yang and N. G. Alexopoulos, "A Generalized Method for the Distinction of Radiation and Surface Wave Losses in Microstrip Discontinuities," *IEEE Microwave Symposium Digest*, pp. 1055-1058, May 1990.

[68] W. P. Harokopus, Jr. and P. B. Katehi, "Radiation Losses in Microstrip Antenna Networks Printed on Multi-Layer Substrates," accepted for publication in *International Journal of Numerical Modelling.*

[69] W. P. Harokopus, Jr. and P. B. Katehi, "Surface Wave Excitation From Open Microstrip Discontinuities," accepted for publication in *IEEE Trans. Microwave Theory Tecniques*. pp. 807-814, August 1984.

[70] N.G. Alexopoulos, and D. R. Jackson, "Fundamental Superstrate (Cover) Effects on Printed Circuit Antennas," *IEEE Transactions on Antennas and Propagation*, Vol AP-32, No. 8, pp. 807-814, August 1984.

[71] N.G. Alexopoulos, D. R. Jackson, and P. B. Katehi, "Criteria for Nearly Omnidirectional Patterns for Printed Antennas," *IEEE Transactions on Antennas and Propagation*, Vol AP-33, No. 2, pp. 195-205, February.1985.